Electron Microscopy of Electromagnetic Waveforms

Andrey Ryabov

München 2016

Electron Microscopy of Electromagnetic Waveforms

Andrey Ryabov

Dissertation
an der Fakultät für Physik
der Ludwig–Maximilians–Universität
München

vorgelegt von
Andrey Ryabov
aus Moskau, Russland

München, den 22. Dezember 2016

Erstgutachter: Prof. Dr. Ferenc Krausz
Zweitgutachter: Prof. Dr. Roland Kersting
Tag der mündlichen Prüfung: 06. Februar 2017

Contents

List of Figures

List of Tables

Zusammenfassung

Schnell oszillierende elektrische und magnetische Felder bilden die Grundlage jeglicher mikroelektronischer Bauelemente sowie für fast alle Arten der Licht-Materie-Wechselwirkung. Ein Elektronenmikroskop unterliegt nicht der Beugungsbegrenzung eines optischen Mikroskops und ist daher hervorragend für die Untersuchung von Strukturen in Festkörpern auf der Nanoskala geeignet. Trotz des einfachen Zugangs zur Strukturinformation durch das Elektronenmikroskop sind üblicherweise andere Techniken notwendig, um elektromagnetische Phänomene zu beleuchten. Darüber hinaus ist für ultraschnelle Prozesse, die eine Ladungsträgerdynamik auf einer Zeitskala von Femtosekunden bis Pikosekunden aufweisen, eine entsprechende Zeitauflösung in dieser Größenordnung notwendig, um das elektromagnetische Verhalten einer Probe erfolgreich untersuchen zu können.

In dieser Arbeit wird ein Konzept für die Elektronenmikroskopie elektromagnetischer Wellenformen vorgestellt und gezeigt, dass eine Zeitauflösung unterhalb eines optischen Zyklus sowie eine Ortsauflösung unterhalb einer Wellenlänge erreicht wird. Diese Technik kann in einem Transmissions-Elektronenmikroskop Anwendung finden und somit dessen Fähigkeiten um die Erfassung elektromagnetischer Phänomene erweitern, wodurch Forscher Zugang zu neuartigen Informationen über Objekte erhalten können.

Dazu lassen wir einen kurzen Elektronenpuls durch eine Probe laufen, die von einem elektromagnetischen Puls angeregt wird, und nehmen die zeitabhängige Ablenkung des Elektronenstrahls auf. Wenn der Elektronenpuls – das Schlüsselelement dieser Technik – eine zeitliche Dauer hat, die kürzer als ein Zyklus der Anregungsstrahlung ist, werden die Elektronen durch eine zeitlich eingefrorene Lorentzkraft auf eine quasi-klassische Weise abgelenkt. Sie offenbaren daher direkt die Dynamik an der Probe. Mittels einer voll-optischen Terahertz-Kompressionsmethode ist es uns gelungen, einen Einzelelektronenpuls von 930 Femtosekunden Dauer auf 75 Femtosekunden zu verkürzen, was 15-mal kürzer ist als die Periode der in der Probe angeregten Dynamik. Um solch kurze Elektronenpulse zu charakterisieren, wurde *Streaking* mit THz-Feldern in einer Sub-Wellenlängenstruktur durchgeführt, was eine Zeitauflösung von unter 20 Femtosekunden ermöglicht.

Die Rekonstruktion der elektromagnetischen Felder aus der Ablenkung der Elektronen ist ein nichttriviales Problem. Wir lösen es, indem wir den Verlauf der Elektronendichte nach der Wechselwirkung mit der Probe in einem Anrege-Abfrage-Experiment erfassen und das Gauss-Newton-Verfahren für iterative Datenanpassung anwenden. Als Ergebnis erhalten wir eine zeitliche Sequenz aus zweidimensionalen räumlichen Verteilungen der Dynamik

der Feldvektoren mit einer zeitlichen Auflösung unterhalb eines Anregungszyklus. Eine weitere Datenanalyse kann zusätzlich Informationen über die Frequenz- und Materialantwort zusammen mit den Modenstrukturen und ihrer zeitlichen Dynamik liefern.

Wenn diese neue Technik mit einem Transmissions-Elektronenmikroskop kombiniert wird, wird es möglich sein, die schnellsten und kleinsten elektrodynamischen Prozesse in der Licht-Materie-Wechselwirkung und in Bauelementen zu untersuchen.

Abstract

Quickly oscillating electric and magnetic fields are the foundation of any information processing device or light-matter interaction. An electron microscope exceeds the diffraction limit of optical microscopes and is therefore a valuable device for condensed-matter structure and nanoscale objects investigations. While the electron microscope easily provides structural information, other methods are usually necessary to reveal the electromagnetic phenomena. Moreover, for ultrafast devices, in which charge-carrier dynamics occurs on femtosecond to picosecond time scales, the temporal resolution has to reach such values in order to successfully access the sample's electromagnetic response.

Here, we introduce and demonstrate a concept for electron microscopy of electromagnetic waveforms. We achieve sub-optical-cycle and sub-wavelength resolutions in time and space. The technique can be applied to a transmission electron microscope, which expands its capabilities to the regime of electromagnetic phenomena. The approach thus may give researchers access to additional important information on the object under investigation.

We let a short electron pulse pass through a sample, which is excited by an electromagnetic pulse, and record the time-dependent deflection. If the electron pulse, the key element of the technique, has a sub-cycle duration with respect to excitation radiation, the electrons are deflected by a time-frozen Lorentz force in a quasi-classical way and therefore directly reveal the sample's dynamics. By using an all-optical terahertz compression approach, we succeeded to shorten a single-electron pulse of 930 fs duration down to 75 fs, which is 15 times shorter than the period of excited in the sample dynamics. To characterize such short electron pulse, streaking with THz fields in a sub-wavelength structure was applied, which provided sub-20-femtosecond resolution.

The reconstruction of electromagnetic fields from the electron deflection is not a trivial problem. We solve it by recording the electron density evolution after the interaction with a sample in a pump-probe experiment and employ the Gauss-Newton algorithm for an iterative fitting analysis. As a result, we acquire a time delay sequence containing two-dimensional spatial distributions of the field vector dynamics with a sub-cycle resolution in time. Further analysis of the evaluated data can provide frequency and material response information together with mode structures and their temporal dynamics.

If the new technique is combined with a transmission electron microscope, it will be possible to study the fastest and smallest electrodynamic processes in light-matter interactions and devices.

Chapter 1

Motivation and background

“Higher resolution” – this catchword has almost always motivated scientists for novel scientific discoveries and technological breakthroughs. When characterizing materials that are naturally and technologically occurring, the resolutions that matter most include space, time and energy. Nowadays, a spatial resolution of tens of picometers (10^{-12} m) is achieved, for example, via electron microscopy [1–3], while a temporal resolution in laser-based extreme-ultraviolet (XUV) photonics reaches the attosecond regime (10^{-18} s) [4–6]. These and other techniques, which allow us to see transitions within structures as they occur, have been improved dramatically over the past few decades and are now successfully applied to a wide range of scientific fields, from physics to chemistry and biology. It is fair to say that atoms and their motion are now comprehensively captured by experiments with ultimate spatial and temporal resolutions.

However, not many techniques are able to reveal the dynamics of a sample’s electromagnetic field in space and time. Electromagnetic fields are either a decisive internal property of the sample or can be externally induced as an excitation, for example, to make a device operate as desired. A technique that would reveal these electromagnetic distributions in time and space would therefore be a novel basis for investigations of ultrafast devices, micro- and nanostructures and atomic-level light-matter interactions in general.

Table 1.1 shows some of the techniques that are related to or capable of measuring electromagnetic fields with their spatial and/or temporal resolutions. The *terahertz near-field imaging* technique can provide fascinating, comprehensive information about the field at a sample, its amplitude, phase and polarization [7–10]. This could basically be the method of choice, however, the sample’s field is disturbed by the probing element and the spatial resolution is limited by the probe beam size. Another optical technique is *surface optical microscopy* [11–16]. Here, the resolution is limited by the probing needle tip radius, and fields inside a sample (e.g., a complex structure) can hardly be measured.

Electron-based methods are another option. Due to the fact that the electron has a rest mass, its de Broglie wavelength can easily reach atomic dimensions, for example a wavelength of $\sim$5 pm at a kinetic energy of 60 kilo-electronvolt (keV). Together with the strong interaction between an electron and electromagnetic fields via the Lorentz force, *electron deflectometry* [22–25] currently offers a resolution that is superior to most other

	Spatial resolution	Sub-wavelength	Temporal resolution	Frequency range	Sub-cycle	Sample geometry	Field mapping	Nonlinear field mapping
DPS (Differential Phase Contrast Microscopy) [3, 17]	~ 0.5 Å	—	No	—	x	Transmission	Field, 2D -averaged	—
Photoelectron Imaging [18–21]	~ 1 Å	✓	$\lesssim 1$ fs	XUV	✓	Surface/Transmission	Electron density	—
Electron Deflectometry [22–25]	~ 1 Å - 100 nm	x	~ 1 ps	NIR	x	Transmission	Field, 2D -averaged	Possible
SNOM (Surface Near-field Optical Microscope) [11–16]	$\gtrsim 10$ nm	✓	~ 10 fs	MIR	✓	Surface/Transmission	Field, 3D -amplitude -phase	Possible
PINEM (Photon-Induced Near-field Electron Microscopy) [26–28]	~ 20 nm	✓	~ 100 fs	Visible	x	Transmission	Longitudinal field component -averaged	Possible
EELS-STEM (Electron Energy Loss Spectroscopy in Scanning Transmission Electron Microscope) [29, 30]	~ 10 nm	—	No	—	x	Transmission	Longitudinal field component -averaged	No
Terahertz near-field imaging [7–10]	$\gtrsim 10$ µm	✓	~ 100 fs	FIR	✓	Surface	Field, 3D -amplitude -phase -polarization	Possible

Table 1.1: *Comparison table of different techniques.* Columns *Sub-wavelength* and *Sub-cycle* correspond to the resolution with respect to the sample's excitation radiation.

techniques. Electromagnetic fields in space and time can indeed be recorded, but the temporal resolution has been insufficient to resolve optical cycles. Also, reconstruction and interpretation of the measured electron beam distortions into the field distributions is difficult. Importantly, the sub-cycle (with respect to an excitation signal) vectorial field could not be recorded.

This work introduces a new approach for investigating electromagnetic fields in space, time and vectorial direction, dubbed *waveform electron microscopy* [31]. The concept is applicable to complex structures and devices and provides sub-wavelength and sub-optical-cycle resolutions. This thesis reports, firstly, theoretical and experimental investigations of electron pulse control in space and time by an electromagnetic pulse; secondly, a description of a novel method for generating the shortest-ever electron pulses within an electron microscope with extremely low temporal jitter; thirdly, the experimental details and results of the waveform microscopy; fourthly, a novel reconstruction algorithm; fifthly, an estimation of the current resolution and the resolution that can be achieved with a modern instrument; and, finally, an outlook on the future prospect of this technique.

Chapter 2

Concept and requirements

This work is based on merging two well-known techniques and one novel concept: electron microscopy for obtaining an ultimate spatial resolution, a pump-probe technique for obtaining a sub-cycle resolution in time and a novel sub-cycle and sub-wavelength metrology concept for investigating dynamic electromagnetic fields [31]. An electromagnetic pulse and an electron bunch act as the pump and probe pulses, respectively. To describe the electron's behavior in a basic transmission electron microscope used in this work, we can well neglect its wave nature and, thus, treat the electron as a point particle, applying ray

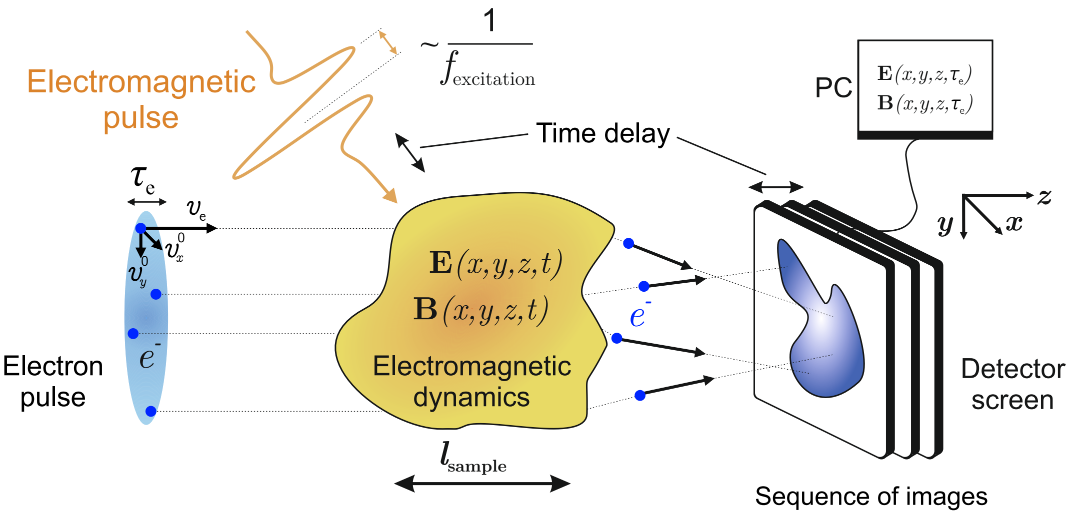

Figure 2.1: *Schematic of electron microscopy of electromagnetic fields.* A short electron pulse (light blue) with the duration of τ_e passes through a sample area with a characteristic longitudinal dimension l_{sample} (yellow). An electromagnetic pulse at the central frequency $\sim f_{\text{excitation}}$ externally excites an electromagnetic dynamics in the sample, which deflects the electrons, creating a sequence of distorted images on a detector screen (blue). At proper conditions (see Sections 2.1, 2.2), deflection occurs in a time-frozen way. The goal is to reconstruct the electromagnetic dynamics in the sample, obtaining vectorial, spatial and temporal resolutions at the same time.

optics. This is possible, because the de Broglie wavelength of the electron is below 5 pm at kinetic energies above the applied 70 keV, and also the spatial coherence in the beam does not exceed the spatial dimensions of the experiment [32, 33].

Fig. 2.1 shows a schematic of the conceptual experiment. Electromagnetic spatio-temporal dynamics is excited by an electromagnetic pulse and later probed by an electron pulse, which can be delayed in time. The local and time-dependent electromagnetic fields inside the sample area, where the dynamics occurs, deflect the electrons within the pulse. At proper conditions (see Sections 2.1, 2.2), deflections can be described by time-frozen fields. After passing a certain distance and some electron optics, a sequence of distorted images is detected. These images contain information of the dynamics and, under some conditions (see Section 2.3), the distortions can be used to reconstruct back the time-dependent vectorial electromagnetic field distribution in the sample [31].

In principle, the resolution in a transmission electron microscope can reach the atomic scale, and the quest to explore sub-cycle dynamics imposes some substantial restrictions on the allowable electron pulse duration and transition time through a sample. In the following sections we discuss those limits and in Chapter 4 we report a concept for producing the ultrafast electron pulses necessary for reaching sub-cycle resolution.

2.1 Sub-cycle electron pulse duration

When a sample is illuminated with electromagnetic radiation, it has a certain response, which can be resonant or non-resonant, linear or nonlinear with respect to the incident signal. In order to achieve sub-cycle temporal resolutions, the probing electron pulse must be shorter than the characteristic oscillation period of any dynamics in the sample. The maximal excitation and response frequency existing in a sample limits the maximal duration that the electron pulses can have:

$$\tau_{\mathrm{e}} \lesssim \frac{1}{2\max(f_{\mathrm{excitation}}, f_{\mathrm{response}})}, \tag{2.1}$$

where τ_{e} is the characteristic electron pulse duration and $f_{\mathrm{excitation}}, f_{\mathrm{response}}$ are the excitation and the response frequencies, respectively. The factor 1/2 shows that the pulse duration should preferably be shorter than a half-cycle of the electromagnetic oscillations to avoid averaging over the whole period.

This is difficult to achieve experimentally. Vacuum is a dispersive medium for electrons at non-relativistic energies: lower-energetic parts of the wave packet propagate slower than higher-energetic parts [34, 35]. Moreover, electrons generated by photoelectron emission and accelerated in a static electric field [36, 37] are further broadened during propagation as a result of Coulomb repulsion. In contrast to a many-electron pulse, a single-electron pulse [32, 35, 38] is free of such space-charge effects. The single-electron pulse duration is defined as the width of the particle arrival time distribution over many measurements [32, 38, 39] and is limited by timing jitter [40] and electron optical distortions [41].

As it will be shown in Section 4.3, the electron pulse duration, if compressed by terahertz (THz) radiation [36], is around 80 fs (full width at half maximum) in the reported experiments, which is ~15 times shorter than the maximum spectral component of the excitation pulse at 0.8 THz (see Section 3.1). While considering a linear response of the sample[1], the sub-cycle condition is satisfied.

2.2 Transition time

In the previous section, the properties of the probe pulse were discussed to fit the excitation signal. Now we need to consider the properties of the sample in accordance to the electron pulse. In order to achieve sub-cycle resolution and to have a regime of time-frozen fields, the electron must pass through the sample within a time less than about one cycle of the dynamics oscillation period. Hence, in order to probe the sub-cycle field, the electromagnetic field structure in the sample must not be longer than $0.5\,\lambda \approx 0.5\,c/\max(f_{\text{excitation}}, f_{\text{response}})$ in the propagation direction, where λ stands for the characteristic field wavelength and c is the speed of light. Therefore, the sample has to be sub-wavelength in depth, i.e., the longitudinal dimension of the structure must be shorter than the characteristic wavelength: $l_{\text{sample}} \lesssim \lambda/2$. Otherwise, the transmitted electron would contain information of the spatially averaged field over different oscillation cycles[2], which would complicate the reconstruction analysis. The transition time through the sample is $\tau_{\text{transition}} \approx l_{\text{sample}}\, {v_{\text{e}}}^{-1}$, where v_{e} stands for the electron propagation velocity. Combining all together, we get a condition for the sample length:

$$l_{\text{sample}} \lesssim \frac{v_{\text{e}}}{2\max(f_{\text{excitation}}, f_{\text{response}})} \leq \frac{c}{2\max(f_{\text{excitation}}, f_{\text{response}})}. \tag{2.2}$$

One might consider to increase the electron velocity to make it pass through the sample faster; however, this approach is technically complex. To double the velocity of the electron at 70 keV, the acceleration voltage has to reach 1.2 MV, which would dramatically increase the effort to implement it in a transmission electron microscope. Moreover, the deflection would be reduced proportional to v_{e}^{-2} (see Section 2.3). In this work, we chose the electron velocity $v_{\text{e}} \approx 0.48\,c$, which implies $l_{\text{sample}} \lesssim 90\,\mu\text{m}$ ($t_{\text{transition}} \lesssim 200\,\text{fs}$) at 0.8 THz, while the samples investigated in Chapters 4 and 5 have a thickness of $l_{\text{sample}} = 30\,\mu\text{m}$ (for more details see Section 4.2), thus the condition is satisfied. Most metamaterials or other technologically interesting micro- and nanostructures have a sub-wavelength size by definition, so the inequality (2.2) is generally easy to satisfy.

---

[1] In the case of a linear response, the incident electromagnetic pulse does not generate harmonics beyond its initial spectral range. In the nonlinear regime, the electron pulse duration has to be reconsidered to satisfy inequality (2.1) with correspondence to higher harmonics.

[2] In Section 8.3, we discuss a tomographic application of this method, where l_{sample} can be above the sub-wavelength regime.

2.3 Electric and magnetic fields

It was concluded earlier that electrons can be treated classically in the electron microscope applied in this work. The electron-light interaction is described by the Lorentz force via the electric field vector **E** and the magnetic field vector **B** (as far as we neglect the Aharonov-Bohm effect[3]). We obtain:

$$\mathbf{F}^{\text{Lorentz}}(x,y,z,t) = e\left(\mathbf{E}(x,y,z,t) + [\mathbf{v}\times\mathbf{B}(x,y,z,t)]\right), \tag{2.3}$$

where $\mathbf{F}^{\text{Lorentz}}$, e, $\mathbf{v}$ are the Lorentz force vector, the electron charge and the electron velocity vector, respectively.

Consider now a single electron that enters a sample with electromagnetic dynamics at moment in time $t = 0$ and point in space $(x,y,z) = (0,0,0)$, with $\mathbf{v} = \{v_x^0, v_y^0, v_\text{e}\}$, $v_{x,y}^0 \ll v_\text{e}$, where v_x^0, v_y^0, v_e are the x-, y- and z-components of the electron velocity, respectively (see Fig. 2.1 for the coordinate system). For the electromagnetic dynamics we apply following assumptions:

(I) The field is stationary, i.e. time-frozen (the result of the requirements 2.2 and 2.1):

$$\mathbf{E}(x,y,z,t) = \mathbf{E}(x,y,z); \tag{2.4}$$
$$\mathbf{B}(x,y,z,t) = \mathbf{B}(x,y,z). \tag{2.5}$$

(II) Sideways drift of the electrons along the x- and y-axis is negligible inside the volume of the dynamics (we estimate this in Appendix B):

$$\mathbf{E}(x,y,z) = \mathbf{E}(0,0,z); \tag{2.6}$$
$$\mathbf{B}(x,y,z) = \mathbf{B}(0,0,z). \tag{2.7}$$

(III) Longitudinal velocity changes are negligible and we can consider the electromagnetic field as a depth-averaged field over the sample $l_\text{sample} \leq \dfrac{v_\text{e}}{2\max(f_\text{excitation}, f_\text{response})}$ (result of the requirement 2.2):

$$\widetilde{\mathbf{E}}(0,0) = \int_{l_\text{sample}} \mathbf{E}(0,0,z)\,dz; \tag{2.8}$$
$$\widetilde{\mathbf{B}}(0,0) = \int_{l_\text{sample}} \mathbf{B}(0,0,z)\,dz. \tag{2.9}$$

In the following equations, the tilde is dropped for convenience. The assumptions above define a two-dimensional static-field problem approximation with fields **E** and **B**. Let us write down the equation of motion of the electron for all spatial components:

---

[3] The effect, when the electron wave function acquires a phase shift while traveling through an area with zero electromagnetic field but non-zero electric or vector magnetic potentials.

$$\begin{cases} m_\mathrm{e}\,\ddot{x} = e\,(E_x + \dot{y}\,B_z - \dot{z}\,B_y)\,; \\ m_\mathrm{e}\,\ddot{y} = e\,(E_y - \dot{x}\,B_z + \dot{z}\,B_x)\,; \\ m_\mathrm{e}\,\ddot{z} = e\,(E_z - \dot{y}\,B_x + \dot{x}\,B_y)\,. \end{cases} \tag{2.10}$$

In practice, we do not consider z-component of the Lorentz force due to our inability to resolve longitudinal velocity changes in the experiment. Under typical conditions, these changes are much smaller than the initial electron velocity v_e, thus we have:

$$\begin{aligned} &\begin{cases} m_\mathrm{e}\,\ddot{x} = e\,(E_x - v_\mathrm{e}\,B_y) + e\,\dot{y}\,B_z; \\ m_\mathrm{e}\,\ddot{y} = e\,(E_y + v_\mathrm{e}\,B_x) - e\,\dot{x}\,B_z; \end{cases} \Leftrightarrow \begin{cases} m_\mathrm{e}\,\ddot{x} = e\,E_x^\mathrm{eff} + e\,\dot{y}\,B_z; \\ m_\mathrm{e}\,\ddot{y} = e\,E_y^\mathrm{eff} - e\,\dot{x}\,B_z; \end{cases} \Leftrightarrow \\ &\Leftrightarrow \begin{cases} m_\mathrm{e}\,\ddot{x} = e\,E_x^\mathrm{eff} + e\,v_y^0\,B_z + \frac{e^2}{m_\mathrm{e}}\,E_y^\mathrm{eff}\,B_z\,t - \frac{e^2}{m_\mathrm{e}}\,B_z^2\,x\,; \\ m_\mathrm{e}\,\ddot{y} = e\,E_y^\mathrm{eff} - e\,v_x^0\,B_z - \frac{e^2}{m_\mathrm{e}}\,E_x^\mathrm{eff}\,B_z\,t - \frac{e^2}{m_\mathrm{e}}\,B_z^2\,y\,; \end{cases} \Leftrightarrow \\ &\Leftrightarrow \begin{cases} \ddot{x} + \omega_0^2\,x = f_x^0 + \omega_0\,v_y^0 + \omega_0\,f_y^0\,t; \\ \ddot{y} + \omega_0^2\,y = f_y^0 - \omega_0\,v_x^0 + \omega_0\,f_x^0\,t, \end{cases} \end{aligned} \tag{2.11}$$

where $\omega_0 = \frac{e\,B_z}{m_\mathrm{e}}$ is a circular cyclotron frequency, $f_{x,y}^0 = \frac{e\,E_{x,y}^\mathrm{eff}}{m_\mathrm{e}}$ are normalized forces and $E_{x,y}^\mathrm{eff} = E_{x,y} \mp v_\mathrm{e}\,B_{y,x}$ is an effective field. The equation system (2.11) can be easily solved, and the resulting expressions for the coordinates and transversal velocities are:

$$\begin{cases} x(t) = \dfrac{v_x^0}{\omega_0}\sin\,\omega_0 t + \dfrac{f_x^0 + \omega_0\,v_y^0}{\omega_0^2}(1 - \cos\,\omega_0 t) + \dfrac{f_y^0}{\omega_0^2}\,(\omega_0 t - \sin\,\omega_0 t)\,; \\ \\ y(t) = \dfrac{v_y^0}{\omega_0}\sin\,\omega_0 t + \dfrac{f_y^0 - \omega_0\,v_x^0}{\omega_0^2}(1 - \cos\,\omega_0 t) - \dfrac{f_x^0}{\omega_0^2}\,(\omega_0 t - \sin\,\omega_0 t)\,; \end{cases} \tag{2.12}$$

$$\begin{cases} \dot{x}(t) = v_x^0\,\cos\omega_0 t + \dfrac{f_x^0 + \omega_0\,v_y^0}{\omega_0}(\sin\,\omega_0 t) + \dfrac{f_y^0}{\omega_0}\,(1 - \cos\,\omega_0 t)\,; \\ \\ \dot{y}(t) = v_y^0\,\cos\omega_0 t + \dfrac{f_y^0 - \omega_0\,v_x^0}{\omega_0}(\sin\,\omega_0 t) - \dfrac{f_x^0}{\omega_0}\,(1 - \cos\,\omega_0 t)\,. \end{cases} \tag{2.13}$$

Each coordinate position depends on both electric and magnetic field components, however, their dependencies are different. Assuming $\omega_0 t < 1$ (see Appendix B for detailed analysis) and keeping only terms up to the second order for the argument $\omega_0 t$ yields:

$$\begin{cases} x(t) \approxeq v_x^0\, t + \dfrac{f_x^0 + \omega_0\, v_y^0}{2} t^2; \\ y(t) \approxeq v_y^0\, t + \dfrac{f_y^0 - \omega_0\, v_x 0}{2} t^2; \end{cases} \tag{2.14}$$

$$\begin{cases} \dot{x}(t) \approxeq v_x^0 + \left(f_x^0 + \omega_0\, v_y^0\right)\, t; \\ \dot{y}(t) \approxeq v_y^0 + \left(f_y^0 - \omega_0\, v_x^0\right)\, t. \end{cases} \tag{2.15}$$

Expressions (2.14) and (2.15) are kinematic equations for the electron inside the time-frozen electromagnetic dynamics. In this approximation, after passing the sample (at $t = \tau_{\text{transition}}$), the electron acquires the transversal velocity, which components are proportional to the respective Lorentz force components:

$$\begin{cases} F_x^{\text{Lorentz}} = e\, \left(E_x - v_{\text{e}}\, B_y + v_y^0\, B_z\right); \\ F_y^{\text{Lorentz}} = e\, \left(E_y + v_{\text{e}}\, B_x - v_x^0\, B_z\right). \end{cases} \tag{2.16}$$

These expressions could have been derived from the electron's motion equations (2.10) by applying assumptions (I)-(III), but the analysis of the assumption ($\omega_0 t < 1$) can provide field amplitudes, at which the relation between the gained transversal velocity and field components keeps linear behavior. In Appendix B, an estimation of the cyclotron frequency, the electron displacement and deflection inside the electromagnetic dynamics area are introduced for the samples used in the experiment. Moreover, we can neglect terms ($v_y^0\, B_z(x, y)$) and ($v_x^0\, B_z(x, y)$) in equations (2.16) by minimizing initial velocity components v_x^0 and v_y^0 in the experiment while providing a well-collimated beam. Thus, the deflection of the electron is linear to the effective field:

$$\begin{cases} E_x^{\text{eff}} = E_x - v_{\text{e}}\, B_y; \\ E_y^{\text{eff}} = E_y + v_{\text{e}}\, B_x. \end{cases} \tag{2.17}$$

Although, these expressions can be considered as normalized to the electron charge e Lorentz force, with term "field" we emphasize that it is possible to reveal the electric and magnetic field vectors separately. To be able to do so, it is required to perform the same measurement for different v_{e} by tuning electron acceleration voltage, since the electric field deflection contribution scales proportionally to v_{e}^{-2}, but the deflection by the magnetic field follows v_{e}^{-1} (see equation (2.18)). The term "effective" is used to show that the field components in expressions 2.16 or 2.17 are longitudinally integrated and they do not include any hidden quantity.

Since the deflection angle $\alpha_{x,y}^{\text{deflection}}$ is proportional to the transversal velocity in a small angle approximation, we obtain the key expression from equations (2.15) that connects the physics at the sample to the data obtained in the experiment:

$$\alpha_{x,y}^{\text{deflection}} = \frac{v_{x,y}}{v_{\text{e}}} = \frac{e\, E_{x,y}^{\text{eff}}\, l_{\text{sample}}}{m_{\text{e}}\, v_{\text{e}}^2}. \tag{2.18}$$

Chapter 3

Laser system and electron pulse generation

In this section, the laser system and electron gun used in the experiment are described and all known parameters of the electron beam are summarized. These serve as the basis for the following studies on both the THz control of electron pulses (see Chapter 4) and the electron microscopy of electromagnetic waveforms (see Chapters 5 - 7).

3.1 Laser system and beam line

The laser system and beam line, which supply all the experiments in this work, are schematically depicted in Fig 3.1. The laser system has been described before [42, 43] and was readjusted and improved for this work.

The Yb:YAG regenerative amplifier (see Fig 3.1) delivers 340 µJ, ∼1 ps pulses at 1030 nm central wavelength with a repetition rate of 50 kHz [43]. A small fraction of the output is frequency-doubled in a BBO crystal and triggers two-photon photoemission from a cathode [37] (see Section 3.2). Magnetic coils are used to focus the electron beam spatially. Electrons are detected on a phosphor screen, coupled to a camera chip by fiber optics (TemCam F416, 4096 × 4096 pixels[1], 16 bit dynamic range, CMOS technology, TVIPS GmbH).

The major part of the laser output is guided into two separate THz generation setups. In "THz block 1", the near-infrared pulse from the laser is spatially and temporally stretched by a grating and subsequently imaged on the side edge of a prism, cut from a 0.6% MgO-doped stoichiometric lithium niobate crystal ($LiNbO_3$ or LN) [43, 44]. As an output, we obtain a single-cycle THz pulse (see Fig. 3.2) centered at ∼0.3 THz with a bandwidth of 0.3 THz (full width at half maximum) and an amplitude up to 20 kV/cm at 8.6 W of incident pump power. After the LN crystal, the THz pulse is steered by metallic mirrors through a silicon window into the vacuum chamber. In "THz block 2", the laser pulse generates Cherenkov-type THz radiation in the LN crystal slab, which is further coupled out with a silicon prism [45]. The THz pulse is guided into the vacuum chamber by metallic mirrors and

---

[1] Pixel size is $15.6 \times 15.6 \mu m^2$.

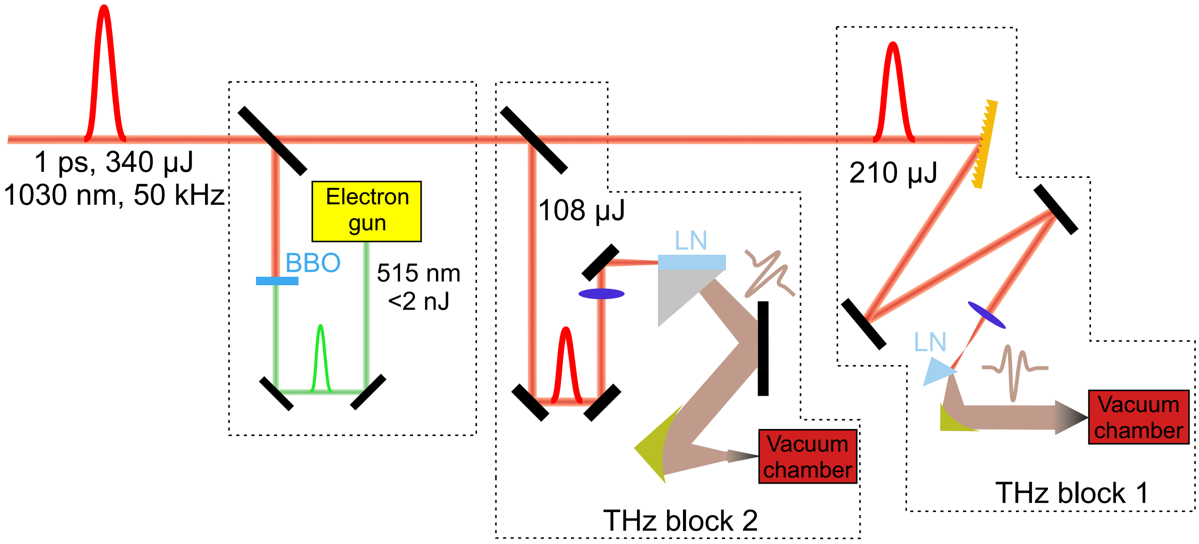

Figure 3.1: *Laser system and beam line.* An Yb:YAG regenerative amplifier delivers 340 µJ, ~1 ps pulses at 1030 nm central wavelength with a repetition rate of 50 kHz. A small fraction of the output (<100 mW) is frequency-doubled in a BBO crystal and triggers two-photon photoemission from a cathode. The major part of the laser output is guided into two separate THz generation setups: "THz block 1" and "THz block 2". In "THz block 1", the near-infrared pulse generates a single-cycle THz pulse in a lithium niobate (LN) crystal with a pulse-front-tilt technique, which is guided by metal mirrors into a vacuum chamber and is focused onto a sample with an off-axis parabola for sample excitation. In "THz block 2", a near-infrared pulse generates a single-cycle THz pulse in a LN crystal but in Cherenkov scheme. The THz pulse is coupled out with a silicon prism attached to the LN crystal and then guided into the vacuum chamber by metal mirrors and an off-axis parabola for subsequent THz compression of single-electron pulses.

an off-axis parabola and further used for electron pulse compression (see Section 4.3). The THz spectrum of "THz block 2" is similar to the one from "THz block 1" (see Fig. 3.2) [43, 45]. Both THz beams can be focused below 2.5 mm diameter (full width at half maximum). "THz block 2" was applied because its simplicity and smaller space requirement comparing to "THz block 1".

3.2 Electron gun

The detailed description of the electron gun, designed by Dr. Peter Baum and Dr. Daniel Kreier, can be found in [46] and [37]. Frequency-doubled laser pulses are focused on a 20-nm gold layer deposited on a sapphire substrate[2] to a beam size of several micrometers. The electrons generated via a two-photon photoemission process are accelerated by a static field

---

[2] For experiments, performed at 70 kV, a chrome layer of ~5 nm was additionally deposited between the sapphire and the gold.

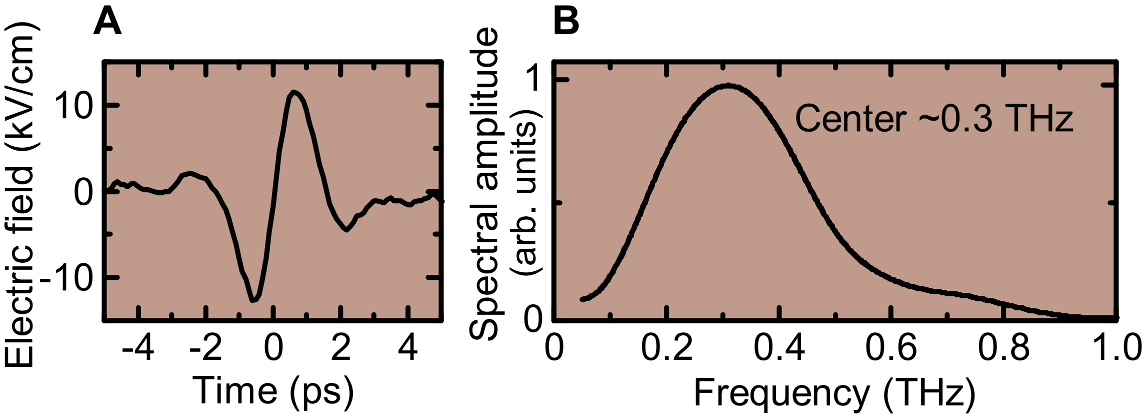

Figure 3.2: *Terahertz pulse electric field and spectrum.* The measurement of the pulse from "THz block 1" is performed with an electro-optical sampling technique. (A) Electric field of the THz pulse. (B) Spectrum of the THz signal. The figure is taken from [43].

of 3.6 MV/m and 2.8 MV/m at applied voltages of 90 kV and 70 kV, respectively, where the cathode-anode distance L_{acc} is 25 mm (see Fig. 3.3).

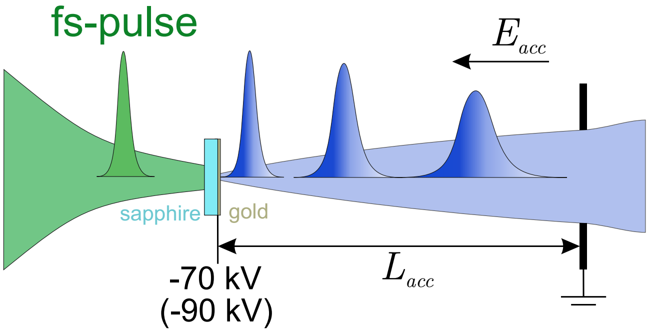

Figure 3.3: *Electron gun schematic.* An optical frequency-doubled laser pulse is focused onto a gold film, coated on a sapphire substrate. The emittance of the gun is 20 nm·rad and the source size is 10 µm [47]. Electrons generated via two-photon photoemission process are accelerated and dispersed in a static field. Higher-energetic electrons are shown in light blue, lower-energetic in dark blue. For 70 kV and 90 kV, the electron pulse duration after the anode is 930 fs and 790 fs, respectively.

As discussed above, single-electron pulses are used in order to avoid Coulomb repulsion. However, even without space charge effects [32], there are fundamental limitations of a single-electron pulse duration generated by an ultrashort optical pulse, which can be overcome by compression techniques (see Chapter 4). The time, at which the electron is extracted from the cathode, is not exactly determined due to the finite optical pulse duration and has a spread of τ_{laser} (assuming a Gaussian-like pulse) [32]:

$$\tau_{\mathrm{laser}} \approx \frac{2\pi\hbar}{\Delta E}. \tag{3.1}$$

where ΔE is the energy bandwidth of the optical pulse and $\hbar$ is the reduced Planck constant. On the other side, the initial kinetic energy spread of the electron ΔE, due to the optical pulse's energy spread and work function mismatch, is the cause of a temporal broadening of τ_{acc} after the acceleration in a static field E_{acc} [32]:

$$\tau_{\mathrm{acc}} \approx \frac{\left(\sqrt{2}m_{\mathrm{e}}\right)^{1/2}}{eE_{\mathrm{acc}}}\sqrt{\Delta E}. \tag{3.2}$$

The single-electron pulse duration at the anode[3] is a convolution of the optical pulse duration τ_{laser} and the temporal broadening τ_{acc} [32]:

$$\tau_{\mathrm{electron}} \approx \sqrt{\tau_{\mathrm{laser}}^2 + \tau_{\mathrm{acc}}^2} \tag{3.3}$$

The energy spread ΔE of the electron gun employed in this work is estimated as 0.6 eV [36] and $\tau_{\mathrm{laser}} \approx 500\,\mathrm{fs}$, therefore the single-electron pulse duration is 930 fs at 70 kV and 790 fs at 90 kV, which is in excellent agreement with the experiment, shown in Sections 4.1 and 4.2. Moreover, in Section 4.3, we demonstrate electron timing jitter of below 5 fs (root mean square) [36]. The electron source's emittance and the source size are ∼20 nm·rad and ∼10 µm[4], respectively, estimated by fitting the data of beam waist scans [47].

---

[3] The broadening from the anode to the sample of non-relativistic single-electron pulses is $t_{\mathrm{sample}} \approx 2\Delta E\sqrt{m_{\mathrm{e}}}\,l_{\mathrm{s}}\left(eU_{\mathrm{acc}}\sqrt{2eU_{\mathrm{acc}}}\right)^{-1}$, where l_{s} and U_{acc} are the anode-sample distance and the acceleration voltage, respectively. This broadening is on the order of tens of femtosecond for $l_{\mathrm{s}} = 1\,\mathrm{m}$ and $U_{\mathrm{acc}} = 70\,\mathrm{kV}$.

[4] The fitting results of beam waist scan data, obtained with different magnetic lenses (ML1 and ML2, see Fig. 4.5), are somewhat different due to a noticeable magnetic response of some elements in the experimental setup.

Chapter 4

THz control of ultrashort electron pulses

The small de Broglie wavelength of electrons at tens to hundreds of kilo-electronvolt (keV) of kinetic energies and their strong interaction with matter are a significant benefit to electron microscopy [1, 2] and crystallography [48, 49] for studying condensed matter. In order to observe atomic motion during transitions and molecular rearrangements, a temporal resolutions of at least hundreds of femtosecond must be achieved. The pump-probe technique allows to do so: an ultrashort laser pulse (a pump pulse) excites different dynamics inside a material and a second ultrashort pulse (a probe pulse) is applied to obtain structural information at a sequence of time delays. In ultrafast electron microscopy (UEM) and ultrafast electron diffraction (UED) techniques, the second pulse, which is usually generated by photoelectric emission with femtosecond lasers, contains electrons [50–52]. In case of multi-electron bunches, such pulses get broadened during the propagation due to Coulomb repulsion between the particles [35]. The single-electron pulse approach [32] does not have this problem, however, the generated electrons have an energy spread nonetheless (see Section 3.2) and disperse in vacuum.

To have as short as possible electron pulses at the sample position, different techniques can be used, for example, laser-triggered streaking [53], single-shot time-stamping [54], energy filtering [55] or optical gating [56, 57]. Compression with microwave cavities provides 150-fs (full width at half maximum) individual free electron pulses in the multi-electron regime [58] and 10-fs-pulses (root mean square) for single-electron wave packets [40]. The main problem of the microwave compression approach lies in appreciable phase drifts, which dramatically increases the technological effort to compensate for it [59]. To overcome such drift issues, we chose here another concept, *all-optical THz compression* [36]. The same laser pulses drive the electron generation, the sample excitation and the compression in an all-optical phase-locked way [36].

In order to investigate how the THz compression, the basis for waveform electron microscopy, works in the most efficient way, we discuss here the use of an ultrathin planar metal foil as a compressor element in more details than before [36]. In the case of low-energy electrons and photons[1] ($E_{\mathrm{photon}}, E_{\mathrm{electron}} \ll m_{\mathrm{e}}c^2$, where E_{photon} and E_{electron} are

---

[1] Compton scattering is negligible in this regime as well.

photon and electron energies, m_e is the electron rest mass, c is the speed of light), it is forbidden for a free electron to absorb or emit a photon in free space [28], thus, we need to introduce a third body to do so. Ponderomotive forces in the experiments are negligible (see Section 3.1 for THz pulse energies). In this chapter, an ultrathin metal foil and different sub-wavelength structures are investigated from theoretical and experimental points of view with attention to energy-momentum exchange between the free electron and the THz radiation. This chapter reproduces some figures and results from [36].

4.1 THz deflection at ultrathin metal foil

A 70-nm-thin aluminum foil works almost as a perfect mirror for electromagnetic radiation in the THz frequency range [60]. At the same time, 90-keV electrons can pass through quite easily with an average transmission of 30 % [42]. The foil introduces an abrupt halt for the interaction between the incoming THz wave and the particle, thereby allowing the electron to gain or lose momentum. This section presents a first-order approximation theory for such interactions and some experimental results showing good agreement. Residual deviations from the theory are associated with difficulties to create close-to-ideal conditions for the THz and electron beams.

4.1.1 Velocity matching

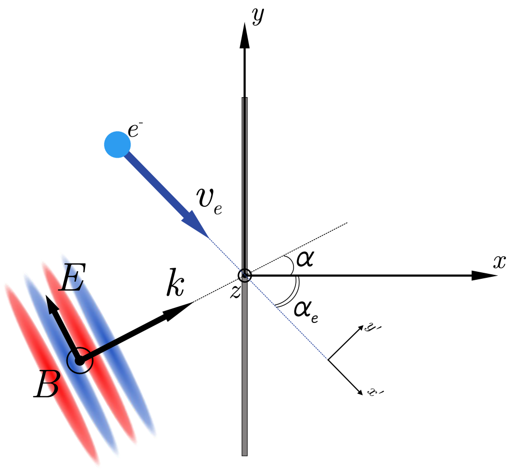

Figure 4.1: *Plane wave reflection and electron momentum gain at thin metal sheet.* A p-polarized electromagnetic plane wave with an incidence angle α is reflected by an ideal thin metal mirror, positioned at $x = 0$. An electron with the velocity v_e and an incident angle α_e passes through the mirror freely and gains transversal and longitudinal momenta along the y'- and x'-axis, respectively.

Assume a perfect mirror sheet at a spatial position $x = 0$ and an incident plane electromagnetic wave (see Fig 4.1). The z-coordinate is irrelevant. The electric field vector $\mathbf{E}$ and wave vector $\mathbf{k}$ both lie in the x-y plane, the incident angle is α. The spatio-temporal field can be written as a sum of two plane waves, co-propagating along y-axis and counter-propagating along the x-axis:

$$E_x(t,x,y) = \begin{cases} E_0\,(-\sin\,\alpha)\,(\sin(\omega t - kx\,\cos\alpha - ky\,\sin\alpha + \phi) + \\ + \sin(\omega t + kx\,\cos\alpha - ky\,\sin\alpha + \phi)), \text{ if } x < 0; \\ 0, \text{ if } x \geq 0; \end{cases} \tag{4.1}$$

$$E_y(t,x,y) = \begin{cases} E_0\,\cos\alpha\,(\sin(\omega t - kx\,\cos\alpha - ky\,\sin\alpha + \phi) - \\ - \sin(\omega t + k\,x\cos\alpha - ky\,\sin\alpha + \phi)), \text{ if } x < 0; \\ 0, \text{ if } x \geq 0; \end{cases} \tag{4.2}$$

$$B_z(t,x,y) = \begin{cases} \frac{E_0}{c}(\sin(\omega t - kx\,\cos\alpha - ky\,\sin\alpha + \phi) + \\ + \sin(\omega t + kx\,\cos\alpha - ky\,\sin\alpha + \phi)), \text{ if } x < 0; \\ 0, \text{ if } x \geq 0. \end{cases} \tag{4.3}$$

Here k, ω, ϕ are the wave vector length, the angular frequency and the phase shift, respectively, E_0 is the electric field amplitude. From expressions (4.1)-(4.3) it is obvious that the wave incident angle $\alpha \in [-\frac{\pi}{2}, \frac{\pi}{2}]$.

The electron propagates with a velocity v_e and has an incidence angle α_e, so its kinematic equations for the coordinate components are $x(t) = v_\mathrm{e}\,\cos\alpha_\mathrm{e}\,(t-\tau)$ and $y(t) = v_\mathrm{e}\,\sin\alpha_\mathrm{e}\,(t-\tau)$, where τ is the temporal delay between the electron and the plane wave arrival. By inserting these equations into (4.1)-(4.3), we can write the longitudinal and the transversal momentum changes $p_{x'}$ and $p_{y'}$ of the particle (along the x'- and y'-axis respectively):

$$\begin{aligned} p_{x'}(\tau) = eE_0 \int\limits_{-\infty}^{\infty} (\,&\sin(\omega t - \omega\beta\,\cos(\alpha-\alpha_\mathrm{e})\,(t-\tau)+\phi)\,\sin(\alpha_\mathrm{e}-\alpha) - \\ &- \sin(\omega t + \omega\beta\,\cos(\alpha+\alpha_\mathrm{e})\,(t-\tau)+\phi)\,\sin(\alpha_\mathrm{e}+\alpha))\,dt; \end{aligned} \tag{4.4}$$

$$\begin{aligned} p_{y'}(\tau) = eE_0 \int\limits_{-\infty}^{\infty} (\,&\sin(\omega t - \omega\beta\,\cos(\alpha-\alpha_\mathrm{e})\,(t-\tau)+\phi)\,(\cos(\alpha-\alpha_\mathrm{e})-\beta) - \\ &- \sin(\omega t + \omega\beta\,\cos(\alpha+\alpha_\mathrm{e})\,(t-\tau)+\phi)\,(\cos(\alpha+\alpha_\mathrm{e})+\beta))\,dt, \end{aligned} \tag{4.5}$$

where $\beta = \frac{v_\mathrm{e}}{c}$ and e is the electron charge. For details see Appendix A. Here the results of integration are presented:

$$p_{x'}(\tau) = e\,E_0\,\mathrm{sign}(\cos\,\alpha_\mathrm{e})\frac{\cos(\omega t+\phi)}{\omega}\left(\frac{\sin(\alpha-\alpha_\mathrm{e})}{(1-\beta\cos(\alpha-\alpha_\mathrm{e}))} + \frac{\sin(\alpha+\alpha_\mathrm{e})}{(1+\beta\cos(\alpha+\alpha_\mathrm{e}))}\right); \tag{4.6}$$

$$p_{y'}(\tau) = e\,E_0\ \mathrm{sign}(\cos\,\alpha_\mathrm{e})\frac{\cos(\omega t+\phi)}{\omega}\left(\frac{\cos(\alpha+\alpha_\mathrm{e})+\beta}{(1+\beta\cos(\alpha+\alpha_\mathrm{e}))}-\frac{\cos(\alpha-\alpha_\mathrm{e})-\beta}{(1-\beta\cos(\alpha-\alpha_\mathrm{e}))}\right). \tag{4.7}$$

where $\mathrm{sign}(\cos\,\alpha_\mathrm{e}) = 1$ if $(\cos\,\alpha_\mathrm{e}) > 0$ and $\mathrm{sign}(\cos\,\alpha_\mathrm{e}) = -1$ if $(\cos\,\alpha_\mathrm{e}) < 0$. Expressions (4.6) and (4.7) show that the momentum gain has the same frequency as the incident field and it has a phase shift of $\frac{\pi}{2}$. In Fig. 4.2, contour maps for the amplitudes of $p_{x'}$ and $p_{y'}$ are plotted. These plots help to find geometric conditions, i.e., α and α_e, for the momentum gain required.

The expressions above maintain validity if we introduce a temporal (e.g., a Gaussian shape) envelope of the incident wave with a group velocity of c. Although it is not shown rigorously in this work due to complexity, but physical intuition, simulations and the fact that interactions have a certainty in phase – all indicate the same behavior as in the plane-wave approximation. However, if we also add a transversal dimension of the electromagnetic pulse (e.g., a Gaussian beam waist), the deflection and the acceleration curves are changed: some additional tails arise in the signal, because the particle now propagates through a spatio-temporal gradient of the field.

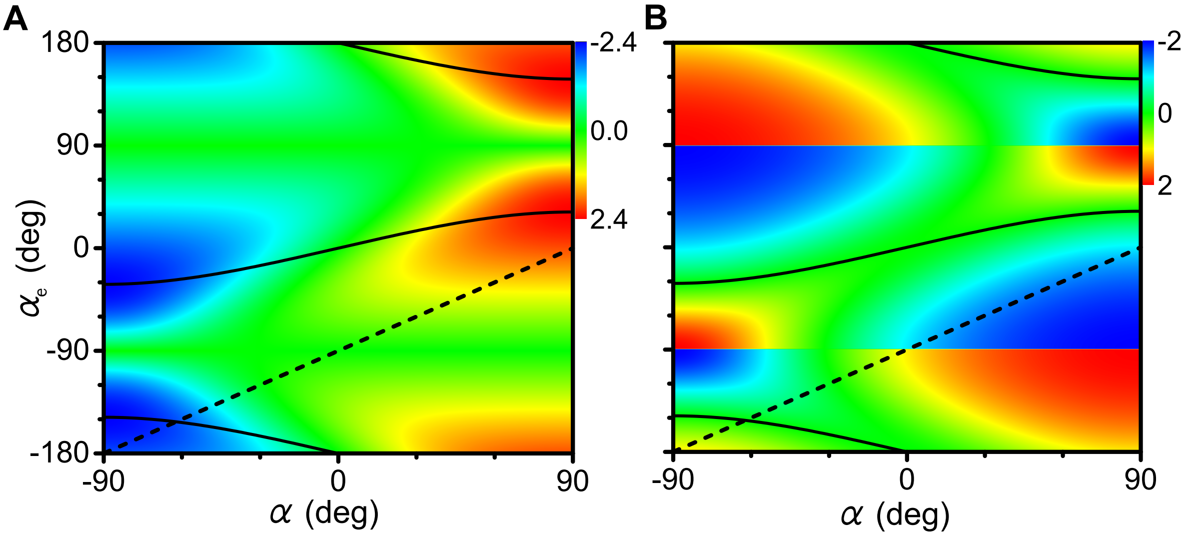

Figure 4.2: *Contour plots of momentum gain of electron.* (A) Longitudinal momentum gain map. (B) Transversal momentum gain map. The plots are normalized to $[eE_0\,\cos(\omega t+\phi)/\omega]$. The solid black lines show a velocity-matching condition, a dashed black line is $\alpha_\mathrm{e} = \alpha - \theta$, where θ is the relative angle of 90° between the plane wave and the electron. A phase jump in the transversal momentum gain is related to the integration limits and the resulting sign-function.

Let us assume now an infinitely short electron pulse with a transversal dimension, i.e., with a finite beam diameter. In this case, "velocity-matching" becomes important: to avoid distortions within the electron beam profile due to the deflection and acceleration at different transversal locations, all electrons must arrive at the same phase of the incident wave at the foil [61]. This condition is easy to express mathematically as:

$$\frac{v_{\mathrm{e}}}{\sin\,\alpha_{\mathrm{e}}} = \frac{c}{\sin\,\alpha}. \tag{4.8}$$

An important detail to be noticed is that expression (4.8) appears to be one of the zero-conditions of equation (4.7) (see expression (8) in Appendix A). This is quite a surprising result, meaning that electrons under velocity-matching condition automatically gain no transversal momentum (see Fig. 4.2), which is very functional in the experiment. In practice, a relative angle $\theta = \alpha - \alpha_{\mathrm{e}}$ between the plane wave and the electrons is defined by the setup construction. With the help of the maps depicted in Fig. 4.2 maps, it is easy to find the velocity-matching condition at any given relative angle by simply intersecting the line $\alpha_{\mathrm{e}} = \alpha - \theta$ and the velocity-matching curve.

The longitudinal momentum gain $p_{x'}$ can be used for compression to create a train of ultrashort pulses at high optical frequencies [62], or an individual ultrashort pulse with microwave or THz fields [36, 63]. In the latter concept, the initial electron pulse duration should be shorter than one half-period of the wave oscillation. For more details see Section 4.3.

4.1.2 Experiment

In the real experiment[2] (see Fig. 4.3), such approximations as discussed above are not entirely easily to realize. The main challenge is to provide a plane homogeneous phase front of incident electromagnetic THz radiation. At the velocity-matching condition, we can still observe a residual deflection [36], see Fig. 4.4. A 90-keV electron beam is focused onto the detector through the 70-nm-thick aluminum foil. The incoming electron pulse duration[3] was ∼800 fs. The sample-detector distance is 68 cm. By scanning the delay τ between the arrival times of the THz and the electron pulses, we acquire snapshots of the electron distribution at the detector. The images are averaged and normalized along the undeflected direction, forming one-dimensional beam profiles, and put together with respect to the time delay, resulting in a deflectogram[4] (see Fig. 4.4). A more detailed analysis of deflectograms is discussed in Subsection 4.2.3. A tiny but reproducible transversal momentum gain is obvious, however, the amplitude is small, as predicted by expression (4.7) at conditions close to the velocity matching.

The relative THz-electron angle is $\theta \approx 33°$. The electron beam size at the foil is ∼300 µm, which is roughly one-third of the central wavelength λ of the THz pulse. To

---

[2] The experiment was performed in collaboration with Dr. Waldemar Schneider.

[3] The electron pulse duration was measured with the same technique as discussed in Subection 4.2.3.

[4] The term “deflectogram” was chosen for such data to show both similarities and differences with attosecond spectrograms. The data contains both electromagnetic and electron pulse information, but mathematically the deflectogram can be expressed in slightly different way (see expression (4.9) in Subsection 4.2.3). The reconstruction procedure is discussed in the same subsection.

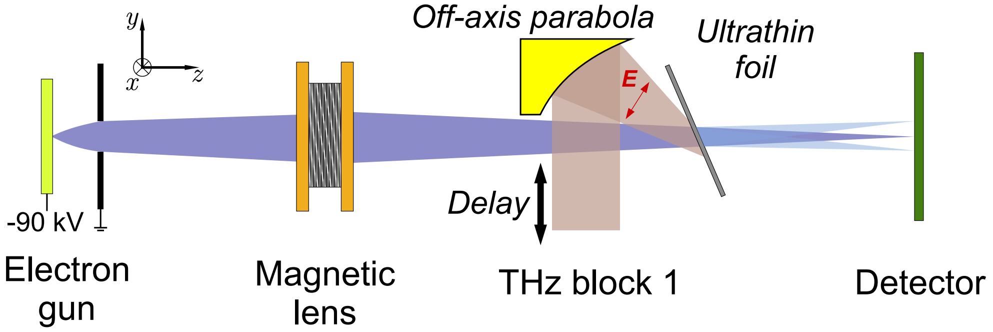

Figure 4.3: *Deflection at thin foil: experimental setup schematic.* A 90-keV electron beam is focused with a magnetic lens onto a screen trough a 70-nm aluminum foil. A THz beam from "THz block 1" is focused onto the foil by an off-axis parabola, making a spot with the size of <3 mm (full width at half maximum).

have an as high as possible field amplitude within the light-electron intersection area, the THz pulse from "THz block 1" (see Section 3.1) is guided into the vacuum chamber through a silicon window and focused onto the foil by an off-axis parabola to a size of close to λ. Thus, the Gaussian beam approximation is not entirely valid and spatio-temporal phase can play a significant role, not only at the surface but also on the way to it. To minimize such effects, it is necessary to either produce a smaller electron beam at the foil, or to have a reasonably large THz focus size.

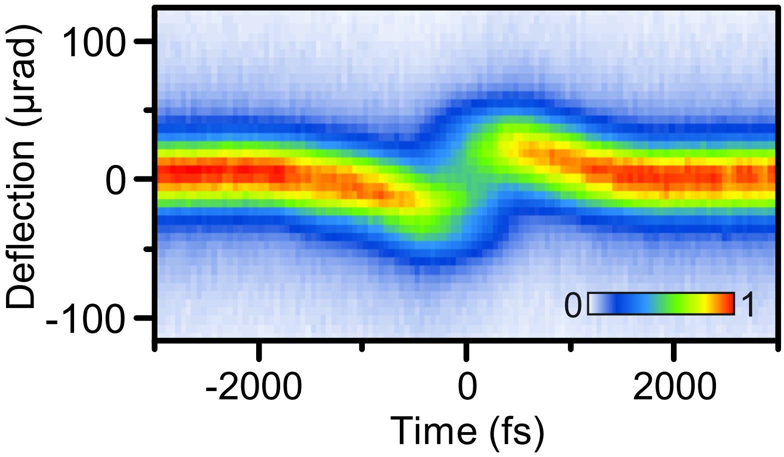

Figure 4.4: *Deflection at thin foil: deflectogram.* Deflectogram, acquired via deflection of the electron pulse by the THz field at the 70-nm aluminum foil. The figure is taken from [36].

4.2 THz deflection in resonators of various shapes

While an ultrathin foil is perfect for longitudinal momentum gain, which can be used for compression, the characterization by streaking requires time-dependent sideways momentum [36]. Here, we study several approaches to achieve this. An abrupt interaction of the electron with THz fields can be realized by using sub-wavelength hole structures. Such structures have been attracting attention over several decades, since relations between extraordinary optical transmission and both localized and surface plasmons[5] were revealed [64–67]; now these elements find applications in sensing and as tunable plasmonic components of metamaterials [68–70].

Consider now the same plane wave reflection geometry discussed in Section 4.1 (see Fig. 4.1) but with the foil having a sub-wavelength hole perforated in it along the z-axis. Here, the deflection of an electron propagating through the structure is not compensated, even in a collinear scheme in contrast to the previous section (see equation (4.7)), because the reflected wave has amplitude and phase deviations from the incident one due to not ideal reflection from the perforated metal foil and field penetration through the hole. Moreover, if the structure has a resonance to the incident field, a localized plasmon can be excited, which then irradiates into free space and can have field enhancement in certain locations of the structure. If the enhanced field has an amplitude higher than those amplitude deviations, then the deflection of the electron can be described by equation (2.18). The field inside a drilled hole is localized, however, it penetrates outwards. For a foil thickness of less than $\sim$100 µm, the transition time of the electron pulse in the experiment is shorter than the period of the THz excitation wave anyway and we can apply the definitions given by assumption (III) in Section 2.3. For designing different holes' geometries, a software for 3D electromagnetic simulation (CST Microwave studio, CST GmbH) was used.

With a tightly focused or collimated beam of a diameter less or of the same order as the field inhomogeneity, it is possible to probe the local field of the localized plasmon inside the structure. Basically, this simple device is a streak camera [71], where the streaking field is excited by the THz pulse, and varying temporal delay between the THz and the electron pulses provides information about the response of a sub-wavelength structure. In Subsection 4.2.3, devoted to the electron pulse characterization, the resolution of the THz streak camera is discussed in detail.

In this work, individual holes are investigated, which were cut into the 30-µm aluminum foil with a laser-drilling machine. By adjusting the hole size and shape, it is possible to set a resonance condition for the incident electromagnetic pulse and enhance the field inside such structure. In contrast to the deflection at the ultrathin metal foil, where the electron and the THz pulse have a relative angle for an efficient momentum transfer, here both beams can be collinear and have zero incidence angle at the foil with the sub-wavelength resonator. In this section, experimental results of electron control are presented, that were used for designing of a streak camera with a resolution of 10 fs.

---

[5] Surface plasmons are coherent delocalized electron oscillations that exist at the interface between any two materials where the real part of the dielectric function changes sign across the interface (e.g. a metal-dielectric interface, such as a metal sheet in air).

The experimental setup is schematically shown in Fig. 4.5. The electron gun operates at 70 kV, the solenoid lens (ML1) is placed 14 cm after the anode, the second lens (ML2) is positioned ∼30 cm after ML1. Both coils are adjusted to produce a rather collimated beam with a diameter of 16 µm in the y-direction and 9 µm in the x-direction (full width at half maximum). Collimated electrons pass through a hole drilled into an off-axis parabola mirror with a focal distance of 5 cm, which focuses the THz beam from “THz block 1” with close to normal incidence onto a certain sub-wavelength structure at the foil. Structures are located in such a way that an interaction between each other is excluded. The electron beam can be steered by two pairs of coils placed after ML2. The distances from ML2 to the sample and from the sample to the detection camera are ∼35 cm and ∼55 cm, respectively. From the deflection experiment, we obtain spatial displacement of the electron beam at the screen, which can be converted to the angular deflection through dividing by the sample-detector distance.

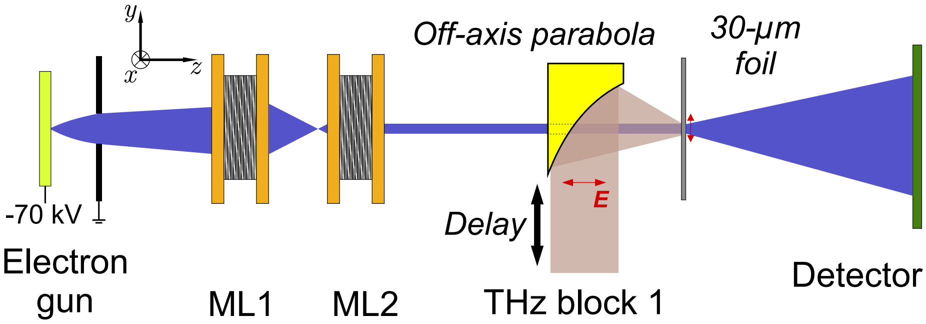

Figure 4.5: *Deflection at sub-wavelength structure: experimental setup schematic.* A 70-keV electron beam is collimated by a pair of magnetic lenses ML1 and ML2 to a beam size of ∼16 µm. The electrons pass an off-axis parabolic mirror, which focuses THz radiation from “THz block 1”, through a drilled ∼3 mm hole. A 30-µm foil with laser-drilled sub-wavelength structure has a close to normal incidence angle for both the electrons and THz pulse.

4.2.1 Single-mode slit reonator

The THz excitation pulse is polarized along the y-axis at the sample and the sub-wavelength structures, which are under consideration in this subsection, are aligned such that they exhibit an enhancement of the resonance fields along y-direction. Fig. 4.6B depicts a microscopic image of the slit resonator with dimensions of 230 µm and 120 µm in width and height, respectively (a single-mode TE resonator). Fig. 4.6A shows a set of raw images at different temporal delays, at which the electron pulse passes through the center of the rectangular hole and interacts with a localized field at the structure. The electron beam deflection in the x-direction is negligible, and we acquire a deflectogram (see Fig. 4.6C). While the electron beam diameter is smaller or of the same order as the confined field

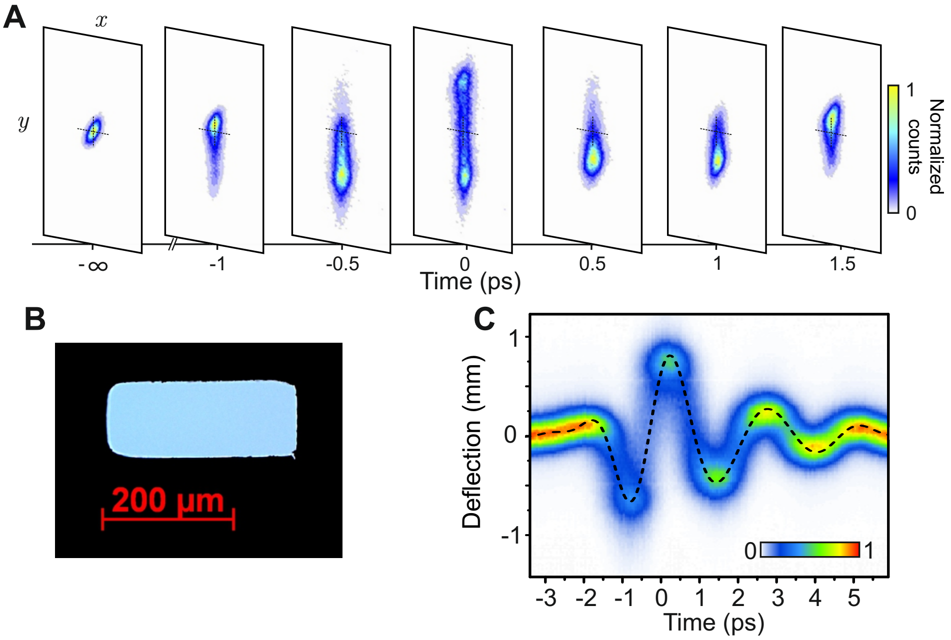

Figure 4.6: *Deflection at single-mode slit sub-wavelength structure.* (A) Raw images of the pump-probe experiment in the single-mode slit resonator. (B) Microscopic photo of the single-mode rectangle resonator. (C) Deflectogram of the single-mode slit resonator. The evaluated deflection field in the center of the resonator is shown by a dashed black line.

inhomogeneity, the measurement gives information about the electron pulse duration and the local field strength and direction[6].

To analyze the deflectogram's signal, we invoke an iterative algorithm, described in Subsection 4.2.3. The signal retrieved from the deflectogram is proportional to an effective field at a local spatial position (see expression (2.18)), which consists of an average contribution of different modes (see the black dashed line in Fig. 4.6C). For the single-mode slit, however, this data reveals the damping of the mode and its central frequency, which are $\gamma \approx 0.47\,\text{THz}$ and $f_0 = 0.43\,\text{THz}$, respectively[7].

4.2.2 Multi-mode slit reonator

The same experimental scheme is realized with a multi-mode slit resonator with dimensions of 730 µm (width) and 100 µm (height), see the inset of Fig. 4.7A, which can support more than one mode in the excitation spectrum (see Fig. 3.2). Fig. 4.7A depicts the resulting deflectogram and the evaluated field trace (black dashed line). In the single-mode slit

---

[6] This method can be applied for the microscopy of electromagnetic waveforms. However, the experimental setup does not provide precise enough control of the electron beam position and diameter. Besides, the amount of points to be probed has to be very large in order to provide with any decent spatial resolution, although, using a mask to produce an array/matrix of small electron beams can improve the measurement and make this method very efficient.

[7] Damping is defined as an exponential coefficient γ in $e^{-\gamma\tau}$.

resonator, the transversal magnetic field components approach zero in the center, giving an opportunity to record the almost bare electric field, because a longitudinal magnetic component does not deflect a well-collimated beam. Although, in a multi-mode slit resonator the magnetic field distribution differs from that in a single-mode slit, it remains negligible at the center. Because the electron probe beam enters the slit in the center, some modes, which have knots in this region, can escape from observation.

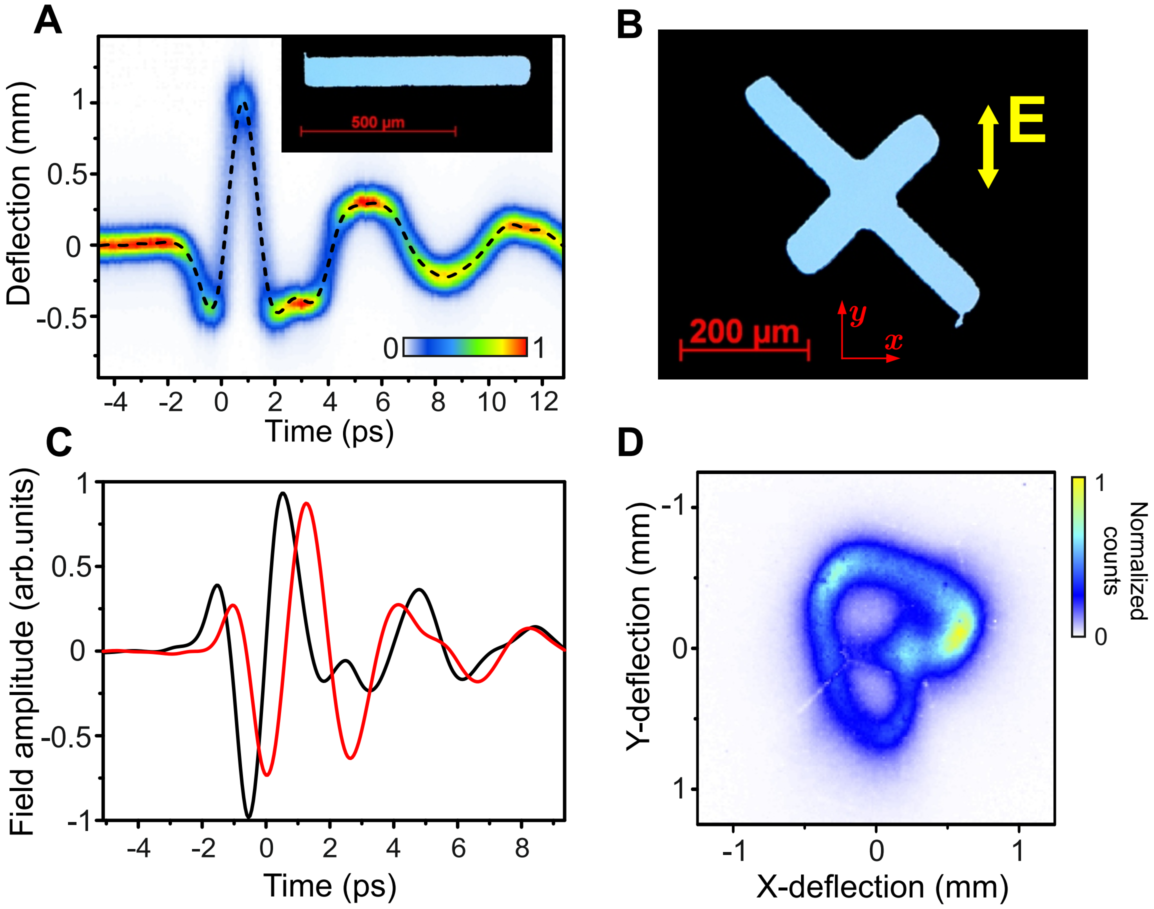

Figure 4.7: *Deflection at multi-mode sub-wavelength structures.* (A) Deflectogram of the multi-mode slit, an inset shows its microscopic photo. A dashed line depicts the evaluated deflection field. (B) A microscopic photo of the cross-shaped sub-wavelength structure. A yellow arrow shows a THz polarization. (C) Evaluated field components at the center of the cross structure: a black curve shows the y-component, a red curve shows the x-component. (D) Lissajous figure drawn by the electron beam. The image is formed from a sum of snapshots at time delays between -0.3 ps and 2.4 ps.

Multi-slit resonators have very pronounced modes, however, the field direction is determined by the geometry. In an attempt to spatially separate deflections of different modes, a “cross-shaped” structure was studied. It is constructed of two perpendicular slit holes that intersect each other in the center (see Fig. 4.7B). The electron beam passes through the center of the cross. If the excitation pulse field polarization is not parallel to one of the sample's slits, and if the slits have slightly detuned resonances from one another, then the deflection occurs not in one plane and the electron beam can "draw" a Lissajous figure, similar to a beam in an oscilloscope (see Fig. 4.7D). The image is a normalized sum of electron density snapshots in the interval between -0.3 ps and 2.4 ps. Such a cross-system response can be described as a multi-mode oscillator with two damping coefficients and an external excitation. We can evaluate the effective field inside the cross and find phase offsets between local plasmon oscillations (see Fig. 4.7C).

4.2.3 Bowtie resonator: electron pulse and THz signal characterization

The key component of a high-resolution streak camera is a high spatial and temporal gradient of the field [72]. Among sub-wavelength structures with different shapes and sizes, a standout one is the so-called bowtie[8] shape [73]. An advantage of this shape is a strong localization of the field within a small area, hence it exhibits a high field enhancement and a more pronounced mode to produce a temporal field gradient. To have good coupling between an excitation pulse and a resonant structure, its main eigenmode must be tuned according to the peak of incident signal spectrum (~0.3 THz). Not only enhancement is important, but also the homogeneity of the field within the area of the electron beam transmission, otherwise, the problem of field reconstruction from a deflectogram becomes more complex. The optimal sizes of the bowtie resonator are determined from numerical simulations[9] (see Fig 4.8C). The electron beam is spatially aligned to pass through the center of the bowtie.

The deflection of the electron in a sub-wavelength resonator with field-enhancement can be described by expression (2.18), thus the streaking signal will reproduce the shape of the field inside the structure (instantaneous regime). This stands in contrast to attosecond streaking of extreme-ultraviolet pulses in gases or at bulk surfaces, where the transition time of the electron is longer than a field oscillation period, thus the streaking signal follows the integral of the field, i.e., the vector potential[10] [75].

The technical resolution of a streak camera ΔT is given by $\Delta T = \Delta X / V$ [76], where ΔX, in our case, is the electron beam width and V is the streaking speed, i.e., the temporal slope of the local field. A pinhole[11] with a diameter of 50 µm is placed ~100 mm before the bowtie resonator in order to improve electron beam emittance and the resolution of the streaking camera at the expense of a reduced electron flux. The focus of the beam lies between the streaker and detector, at which positions the beam diameter is 11 µm and 23 µm, respectively (both values are root mean square). In the current experiment, the instrumental resolution is below 20 fs (root mean square), but the presence of timing

---

[8] In some literature it is called butterfly shape.

[9] CST Microwave studio, CST GmbH.

[10] Instantaneous regime of extreme-ultraviolet pulse streaking also can be realized by nanoplasmonic field [74].

[11] The pinhole was installed by Dominik Ehberger and Dr. Catherine Kealhofer. This greatly increased the resolution of the streaking, enabling to measure sub-100-fs pulses, which has been achieved afterwards.

fluctuations can worsen it. However, due to the optical synchronization, their impact is smaller than the resolution limit of the streaker (see Section 4.3).

Fig. 4.8A depicts the experimentally acquired deflectogram. The electron pulse duration and the local effective (longitudinally averaged, see Section 2.3) THz field are contained in the deflectogram data. To roughly estimate the pulse duration, one can analyze a time-delay slice at the maximum linear slope of the deflectogram, by determining its width (in µm) and dividing by the slope steepness (in µm/ps) or by evaluating the temporal width of the slope.

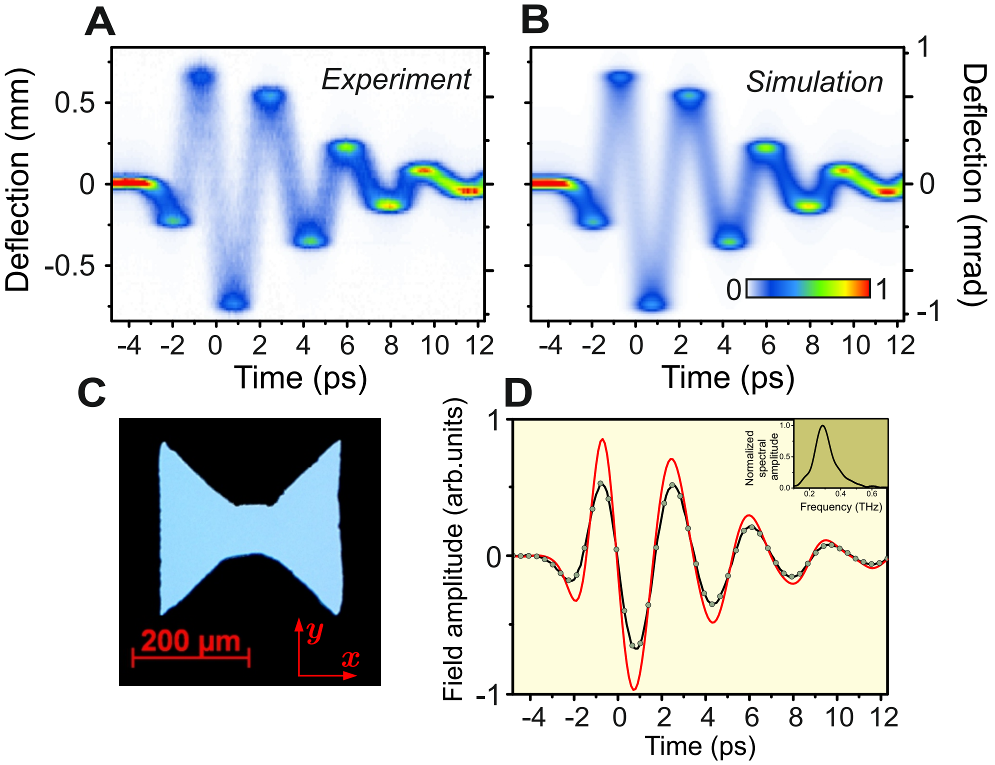

Figure 4.8: *Streaking and characterization of electron beam at bowtie sub-wavelength structure.* (A) Experimental deflectrogram, acquired with the bowtie structure. (B) Simulated deflectogram. (C) Microscopic photo of the bowtie structure. (D) Evaluated field (red solid line), the first center-of-mass guess (black solid line) and the initial parameter values (green circles). The inset shows the spectrum of the evaluated field.

To increase the evaluation precision, we apply an iterative algorithm analysis to reconstruct the electron pulse duration/envelope and the local THz field at the sub-wavelength resonator simultaneously. In general, applying a Levenberg-Marquardt algorithm, we minimize the squared difference between the experimental and simulated deflectogram by varying parameters that are used to calculate the deflection curve $f(t)$ and the electron pulse's temporal shape $e(t)$. The simulated deflectogram $D(x,\tau)$ can be expressed as:

$$D(x,\tau) = \int\limits_{-\infty}^{\infty} r(x - f(t+\tau))\, e(t)\, dt \approx \sum_{i=0}^{G} r(x - f(t_i+\tau))\, e(t_i), \tag{4.9}$$

where $r(x)$ is the one-dimensional undeflected beam profile and G is the time-grid size, on which $e(t_i)$ is defined. Note that $f(t)$ can be associated with the field in instantaneous deflection assumption, which is applied here, or with the vector potential, i.e., without the assumption. The parameters for $f(t)$ serve as cubic spline points, and $e(t)$ can either be expressed with one parameter, the pulse duration (for a Gaussian-shape pulse assumption), or with multiple parameters that characterize the pulse envelope. The resulting simulated deflectogram is shown in Fig. 4.8B. Fig. 4.8D depicts the evaluated field (solid red line), the center-of-mass first guess fit of the experimental deflectogram (solid black line) and the initial values of the parameter points for $f(t)$ (green circles). A simple frequency filter can be introduced in the fitting function in order to reduce high-frequency noise. The evaluated electron pulse duration (for a Gaussian pulse envelope assumption) is 930 fs (full width at half maximum). This approach gives very good results for more or less homogeneous field distributions within the area of the electron beam transmission, otherwise the beam profile even of an extremely short electron pulse would be distorted during the deflection and the error of the fit would increase.

4.3 THz compression concept

To have better resolution in a pump-probe experiment, it is preferable to have a probe pulse duration shorter than that of the pump pulse, especially, when a sub-cycle resolution has to be achieved. In our case, the electron pulse has a duration of 930 fs, thus the resolution of the a sub-cycle measurement would suffer a lot, making the data evaluation difficult. However, electron pulses can be compressed by the techniques discussed in the beginning of this chapter. In the current work, the THz pulse generated by the same laser pulse as the singe-electron pulse is utilized to compress the latter down to the sub-100-fs regime.

It was theoretically shown in Section 4.1 how to transfer longitudinal momentum to electrons in the beam at the ultrathin metal foil. Assume the electron pulse duration is shorter than a half-cycle of the electromagnetic pulse. If the temporal delay between the electron pulse and the incident electromagnetic pulse is set in a way that the center of the electron pulse passes the foil, when the longitudinal field component approaches zero (a so-called "time-zero" or "zero-crossing"), the electron pulse's front is decelerated by the field and its tail is accelerated. The electron pulse obtains a negative chirp and, after a certain distance, it compresses itself due to dispersion in vacuum [38] (see Fig. 4.9A). If the field is linear in time over the entire duration of the electron pulse, the pulse obtains a linear negative chirp and, theoretically, can be compressed to the attosecond durations [38].

But different factors, for example, a nonlinearity of the field, inhomogeneities of the field inside electron optics, timing jitter between the pulses, multi-electron pulse generation and etc., set a limit for single-electron pulse compression [40, 59].

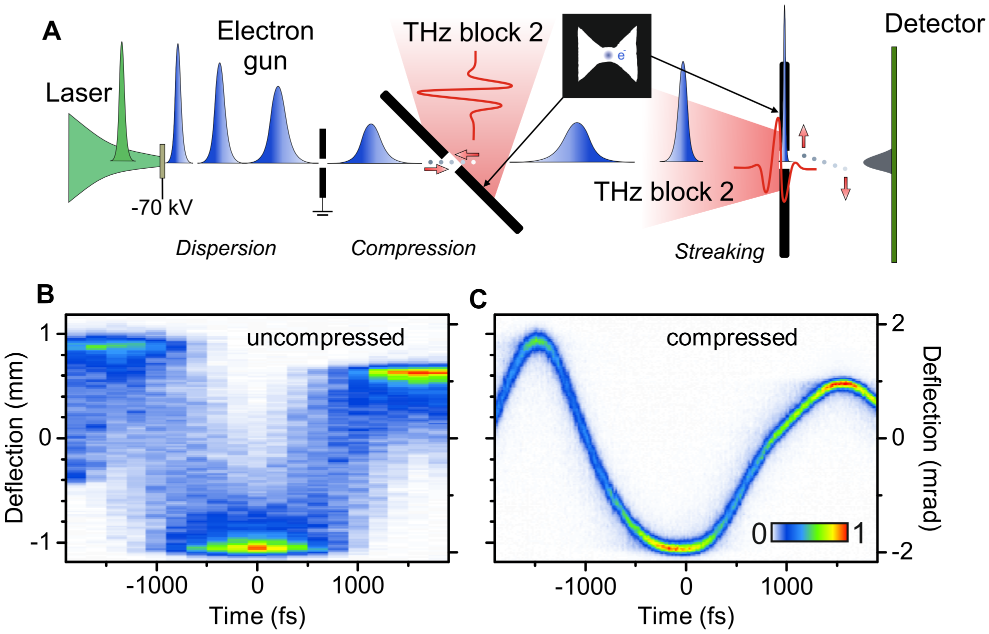

Figure 4.9: *Electron pulse compression with bowtie sub-wavelength structure.* (A) Schematics of the compression and streaking of the electron pulse. Electrons in a single-electron pulse are dispersed via acceleration in the electron gun (see Section 3.2). Higher-energetic electrons are marked as light blue under the pulse envelope, lower-energetic are dark blue. By passing through the first bowtie structure, which is tilted with respect to the electron trajectory, at zero-crossing of the THz field inside, the tail of the electron pulse gains longitudinal momentum, while the front loses it, as shown with red arrows. By setting an appropriate THz field peak amplitude, the electron pulse is compressed at the position of the streaking stage [36]. At this stage, the electrons are deflected by the field inside the second bowtie structure (the streaker). (B) Deflectogram of the uncompressed electron pulse. (C) Deflectogram of the compressed electron pulse. The figures (B) and (C) are take from [36].

An ultrathin foil acts as an excellent instrument for electron pulse compression, however, if a high THz amplitude is not available, a sub-wavelength structure can be utilized due to its field enhancement inside. In the experiment, we used a bowtie resonator[12], which is tilted in such a way that the enhanced field inside the resonator has a component parallel to the electron propagation direction. This provides a longitudinal oscillating electric field component with a strong slope, which can both accelerate or decelerate electrons within an electron pulse (see Fig. 4.9A). By varying the compression field amplitude, we can change the so-called "temporal focus" of the compressor, i.e., the position, where the electron pulse has the shortest duration [36].

---

[12] The compression bowtie structure has the same dimensions as the bowtie used for streaking, see Subsection 4.2.3.

As it is shown in Subsection 4.2.3, there is a quasi-linear part of the excited field inside the bowtie resonator, from -0.4 ps to 0.4 ps (see Fig. 4.8D). The initial pulse duration of ∼930 fs (full width at half maximum) exceeds the linear region of the compression field, which introduces nonlinear chirp in the pulse, hence making the compression less efficient. Fig. 4.9A presents a schematic of the experimental setup for the compression and characterization. The electron pulse is focused into the bowtie compressor with the first magnetic lens, and afterwards it is softly focused between the streaking element and the camera screen with the second magnetic lens as it is shown in Subsection 4.2.3. The deflectograms of the uncompressed and compressed electron pulses are show in Fig. 4.9B and Fig. 4.9C, respectively. The compressed electron pulse duration is 75 ± 10 fs (full width at half maximum) [36].

In [59,63], it is shown how timing jitter and long-term drifts between the electron pulse arrival at the compression stage and into at streaking stage, as well as amplitude fluctuations of the compression and streaking can dramatically worsen not only the resolution but also the advantage of using compression altogether. With the all-optical concept, where the compression and streaking fields are naturally synchronized to the electron pulse generation via the same laser pulse, the timing jitter can be improved passively, reaching values of <5 fs (root mean square) [36], meaning that measurements of electromagnetic waveforms by electron microscopy in the THz frequency range will not suffer from timing jitter and drifts.

The experimental results, that are discussed in this section, were obtained in collaboration with Dr. Catherine Kealhofer and Dominik Ehberger and serve as a basis for the electron microscopy of electromagnetic waveforms.

Chapter 5

Electron microscopy of electromagnetic waveforms: experiment

This chapter describes the main experimental setup, which is combined from the elements discussed in Chapters 3 and 4. Before the data acquisition, some preparation procedures are performed, such as the electron pulse duration measurement and calibration of the excitation field time-zero.

The experimental setup for electron microscopy of electromagnetic waveforms is schematically depicted in Fig. 5.1. The electrons are generated with a frequency-doubled femtosecond laser pulse (see Section 3.1) and accelerated from the cathode to a kinetic energy of 70 keV in the electron gun (see Section 3.2). The first magnetic solenoid, positioned 14 cm after the anode, focuses the electron beam into the bowtie structure, which is used for electron pulse compression (see Section 4.3). The second magnetic lens, located 9.5 cm after the compressor, acts as a collimator, producing a beam with a diameter of ~810 µm (full width at half maximum). The electron beam size is made large enough to illuminate an entire sub-wavelength structure with a sufficient electron intensity. From the source emittance (see Section 3.2), we conclude a divergence angle of $\alpha_{\mathrm{div}} \approx 60\,\mu\mathrm{rad}$. The sample, a 30-µm aluminum foil with holes of different shapes, laser-drilled through the metal, is positioned 49 cm after the compression stage. Most of the holes are designed to be resonant to the THz excitation spectrum (see Fig. 3.2). The third solenoid lens, placed 28 cm after the sample, magnifies the distorted electron images onto a phosphor screen of a detector; the sample-screen distance is 134 cm. The camera has a minimal acquisition time of one second. The complete scan of 150×16 images (150 time steps, 16 field strengths; see Chapter 6) would take ~1 hour. However, due to the presence of some detrimental correlated 50-Hz noise in the lab due to electrical cables in the basement, a chopping wheel was installed in the frequency-doubled beam line and synchronized with the line frequency. We set the duty cycle to 20% of average power transmission, which increased the measurement time to ~5 hours but sufficiently suppressed the broadening and oscillation of the electron beam. In order to perform a scan with compressed electron pulses, two motorized stages are moved synchronously: one sets the delay of the emitted electrons with respect to the

THz excitation pulse, another maintains the zero-crossing of the compression field with respect to the arrival time of the electron pulse at the compressor.

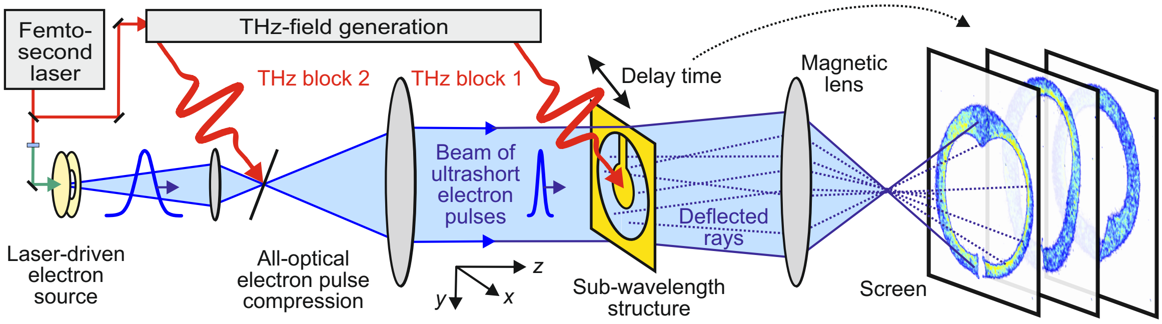

Figure 5.1: *Electron microscopy of electromagnetic waveforms: experimental setup.* After the electron gun, electrons are focused with the first lens into the bowtie compressor and then collimated with the second lens. The compressed electron pulse, which is delayed in time, is transmitted through the sample. The third lens magnifies the beam and projects a magnified shadow image. The figure is adapted from [31].

To characterize the electron pulse duration, it is required to place a streaking element at the sample's position (see Section 4.2). In our case, we use the bowtie element discussed in Subsection 4.2.3 for electron streaking. The difference from the measurements discussed in Section 4.3 is that we are not able to focus the electron beam into the streaking element, because it would change the overall electron path length to the sample, i.e., the temporal focus would be shifted. To perform a measurement and record a deflectogram with the collimated electron beam, we can either use a pinhole to let only a small part of the beam to pass through a quasi-homogeneous streaking field in the center of the resonator, or we do not mask the beam and illuminate the streaking element completely. The drawback of the first approach is a reduced signal and thus increased measurement time; the disadvantage of the second approach is a decrease in resolution, because overlapping electrons from different parts of the streaker distort the beam on the screen and introduce systematic error into the pulse duration evaluation. Nevertheless, for the electron pulse duration obtained in Section 4.3, the choice of the approach does not play a significant role for the resolution. Figure 5.2A depicts the deflectogram acquired with the full illumination of the streaking resonator[1], the retrieved pulse duration $\tau_{\text{electron}} = 80 \pm 20$ fs.

One way to record the electron microscopy data is a "linear-field approach" (see Section 6.2). The peak amplitude of the THz excitation field is swept at each pump-probe delay step. This is required to record a set of deflected images, i.e., the electron density evolution, for further evaluation of the time-dependent field distribution (see Section 6.2). To set the THz field amplitude, we vary the power of the laser pulse pumping the LN crystal (see Section 3.1), using a thin-film polarizer and a motorized rotary stage with a half-wave plate. The THz generation via optical rectification is a second-order nonlinear

---

[1] We analyze the signal in the image area, restrained in the x-directions by the width of the central bowtie part.

process, thus the THz field amplitude is proportional to the pump power (see Fig. 5.2B). The drawback of the pump power sweeping approach is the appearance of a correlated zero-crossing shift, i.e., the delay between the THz excitation pulse and the electron arrival changes at different pump powers (see Fig 5.2C). This is probably due to thermal effects and is compensated in the experiment optomechanically by adjusting the motorized stages according to a previously measured zero-crossing calibration curve (see Fig 5.2C).

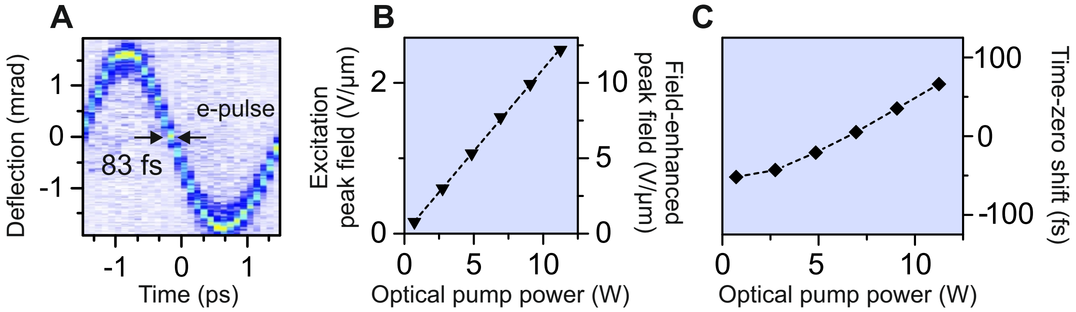

Figure 5.2: *Electron pulse duration measurement and zero-crossing shift.* (A) Electron pulse duration measurement with a collimated beam using the bowtie resonator. The evaluation is done by measuring the slope width of the acquired deflectogram. (B) Dependence of the THz pulse amplitude and the THz field in the center of the streaking bowtie resonator (see Subsection 4.2.3) versus the infrared pump power. (C) Pump-power-dependent zero-crossing shift. This shift indicates a relative displacement of the deflectogram's zero-crossing, measured at different laser pump powers in "THz block 1". All figures are taken from [31].

Chapter 6

Electron microscopy of electromagnetic waveforms: data and analysis

Field reconstruction in electron microscopy is an inverse non-bijective problem: after interaction with the electromagnetic dynamics in the sample, particles can overlap and, after detection, it is not directly possible to find the initial state of their position and velocity. This chapter introduces two main techniques of obtaining experimental data and its analysis in order to reconstruct the local spatio-temporal dynamics, excited by an electromagnetic pulse. We discuss the limits of spatial resolution (the smallest resolvable length scale at the sample) and angular resolution (the smallest resolvable field amplitude) of these techniques.

6.1 Inverse non-bijective problem

Consider in the first case a *discrete* two-dimensional distribution of particles with only a longitudinal velocity component v_z (the same concept and approximations as presented in Chapter 2). By passing through an infinitely thin region (a sample plane) along the z-axis (see Fig. 6.1A), each particle is instantaneously deflected (approximation $v_{x,y} \ll v_z$, $v_z = \text{const.}$) and hits the screen after a certain propagation distance. To find the transversal velocity components v_x and v_y of the deflected particles, it is, in principle, enough to have two snapshots of the particles positions: before the sample (initial distribution) and at a position Δz after the sample, where $\Delta z \to 0$ (we assume an infinite spatial resolution of the detector). Overlaps have not occurred yet and we can write the kinematic equations for each particle:

$$\begin{cases} v_{xi} = \dfrac{x_i - \xi_i}{\Delta z} v_z = \alpha_{xi}\, v_z; \\ v_{yi} = \dfrac{y_i - \eta_i}{\Delta z} v_z = \alpha_{yi}\, v_z, \end{cases} \tag{6.1}$$

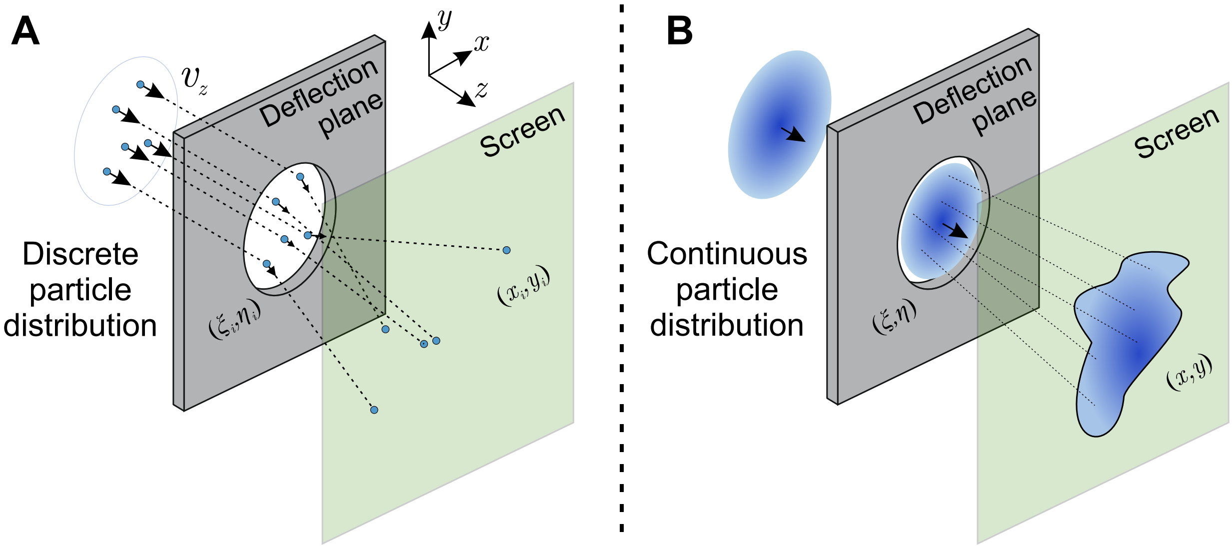

Figure 6.1: *Instantaneous deflection of particle density distribution.* (A) Discrete two-dimensional particle distribution with initial longitudinal velocity v_z is instantaneously deflected in the thin sample and then detected at the screen of a detector. (B) Continuous two-dimensional particle distribution with initial longitudinal velocity v_z is instantaneously deflected in the thin sample and then detected at the screen of a detector.

where α_{xi} and α_{yi} are deflection angles in x- and y-directions, respectively, ξ_i and η_i are initial x- and y-coordinates, respectively, and the index i corresponds to the i^{th} particle. In equation (6.1) we used the small angle approximation.

On the other hand, we can have a snapshot of the initial particle positions and two snapshots at position z and $z+\Delta z$ positions, from which we can determine the velocities and trace the particles back to their initial positions, defined by the initial discrete distribution. By introducing a limited spatial resolution and by increasing the number of particles, velocimetry techniques can be used to find transversal velocities [77]. The essence of these techniques is tracking particles that are distinct from each other and from the environment. The technique can fail if there are too many particles, overlaps, bad resolution and a low signal-to-noise ratio, when it is not possible to distinguish between individual particles.

Consider in the second case a *continuous* two-dimensional distribution of particles using the above geometry and assumptions (see Fig. 6.1B), propagating with a longitudinal velocity v_z towards a deflection plane (the term *continuous* means that the number of particles is so big that the detector is not capable of detecting single particles but rather a particle density). The tracking of individual particles that are indistinguishable is not possible and requires to work with density distributions. At a moment in time $t_0 = 0$ in the deflection plane, consider a particle density distribution $\rho(\xi,\eta)$, where $\xi = x(0)$ and $\eta = y(0)$ are Lagrangian coordinates[1], and two components of the initial velocity distri-

---

[1] Lagrangian coordinates are coordinates of individual particles in the evolution of a particle distribution while Euler coordinates are coordinates that are fixed to a certain reference system.

butions $V_x(\xi,\eta)$ and $V_y(\xi,\eta)$. The velocity distributions can be transformed into angular distributions $A_x(\xi,\eta) = V_x(\xi,\eta)/v_z$ and $A_y(\xi,\eta) = V_y(\xi,\eta)/v_z$, using the small angle approximation. After the deflection, an evolution of the density can be described by $\rho(x,y,t)$ in Euler coordinates [78]:

$$\begin{cases} x(t) = \xi + V_x(\xi,\eta)\,t; \\ y(t) = \eta + V_y(\xi,\eta)\,t; \end{cases} \Leftrightarrow \begin{cases} x(z) = \xi + A_x(\xi,\eta)\,z; \\ y(z) = \eta + A_y(\xi,\eta)\,z, \end{cases} \tag{6.2}$$

where $z = v_z\,t$ denotes the longitudinal position of the two-dimensional particle distribution.

As the overall number of particles is conserved, we can write:

$$\rho(x,y,t)|_{z=v_z t}\;dxdy = \rho(x,y,z)dxdy = \rho(\xi,\eta)d\xi d\eta \quad \text{or} \tag{6.3}$$

$$\rho(x,y,z) = \rho(\xi,\eta)\left|\frac{D(x,y)}{D(\xi,\nu)}\right|^{-1}, \tag{6.4}$$

where $\left|\frac{D(x,y)}{D(\xi,\nu)}\right|$ is a Jacobian, which acts as a coefficient of area distortions. In the general case, the velocity maps are such that the overlaps can take place immediately after the deflection, which means that $\left|\frac{D(x,y)}{D(\xi,\nu)}\right| = 0$ and $\rho(x,y,z) \to \infty$. The problem of finding $A_x(\xi,\eta)$ and $A_y(\xi,\eta)$ becomes strongly bijective and impossible to solve using analytical equations.

The model of a *continuous* distribution describes the electron imaging of electromagnetic waveforms: at a certain time-delay step, with respect to a deflection field, an electron enters a sample at a certain transversal position with a longitudinal velocity v_z (or v_e), then it is deflected by the fields inside the sample and afterwards detected at the screen of a detector. To collect enough statistics of the process, $10^4 - 10^6$ electrons have to pass through the sample at different transversal positions, which creates a quasi-continuous density distribution at the screen. A decently small acquisition time for sufficient statistics is achieved by a high-repetition rate laser, which generates both free single-electron and electromagnetic pulses used for sample excitation (in our case, an electromagnetic pulse in the THz frequency range, see Section 3.1). A pulse duration of a single-electron pulse after passing through a compression stage (see Section 4.3) is much shorter than the temporal oscillation period of any electromagnetic dynamics at the sample (see Sections 2.1 and 2.2), which enables electron deflection by time-frozen fields (see Section 2.3). The transversal positions of the electrons before entering the sample are described by the initial electron distribution, and the initial transversal velocities can be minimized by producing a well-collimated beam with electron optical elements (magnetic lenses). Basically, we are able to detect two sets of electron distributions: the initial distribution, when the fields inside the sample are switched off, and the electron distribution after the interaction with the electromagnetic dynamics, when the fields are on. As it is mentioned above, due to overlaps of the electrons between the sample and the detector, there is no analytical solution. However, our approach is based on recording a *discrete evolution of electron density* $\rho(x, y, z_i)$, where z_i is a certain longitudinal position of the detector, which is equivalent to a variation of the excitation amplitude or changing the focal length of the objective lens (see Sections 6.2 and 6.3). As it is shown below, it allows to unambiguously find the angular distributions $A_{x,y}(\xi, \eta)$ in the sample and, thus, recover the field distribution of the dynamics in space, time and vectorial direction. In the following sections, different approaches to record the discrete evolution of electron density are shown and a reconstruction procedure is described in detail.

6.2 Linear-field approach

In a real electron imaging experiment, we face the problem that it is instrumentally inconvenient or impossible to take snapshots at different longitudinal positions along the z-axis because the camera is usually fixed to a certain location. In Fig. 6.2, a linear-field approach principle is depicted. Assuming small deflection angles, which is fair for this experiment, a displacement of an electron x_j at different screen positions L_j is equal to the product of an angle α and L_j. However, instead of varying L_j (Fig. 6.2A), we can vary α_j (Fig. 6.2B) and have a constant screen position L:

$$x_j = \alpha L_j = \gamma_j \alpha \, L = \alpha_j L. \tag{6.5}$$

As a result, a discrete evolution of the particle density distribution is obtained without moving the screen. The angle α_j (i.e., the components of $\mathbf{A}(\xi, \eta)$) can be varied by the global amplitude of the electromagnetic dynamics; thus, this approach is based on the linear relation between the amplitude of the excitation signal and the amplitude of the fields inside the sample.

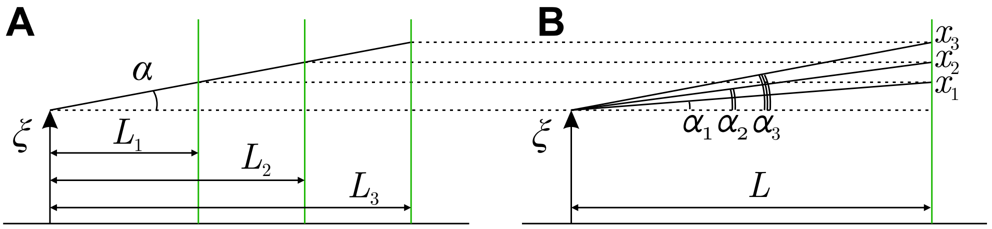

Figure 6.2: *Schematic of linear-field approach.* (A) Electron's position at the screen after the deflection at different detector positions. (B) Electron's position at the screen after different deflections at the fixed detector position L.

Having a lens (or set of lenses) between the deflection plane (the sample) and the screen, the deflection also maintains such linear behavior due to the linear bijective magnification

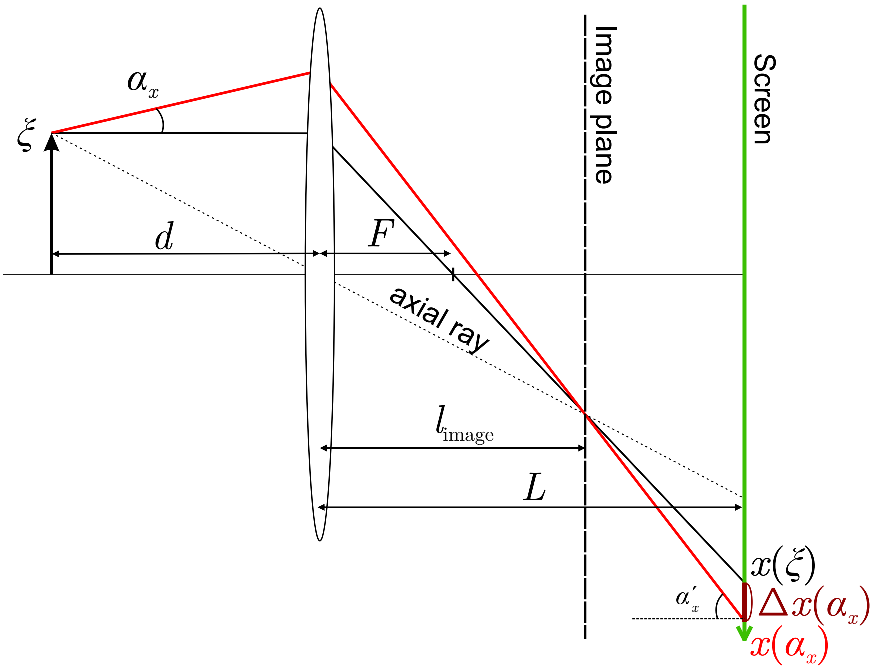

Figure 6.3: *Schematic of linear-field approach with single lens.* The solid black line shows the ray path with no deflection and the solid red line depicts the electron ray deflected by α_x. The distances from the deflection (object) plane (ξ) to the lens and from the lens to the screen are d and L, respectively; l_{image} is the distance from the lens to the image plane; ξ and x are the ray coordinates in the deflection (object) plane and in the screen plane, respectively; Δx corresponds to the screen position shift.

nature of the lens (in case of no aberrations). To find the deflection coordinate and the arrival angle of the electron at the screen, the easiest way is to apply ray transfer matrix analysis. In the case of a single thin lens (see Fig. 6.3), the expressions for the ray $(\xi,\, \alpha_x)^T$ and for the transfer matrix $\mathbf{M}$ are the following:

$$\mathbf{M}\begin{pmatrix} \xi \\ \alpha_x \end{pmatrix} = \begin{pmatrix} x \\ \alpha'_x \end{pmatrix}, \tag{6.6}$$

$$\mathbf{M} = \begin{pmatrix} 1 & L \\ 0 & 1 \end{pmatrix} \begin{pmatrix} 1 & 0 \\ -\dfrac{1}{F} & 1 \end{pmatrix} \begin{pmatrix} 1 & d \\ 0 & 1 \end{pmatrix}, \tag{6.7}$$

where F is the focal distance of the thin lens, d and L are distances from the deflection plane to the lens and from the lens to the screen, respectively; the vectors $(\xi,\, \alpha_x)^T$ and $(x,\, \alpha'_x)^T$ are coordinates and deflection angles of the electron ray in the sample plane and in the screen plane, respectively. The shift of the ray due to deflection can be written as:

$$\Delta x(\alpha_x) = M_{12}\,\alpha_x = \alpha_x dL\left(\frac{1}{F} - \frac{1}{L} - \frac{1}{d}\right), \tag{6.8}$$

The expression for the ray coordinates at the screen as a function of the deflection angles α_x and α_y is given by:

$$\begin{pmatrix} x(\alpha_x) \\ y(\alpha_y) \end{pmatrix} = \begin{pmatrix} x(\xi) + \Delta x(\alpha_x) \\ y(\eta) + \Delta y(\alpha_y) \end{pmatrix} = \begin{pmatrix} x(\xi) + \alpha_x M_{12} \\ y(\eta) + \alpha_y M_{12} \end{pmatrix}, \tag{6.9}$$

where $\alpha_{x,y}$ is the deflection along the x- and y-axis, respectively, in the sample plane and $x = \xi\, M_{11}$ and $y = \eta\, M_{11}$ with $M_{11} = 1 - L/F$. We keep coordinates $x(\xi)$ and $y(\eta)$ in the expression for convenience, because we evaluate the data at the detector's screen. If the screen is coincident with the image plane, then the deflection shift Δx approaches zero. This property underlies the linear-field approach. The lens (or the set of lenses) must be detuned from the imaging condition to be able to detect the deflection, i.e., to have angular resolution. For the sake of simplicity and in accordance with the performed experiment (see Chapter 5), only the single lens case is analyzed further in more details.

The main advantages of the linear-field approach are a constant spatial resolution during the recording of the density evolution due to constant lens magnification and simplicity in image tracing (see Subsections 6.4.1 - 6.4.4). However, it is not possible to investigate samples with a nonlinear electromagnetic response to the excitation field, and the effort of field reconstruction increases dramatically if there is a constant magnetic field[2].

Lens parameters and resolution of linear-field approach

To find the focal distance of the lens, where both spatial and angular resolutions are satisfactory, it is important to know the instrumental resolution of the setup. The spatial resolution is determined by the lens magnification and, in our case, by the pixel size of the detector $\Delta x_{\text{detector}}$, which is assumed to be the smallest resolvable displacement:

$$R_{\text{spatial}} = \frac{\Delta x_{\text{detector}}}{|M_{11}|} = \frac{\Delta x_{\text{detector}}\, F}{L - F}. \qquad \text{(spatial resolution)} \tag{6.10}$$

The angular resolution of the detector in the single-lens geometry can be derived from equation (6.8):

$$R_{\text{angular}} = \frac{\Delta x_{\text{detector}}}{|M_{12}|} = \frac{\Delta x_{\text{detector}}}{|M_{11}\, d + L|}. \qquad \text{(angular resolution)} \tag{6.11}$$

---

[2] While the sample is not at imaging condition, the shadow image would be distorted by static magnetic fields in the sample and the bijective relation between ξ, η and $x(\xi), y(\eta)$ would be broken.

For single-lens and multiple-lens cases, $M_{12} \propto M_{11}$[3], meaning that the higher the value of M_{11}, the smaller the angle can be resolved. Both resolution curves are depicted in Fig. 6.4 as functions of the focal distance (see figure caption for the values of L, l, d and $\Delta x_{\text{detector}}$). However, there is another resolution limit that comes from the divergence angle α_{div}, which is an essential property of the electron beam (see Section 3.2). This angle imposes a lower limit on the angular resolution in the experiment:

$$R_{\text{angular}}^{\text{divergence}} = \alpha_{\text{div}}. \qquad \text{(minimal angular resolution)} \qquad (6.12)$$

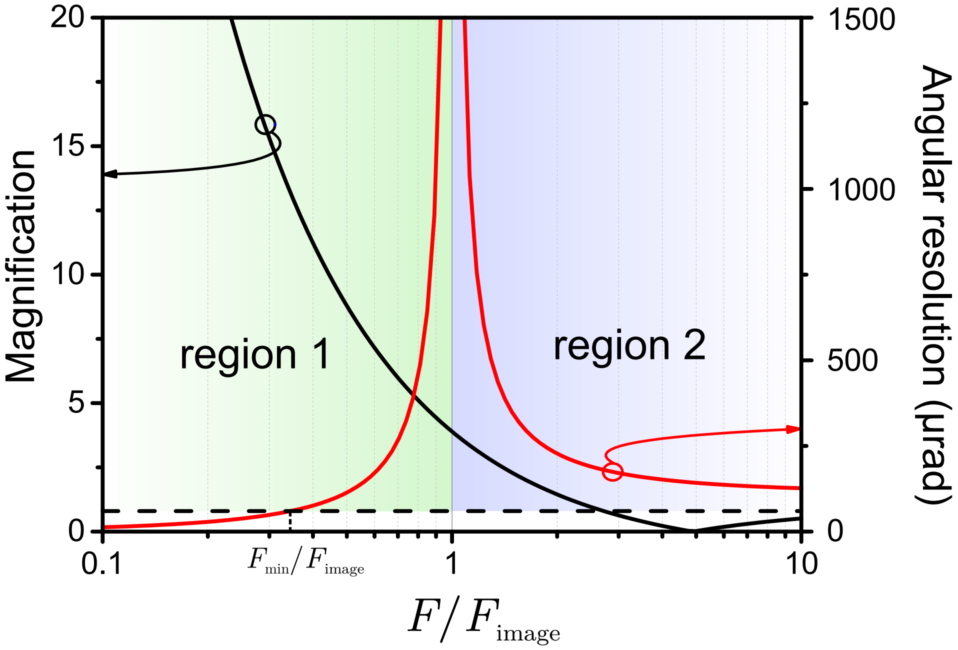

Figure 6.4: *Magnification and angular resolution as functions of focal distance.* The black solid line represents the magnification of the thin lens, i.e., element M_{11} of matrix $\mathbf{M}$ (see equation (6.7)). This value is plotted instead of R_{spatial} for better visualization. The red solid line represents the smallest angle that can be resolved with a certain F/F_{image} ratio with a camera of a pixel size Δx, i.e., R_{angular}. The black dashed line shows the divergence angle α_{div}, i.e., $R_{\text{angular}}^{\text{divergence}}$. The parameters used are: $L = 109\,\text{cm}$, $d = 28\,\text{cm}$, $\alpha_{\text{div}} = 60\,\mu\text{rad}$, $\Delta x_{\text{detector}} = 15.6\,\mu\text{m}$; $F_{\text{image}} = d\,L/(L+d)$ is the focal distance for the imaging condition of the lens. F_{min} is the focal distance of the lens at the lower limit of angular resolution.

The divergence angle $\alpha_{\text{div}} \approx 60\,\mu\text{rad}$ corresponds to a minimum-resolved field value of $E_{\text{min}}^{\text{eff}} = 2.4{\times}10^5$ V/m (see expression (2.18)). In Fig. 6.4, it is shown that in “region 2” the minimal resolved angle is higher than divergence angle α_{div} and the magnification is lower than in “region 1”, where the magnification is limited by the divergence angle, i.e., the minimal focal distance can be set to F_{min}. In our experiment, we stay in “region 1” in order to have higher magnification, however, for a proof-of-principle experiment, we work

---

[3] This can be proven by simple matrix multiplication. For a single thin lens, $M_{12} = d\,M_{11} + L$.

with magnification of about five times[4] to be on a safe side and away from the limit of angular resolution. For the single-thin-lens case, the minimum focal distance F_{min}, at which the angular resolution reaches the limit imposed by the beam divergence, can be derived from expression (6.11):

$$F_{\text{min}} = \frac{F_{\text{image}}}{\dfrac{\Delta x_{\text{detector}}}{\alpha_{\text{div}}\,(L+d)} + 1}, \tag{6.13}$$

where $F_{\text{image}} = \dfrac{L\,d}{L+d}$.

In [31], a related analysis was applied to the case of a state-of-the-art instrument, yielding a spatial resolution below 10 nm and an angular resolution below 20 µrad. This is sufficient for the typical fields in transistors or plasmonics. For a more appropriate analysis, more complex models for magnetic lenses can be applied [47, 79, 80].

6.3 Focus-variation approach

Another way to record a discrete evolution of the electron density is a focus-variation approach, which can be described by the following: instead of scanning the deflection strength (i.e., the excitation field amplitude), we vary the focal distance of the lens placed after the sample at a constant excitation strength (see Fig. 6.5). At the imaging condition ($F = F_{\text{image}}$), the angular resolution $R_{\text{angular}} \to \infty$ (see Fig. 6.4), thus no deflection can be observed. If F is varied, then deflection starts to appear together with magnification ($F < F_{\text{image}}$, see "region 1" in Fig. 6.4) or demagnification ($F > F_{\text{image}}$, see "region 2" in Fig. 6.4), reaching a diffraction condition without any spatial information at $F = L$. The magnification case is much more interesting, because it provides higher spatial resolution compared to the demagnification case. The approach gives a possibility to track electron rays, their convergence and divergence.

Let us again employ a ray optics analysis and derive the equation for the deflection angles. At the defocusing condition, i.e., when the image plane lies between the focus and the screen, the coordinate x of the ray at the screen is determined by the ray coordinate x_{image} at the image plane:

$$x = \xi\, M_{11}(F) = x_{\text{image}} \frac{M_{11}(F)}{M_{11}(F_{\text{image}})}. \tag{6.14}$$

The coordinates in the screen plane at the imaging condition x_{image} and y_{image} are related to ξ and η via element $M_{11}(F_{\text{image}})$ of matrix $\mathbf{M}$ (see equation (6.7)). An expression for the position shift Δx reproduces equation (6.8). In the experiment, we use magnetic coils for imaging and magnification. Taking into account that magnetic coils also cause a rotation of the image, the final expressions for the ray coordinates at the camera screen are:

---

[4] In Subsection 7.2, the magnification is about seven times.

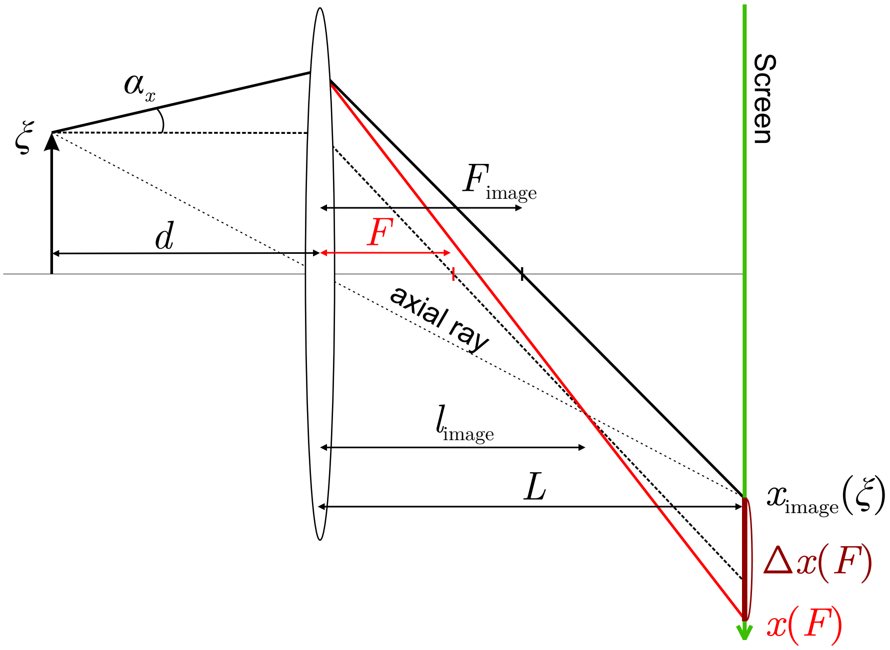

Figure 6.5: *Schematic of focus-variation approach.* The solid black line shows the deflected ray at the imaging condition ($F = F_{\text{image}}$), the solid red line shows the deflected beam at the condition $F < F_{\text{image}}$. By varying the focal distance of the lens, the electron density evolution can be recorded by a camera: starting from an undeflected image (the imaging condition) and proceeding with images that are more distorted by the deflection.

$$\begin{pmatrix} x(F) \\ y(F) \end{pmatrix} = R(\theta) \begin{pmatrix} x_{\text{image}} \dfrac{M_{11}(F)}{M_{11}(F_{\text{image}})} + \alpha_x M_{12}(F) \\ y_{\text{image}} \dfrac{M_{11}(F)}{M_{11}(F_{\text{image}})} + \alpha_y M_{12}(F) \end{pmatrix}, \tag{6.15}$$

$$\text{where } R(\theta) = \begin{pmatrix} \cos\theta & \mp\sin\theta \\ \pm\sin\theta & \cos\theta \end{pmatrix} \text{ is a rotation matrix.}$$

The rotation angle θ and the focal distance F of the lens are well described by the dependence of the magnetic lenses on the current I: $\theta \propto I$ and $F \propto I^{-2}$ [81].

Despite more complicated math relations between (ξ, η) and $(x(F), y(F))$ than before and additional memory requirements for calculations (see Section 6.4), the focus-variation approach is feasible on modern desktop computers and noticeably can reveal static magnetic fields and also the nonlinear response of the sample to the excitation, in contrast to the linear-field approach.

In this work's experiments, all available samples had negligible magnetic response on the excitation. For the sample with a magnetic response, the focus-variation approach is much more preferable. The deflection by static magnetic fields can be described also by an effective potential $\phi^0_{\text{eff}} = -v_e\,\mathcal{A}_z(x,y)$, where $\mathcal{A}_z(x,y)$ is a component of the magnetic vector potential $\boldsymbol{A}(x,y)$ and the magnetic fields can be obtained from $\mathbf{B} = \nabla \times \boldsymbol{A}$. In a further analysis, this has to be considered.

Lens parameters and resolution of focus-variation approach

In principle, the resolution analysis of the linear-field approach shown in Subsection 6.2 can be also applied to the focus-variation approach. "Region 1" (see Fig. 6.4) is then extended to $F/F_{\text{image}} = 1$, the imaging condition. By varying the focal distance from F_{image} towards the limit of F_{min}, the angular resolution increases, however, the spatial resolution is limited to the resolution at the imaging condition when $F = F_{\text{image}}$. In the end, the type of dynamics expected in the sample determines the most appropriate approach.

6.4 Inversion analysis by support points fit

Recording the discrete evolution of electron density by either the linear-field or focus-variation approach (see Sections 6.2 and 6.3), in principle, removes the ambiguity of the non-bijective problem (see Section 6.1), but the final solution has still to be found. By applying the model of ray tracing discussed above, it is possible to recover the field distribution $\mathbf{E}^{\text{eff}}(\xi,\eta)$ (i.e., the deflection angle distribution $\mathbf{A}(\xi,\eta) = (A_x(\xi,\eta), A_y(\xi,\eta))$ in the sample by a fitting procedure discussed below. Let us rewrite equations (6.9) and (6.15) as functions of the values we vary in the experiment – the electromagnetic amplitude E in the case of the linear-field approach and the focal distance F in the case of the focus-variation approach. In the case of the linear-field approach we can write expressions (2.18), (6.2) and (6.9) as:

$$\begin{pmatrix} x(E) \\ y(E) \end{pmatrix} = \begin{pmatrix} x(\xi) + A_x(E)M_{12} \\ y(\eta) + A_y(E)M_{12} \end{pmatrix} = \begin{pmatrix} x(\xi) + A_x(\xi,\eta)\, z^{\text{LFA}}(E) \\ y(\eta) + A_y(\xi,\eta)\, z^{\text{LFA}}(E) \end{pmatrix}; \tag{6.16}$$

Expression (6.16) is a "kinematic form" of the electron ray coordinate on the screen in the linear-field approach; $z^{\text{LFA}}(E) = E/E_{\text{max}}\, M_{12} = E/E_{\text{max}}\,(d\,M_{11} + L)$ is an effective screen position within the linear-field approach. E_{max} is the maximum amplitude that can be set in the experiment still satisfying the linear relation between the excitation and the dynamics in the sample (see Section 6.2). The coordinates $x(\xi)$ and $y(\eta)$ are the ray coordinates at the screen when $E = 0$, and we keep them in the equations, because the analysis is performed on images in the detector's screen plane. The components $A_{x,y}(\xi,\eta)$ of the deflection angle vectorial map are independent on the incident field amplitude E and the effective screen distance z^{LFA}.

The following expression (6.17) shows such kinematic equations for the focus-variation approach:

$$\begin{aligned}\begin{pmatrix} x(F) \\ y(F) \end{pmatrix} &= R(\theta(F)) \begin{pmatrix} x_{\mathrm{image}}(\xi)\dfrac{M_{11}(F)}{M_{11}(F_{\mathrm{image}})} + A_x(\xi,\eta)\, M_{12}(F) \\ y_{\mathrm{image}}(\eta)\dfrac{M_{11}(F)}{M_{11}(F_{\mathrm{image}})} + A_y(\xi,\eta)\, M_{12}(F) \end{pmatrix} = \\ &= R(\theta(F)) \begin{pmatrix} -\dfrac{x_{\mathrm{image}}(\xi)L}{M_{11}(F_{\mathrm{image}})d} + \left(A_x(\xi,\eta) + \dfrac{x_{\mathrm{image}}}{M_{11}(F_{\mathrm{image}})\, d} \right) M_{12} \\ -\dfrac{y_{\mathrm{image}}(\eta)L}{M_{11}(F_{\mathrm{image}})d} + \left(A_y(\xi,\eta) + \dfrac{y_{\mathrm{image}}}{M_{11}(F_{\mathrm{image}})\, d} \right) M_{12} \end{pmatrix} = \\ &= R(\theta(F)) \begin{pmatrix} \widetilde{x}_{\mathrm{image}}(\xi) + \widetilde{A}_x(\xi,\eta) z^{\mathrm{FVA}}(F) \\ \widetilde{y}_{\mathrm{image}}(\eta) + \widetilde{A}_y(\xi,\eta) z^{\mathrm{FVA}}(F) \end{pmatrix}, \end{aligned} \tag{6.17}$$

where $\widetilde{A}_r(\xi,\eta) = A_r(\xi,\eta) + \frac{r_{\mathrm{image}}}{M_{11}(F_{\mathrm{image}})\, d}$ for $r = x, y$, $M_{12} = d\, M_{11} + L$ and $z^{\mathrm{FVA}}(F) = M_{12}(F)$ is an effective screen position within the focus-variation approach. The modified angular distribution $\widetilde{A}_r(\xi,\eta)$ is independent on the focal distance F. Note that in order to have equidistant effective screen position steps, it is required to solve the equation $z^{\mathrm{FVA}}(F)$ for appropriate F values. Both $z^{\mathrm{LFA}}(E)$ and $z^{\mathrm{FVA}}(F)$ can be considered as steps of a discrete evolution of electron density with respect to the chosen approach. Examples of electron density evolution are shown in Fig. 7.2A and 7.8B.

In the experiment, we now obtain a data set that contains T pump-probe delay points at times τ; K images for each time step represent a batch of the discrete evolution of electron density. A single image can be indexed with I_τ^k. The image I_τ^0 is a *zero-image*, which is the same for all T batches: it is an image after passing the sample with no excitation (linear-field approach) or in the imaging condition (focus-variation approach). The index k increases while the excitation field amplitude or the lens strength rises; we denote the evolution step between I_τ^{k-1} and I_τ^k with z_k. Note that these increments do not have to be equidistant: the effective screen position can be varied linearly or according to some function. Images in the batch have to be taken within a range where the divergence of the incident electron beam does not play a significant role for resolution (see “region 1”, Fig. 6.4). All image counts are normalized to the counts of the zero-image to account for potential losses or varying sensitivity of the detector. Another important point is that images I_τ^0 and I_τ^1 should have only a small deviation, in particular the image area should remain roughly the same, see Subsection 6.4.1.

We discuss the two approaches in parallel, because the only difference is the propagation function based on equations (6.16) and (6.17). The following inversion procedure has four steps: three guessing steps and one global fit step. It is very important to note that this procedure is applied to every τ point (a pump-probe delay) independently, without any assumption on the field structure or the field dependencies between adjacent delay steps.

For visualization of the inversion procedure, we employ the results acquired with a split-ring resonator sample and linearly polarized THz radiation at the particular pump-probe delay $\tau = 3.1\,\mathrm{ps}$ (see Fig. 7.1) using the linear-field approach. The number of images in the evolution batch is $K = 17$ (including the zero-image). The results are depicted in Fig. 6.7, which is taken from [31].

6.4.1 Step 1

If images I_τ^0 and I_τ^1 are acquired in such a way that deflections are very small and the areas on the screen approximately remain the same, we can assume that overlaps between different rays are minimal and irrelevant. Another assumption for this step is a conservative effective two-dimensional deflection. It means that any field vortices are of smaller orders than the field, expressed by the gradient of an electric two-dimensional potential. From equation (6.4) for the particle density evolution, the Jacobian can be written (with $z = v_z\,t$):

$$\left|\frac{D(x,y)}{D(\xi,\eta)}\right| = \begin{vmatrix} \frac{\partial x}{\partial \xi} & \frac{\partial x}{\partial \eta} \\ \frac{\partial y}{\partial \xi} & \frac{\partial y}{\partial \eta} \end{vmatrix} = \begin{vmatrix} 1 + \frac{\partial V_x(\xi,\eta)}{\xi} t & \frac{\partial V_y(\xi,\eta)}{\partial \eta} t \\ \frac{\partial V_x(\xi,\eta)}{\partial \xi} t & 1 + \frac{\partial V_y}{\partial \eta} t \end{vmatrix} \overset{t\to 0}{\approx} 1 + \frac{\partial V_x}{\partial \xi} t + \frac{\partial V_y}{\partial \eta} t = 1 - \Delta\Phi(\xi,\eta) z, \tag{6.18}$$

where $\Delta = \nabla \cdot \nabla$ is the Laplace operator and $\Phi(\xi,\eta)$ is the effective two-dimensional scalar potential of the field inside the sample: $\mathbf{E}^{\mathrm{eff}}(\xi,\eta) \propto \mathbf{A}(\xi,\eta) = -\nabla\Phi(\xi,\eta)$. This effective potential is proportional to the electric potential (see equation (2.18)) averaged along the electron propagation near the sample. The discrete evolution of the electron density K lies within the time delay step τ, so the zeroth and first images are I_τ^0 and I_τ^1, respectively. The effective potential can be found by solving the Poisson equation:

$$\Delta\Phi_\tau^1(x,y) = \frac{\mathrm{I}_\tau^1(x,y) - \mathrm{I}_\tau^0(x,y)}{\mathrm{I}_\tau^0(x,y)\, z_1}, \tag{6.19}$$

where z_1 is the evolution step between $\mathrm{I}_\tau^0(x,y)$ and $\mathrm{I}_\tau^1(x,y)$ within the batch $\mathrm{I}_\tau^k(x,y)$ (z^{LFA} or z^{FVA} are applied depending on the evolution scan approach). In equation (6.19), we use the approximation $\mathrm{I}_\tau^0 \approx \mathrm{I}_\tau^1$ in the denominator[5]. For the linear-field approach, the procedure above is directly sufficient to perform "step 1" and find $\Phi_\tau^1(\xi,\eta)$. For the focus-variation approach, it is required to trace the zero-image pixels with the magnification propagator and rotation matrix, i.e., using the tracing function with the limit $M_{12}(F) \approx 0$ (see equation (6.15)) and, after the Poisson equation is solved, the effective potential can be found as well.

In order to assess the quality of the solution, we compare the experimental and simulated images. The latter are obtained via calculation by using a propagating function via calculation. Obtaining the propagating or tracing function is straightforward. For both the linear-field and focus-variation approach, each signal pixel of the zero-image has a value $\mathrm{I}_\tau^0(x,y)$ and angles $A_x(x,y)$, $A_y(x,y)$. The pixel values are traced to a new position according to equations (6.16) and (6.17) and the signal is split between four neighboring pixels

---

[5] This approximation is not necessary but usually the zero-image I_τ^0 is acquired in a way to reduce image-to-image noise by longer exposure time and, thus, has less probability to contain single-image artifacts.

proportionally (within a 2×2 pixel block). Fig. 6.6 schematically illustrates the tracing of the signal. It is possible to artificially increase the resolution by introducing a sub-grid at every pixel for the potential/field value while applying the tracing function, but then the splitting procedure should be done among greater number of pixels.

The point-spread function of the detection camera ($\sigma_{PSF} = 0.8\,\text{pixel}$ [82]) and the divergence of the electron beam (each point at the sample can cover more than one pixel on the detector) have to be considered. For the linear-field approach, the image has already a blur because of the slight defocusing. The blur width as a function of the divergence angle of the electron beam $\sigma_{\text{div}} = 0.5\,\Delta x(\alpha_{\text{div}})$ can be estimated from expression (6.8) and amounts to less than one pixel in our experiment, so as the first approximation we can directly trace pixels. For the sub-grid case, however, it is required to use a Gaussian function with a standard deviation of σ_{div} to apply the correct weight to each ray on the detector. For the focus-variation approach, σ_{div} is increasing within the electron density evolution and can reach values greater than the pixel size. Therefore, at every image simulation, pixel-splitting procedure needs weighting for surrounding pixels by a Gaussian distribution of width σ_{div}.

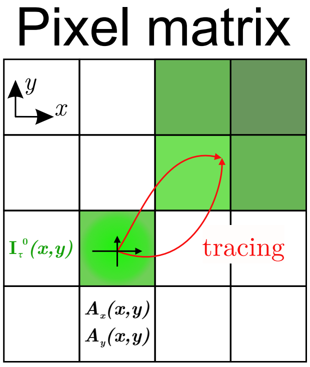

Figure 6.6: *Tracing function schematic.* A pixel value $\mathrm{I}_\tau^0(x,y)$ is proportionally split between 2×2 pixel block around the traced position, calculated using the deflection angles $A_x(x,y)$ and $A_y(x,y)$ and the kinematic expressions (6.16) and (6.17).

Fig. 6.7C shows the simulated electron density using the last evolution step z_{15}^{LFA}(i.e., the highest amplitude of the THz excitation pulse), based on the solution of the Poisson equation (see equation (6.19)). For comparison, the experimental electron density at the last evolution step is depicted in Fig. 6.7G.

6.4.2 Step 2

When the effective potential $\Phi_\tau^1(x,y)$ is found, we can vary its values at every (x,y) point in order to fit the simulated image to the entire batch of density evolution by minimizing the squared differences between experiment and computation according to a model for acquiring the evolution batch. Because the images contain a large number of signal pixels ($\gtrsim$ 4000 pixels), the problem is over-determined, but the procedure requires a lot of memory and computational resources. In order to increase the performance, we assign N support points over the relevant area, formed by the zero-image, also referred to the *zero-image mask* (see Fig. 6.7B). These points represent a grid with equidistant steps in the x- and y-directions[6] and act as spline points for the effective potential and, further, for the deflection angle distribution. The points do not entirely lie within the mask but also slightly outside (see Fig. 6.7B). In this way, by using a biharmonic spline interpolation algorithm, the effective potential and deflection angle values can be found for all points inside the zero-image mask area. The grid step and area beyond the zero-mask is a trade off between evaluation speed, spatial accuracy and artifacts that can appear, for example, due to noise.

After assigning N spline support points that describe the effective potential $\Phi^1_\tau(x,y)$, we compare pairs of several experimental and simulated images starting from less distorted images and leading to more distorted ones and solve the non-linear least squares problem using a Gauss-Newton algorithm[7], where the support points act as parameters being adjusted.

The convergence of the minimization problem is characterized by the mean square error χ^2. For functions with only one global minimum, initial parameter values are irrelevant, but with complicated non-bijective functions and a big number of parameters, the fitting procedure can reach a local minimum, which can be far away from the global minimum and thus does not yield the final solution. In order to avoid local minima, a good initial guess of the parameters must be chosen for the Gauss-Newton algorithm [83]. This guess is provided by "step 1". We cannot assess the convergence only by χ^2, but also need to consider the quality of image fitting, or, simpler, how well the simulated images reproduce the experimentally acquired images. Moreover, to proof the validity of the fitting approach, we can perform a numerical experiment with parameters close to the real one (see Chapter 5): tracing electrons through the excited sample, acquiring electron density images, evaluating the fields with our approach and comparing those with the fields in the numerical experiment (see Section 7.3). It turns out that a guess via "step 1" almost always yields proper results (see Section 7.3).

The parameter variation step in the Gauss-Newton method and the termination conditions are set such that the fitting converges after ∼15-20 iterations. The fitting is first performed only on a few first consecutive images of the evolution batch, where deflections are not yet very pronounced, relying on the potential approximation. The result of the first fit acts as an input for a next image pair and so on, until we reach a certain image, at which the potential-field approximation may not hold anymore. This ends "step 2" of the field evaluation.

As a result, we obtain N support points that approximately describe the pseudo-potential[8] $\Phi^2_\tau(x,y)$. This result has already reduced random (image-to-image) noise substantially and significantly improves the first guess of the angular distribution, based on the effective potential $\Phi^1_\tau(x,y)$. In the illustrated example, the fitting is performed on im-

---

[6] Equidistant steps are necessary for faster computation using a graphics processing unit (GPU).

[7] The Gauss-Newton algorithm was chosen instead of, e.g., the Levenberg-Marquardt or hybrid algorithms, because it is simpler to implement [83].

[8] The superscript "2" denotes to the step number, not the power.

ages with index numbers from 2 to 8. Fig. 6.7D depicts the simulated density, calculated according to the fitting result of the 5th image in the batch at the last evolution step z_{15}^{LFA}.

6.4.3 Step 3

At this step, N support points of "step 2" are split into 2N points that describe now two independent components of the deflection angle distributions $A_x(x, y)$ and $A_y(x, y)$. Field vortices are now allowed. The fit is again done on pairs of the experimental and simulated images (based on the zero-image), and now only the highest-amplitude images of the batch are involved. After the component separation, the fitted maps of the deflection angles first seem to become worse, but then they gradually converge to a better solution than before (see Fig. 6.7A, fit step 8). The result of this step is a new set of 2N spline points describing $A_x(x, y)$ and $A_y(x, y)$.

For the data shown here, we fitted the 6th, 7th, 9th, 12th, 14th, 16th image of the evolution batch. In Fig. 6.7E, the simulated electron density of the 9th image is shown at the last evolution step z_{15}^{LFA}.

6.4.4 Step 4

In the last step, the 2N resulting points from "step 3" are used as an initial guess, but the fit now involves the entire range of images in the evolution batch at once. Here, the deflection angle distributions (or field distributions) are not bound to a particular image but to the entire set, thus, the noise and artifacts of the pair-fitting are reduced, which improves the fit and yields the final result (the global fit).

As a result after "step 4", we obtain a pair of two-dimensional matrices[9] of size $M \times N$, where each element corresponds to a discrete spatial coordinate (x, y) and the values of each element within both matrices correspond to the deflection angles α_x and α_y, which can be converted into the electric field components E_x^{eff} and E_y^{eff} via equation (2.18), respectively.

Fig. 6.7F depicts the simulated electron density distribution, using the global fit result (on images 1 to 16) at the last evolution step (highest amplitude of the THz excitation pulse). In Fig. 6.7A the overall fit convergence is shown, where each point refers to performed fitting, discussed in Subsections 6.4.1-6.4.4.

It is important to note again that all evolution batches K, consisting of images I_{τ}^{k}, are fit automatically and without the need of supervision at each pump-probe delay τ independently from each other, applying no assumptions on the dynamics at the sample. The fact that the result is smooth in time also demonstrates the validity of guessing and fitting steps 1-4. After the inversion analysis of every delay step is complete, we can combine all the data in one complex 3D $M \times N \times T$ matrix $\mathbf{E}^{\mathrm{eff}} = \mathbf{E}_{\mathbf{x}}^{\mathrm{eff}} + i\mathbf{E}_{\mathbf{y}}^{\mathrm{eff}}$.

We have mentioned image-to-image noise, which has a non-correlated origin and can not be avoided. It is difficult to involve this noise in the resolution limit estimation, however, at

---

[9] The size of the evaluated deflection angle (or field) matrices can differ from the size of I_{τ}^{k} if the resolution is changed or the images in the batch are cropped to reduce memory usage.

decent signal-to-noise ratios, the noise is averaged during the calculations and the respective error is reduced.

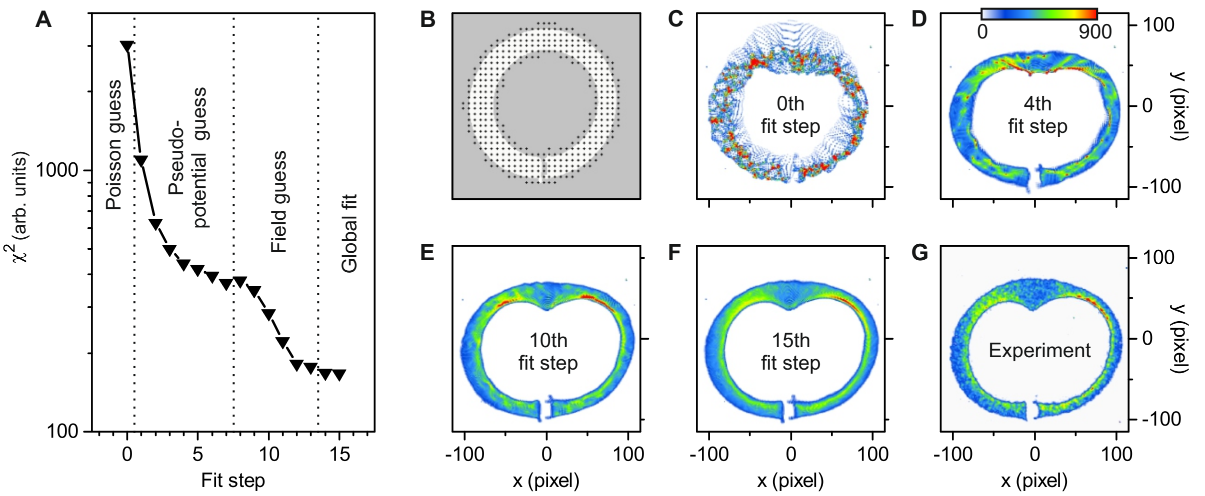

Figure 6.7: *Fit convergence and grid.* (A) Evolution of the mean square error χ^2 between simulated images and the data batch though the three stages of guessing and the final fit. The 14^{th} and 15^{th} fit steps show χ^2 after 15 and 31 iterations of the global fit, respectively. (B) Assignment of spline points on the split-ring zero-image mask. (C)-(F) Evolution of the fitted images at the last evolution step z^{LFA} through the guessing and fitting procedure. (G) Measured image at the last evolution step (the highest excitation field). The pump-probe delay of the evaluated evolution batch is $\tau = 3.1\,\mathrm{ps}$.

6.5 Singular value decomposition

After retrieving the time-dependent vectorial field distribution matrix $\mathbf{E}^{\mathrm{eff}}$, additional analyses can be applied. From the polarization dynamics at every spatial position, it is possible to evaluate values like damping coefficients, resonance frequencies and many more observables as desired. Further descriptive information can be provided by decomposition methods, with which eigenmodes of the sample's dynamics can be extracted. In the current work a *Singular Value Decomposition* (SVD)[10] [85,86] is used for this purpose. However, it is interesting to mention *Dynamic Mode Decomposition* (DMD) [87,88], which can be also applied for our problem. The latter technique can minimize uncorrelated mode structures, for which it is difficult to determine any physical significance, although, the requirements for the delay step size are more rigid. On the other hand, SVD requires neither equidistant nor small steps and, while the oscillations are well-pronounced, it can also extract the main modes.

---

[10] *Singular Value Decomposition* is a discrete version of *Proper Orthogonal Decomposition* (POD). Moreover, SVD is closely connected with *Eigenvalue Decomposition* (EVD), which can be computed only for symmetric matrices. However, squared singular values and eigenvalues for matrices $\mathbf{N}^*\mathbf{N}$ and $\mathbf{N}\mathbf{N}^*$ are the same, where $\mathbf{N}^*$ is conjugate transpose of $\mathbf{N}$ [84].

The SVD is the factorization of a complex matrix $\mathbf{N}$ (size $m \times n$, rank r), which has the form:

$$\mathbf{N} = \mathbf{U}\mathbf{\Sigma}\mathbf{V}^*, \tag{6.20}$$

where $\mathbf{U}$ is a unitary matrix (size $m \times m$), $\mathbf{\Sigma}$ is a diagonal matrix with non-negative real numbers (size $m \times n$) and $\mathbf{V}^*$ is a unitary matrix (size $n \times n$)[11].

To apply SVD to our space-time data, we need to reshape the 3D data matrix $\mathbf{E_{eff}}$ (size $M \times N \times T$) into a 2D matrix $\mathbf{E} = (\mathbf{E}_1, \mathbf{E}_2, ..., \mathbf{E}_L)$ (size $T \times L$, $L = M \times N$), where each column $\mathbf{E}_i$ represents a temporal evolution of the field at each spatial point (x, y) of $\mathbf{E_{eff}}$. If we decompose matrix $\mathbf{E}$ into $\mathbf{U}\mathbf{\Sigma}\mathbf{V}^*$, the physical meaning for the singular values σ_i of $\mathbf{\Sigma}$ is the energy amount stored in the i^{th} mode. Columns u_i of $\mathbf{U}$ are usually called "chronos" and describe the temporal evolution of the i^{th} mode, while columns v_i of $\mathbf{V}$ are called "topos" and describe the spatial configuration of the mode. The real and imaginary parts of the vector elements refer to the x- and y-component of the field, respectively. To improve calculation speed and reduce memory usage, thin SVD is applied[12]. Fig. 6.8 shows a schematic representation of thin SVD, depicting "chronos" and "topos".

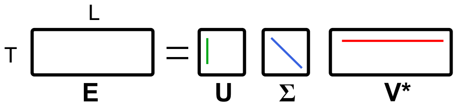

Figure 6.8: *Schematic diagram of thin SVD.* Matrix $\mathbf{E}$ (size $T \times L$) is decomposed into three matrices. Matrices $\mathbf{U}$ and $\mathbf{V}$ are unitary and $\mathbf{\Sigma}$ is a diagonal matrix. The green line in the matrix $\mathbf{U}$ depicts "chrono", a column vector u_i of $\mathbf{U}$, the blue line depicts a descending series of singular values of $\mathbf{\Sigma}$ and the red line stands for "topo", a column vector v_i of $\mathbf{V}$.

For a better visual presentation of the experimental data together with the evaluation results, SVD analyses are presented in Chapter 7. It is important to note that SVD neither enforces harmonic-oscillator solutions nor assumes any electromagnetic boundary conditions.

---

[11] Matrix $\mathbf{\Sigma}$ is unique for matrix $\mathbf{N}$. When modes are pronounced, as in our case, and singular values are distinct, matrices $\mathbf{U}$ and $\mathbf{V}$ are unique as well [89].

[12] National Instruments LabVIEW's built-in thin SVD algorithm is used, which automatically provides singular values in descending order on the matrix diagonal.

Chapter 7

Electron microscopy of electromagnetic waveforms: results

This chapter presents the main results of waveform microscopy, introduced in this work. The investigated samples are split-ring, bowtie and slit resonators, already discussed in Chapters 4 and 6. The split-ring resonator was excited by linear and circular polarization in two different experiments, for the bowtie and slit resonators only linear polarization was used for excitation. Moreover, we applied field reconstruction analysis (see Section 6.4) to simulated data (see Section 7.3) in order to confirm the validity of the iterative fitting approach. For the data obtained from the three different samples, we also applied singular value decomposition to reveal the spatial and temporal profiles of predominant modes.

Some sentences and figures are partially or completely taken from the original publication in Science, Vol.353, pages 374–377 [31]. I especially want to thank Dr. Peter Baum for helpful discussions and support with the article text and visualization.

7.1 Split-ring resonator: linear THz polarization

A microscope photo of the split-ring resonator is shown in Fig. 7.1C. The structure is laser-drilled through a 30-µm aluminum foil. The inner metal part is held only by a thin bridge and it lies slightly out of the foil's plane.

For the data acquisition (see Chapter 5), the time delay step was set to 100 fs, close to the pulse duration value. The dataset is four-dimensional and comprises 250×250 image pixels, 150 pump-probe delays and 16 different but equidistant excitation field strengths (electron density evolution). The maximum corresponding infrared pump power was 8.6 W going into the LN crystal (see "THz block 1", Fig. 3.1), hence producing a field of 2 V/µm at the sample's position. Fig. 7.1A and B show a part of the acquired raw data and the evaluated vector fields, respectively, at certain time delays. The triangle tips denote the vectorial direction, and field strength is encoded in color and size. Some high-frequency

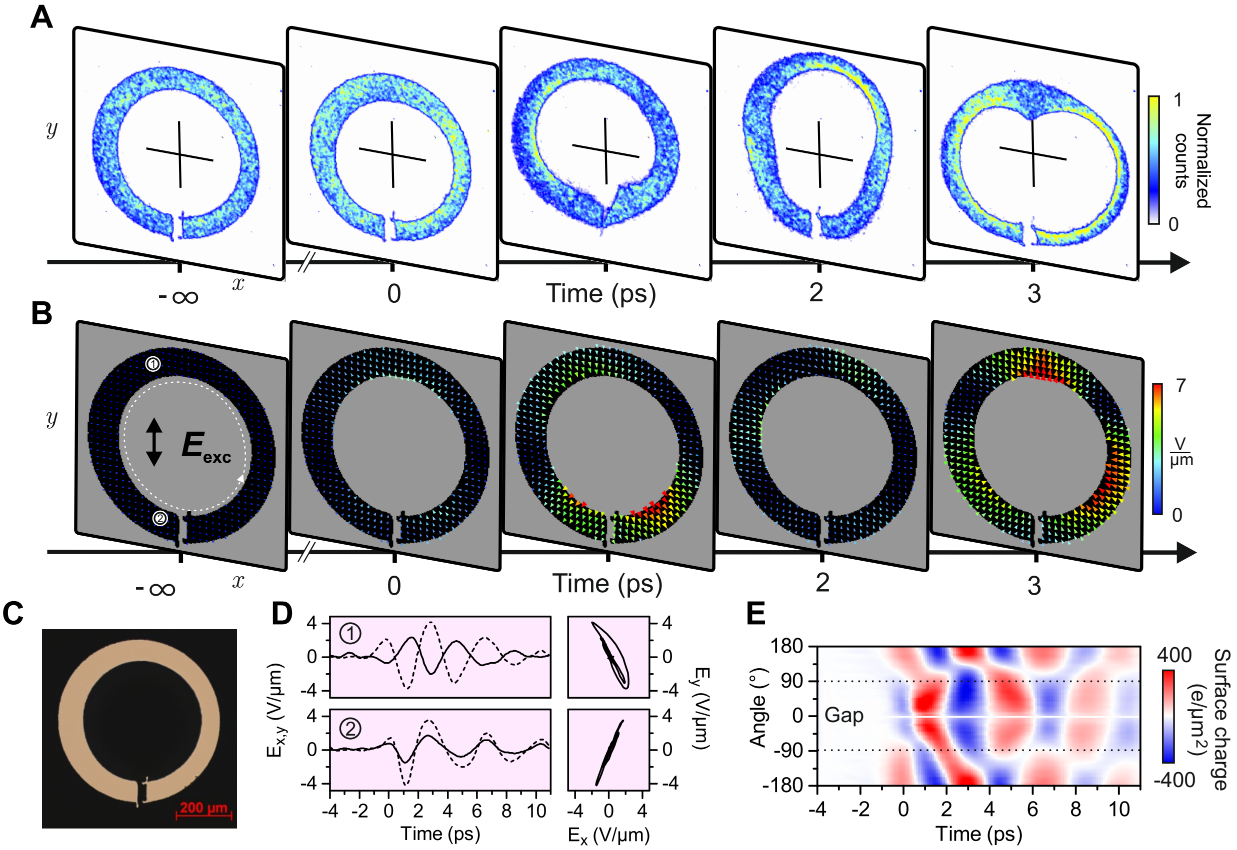

Figure 7.1: *Split-ring resonator under linear polarization: raw data and results.* (A) Image sequence of the raw electron density. (B) Reconstructed time-dependent vectorial fields. Triangles show the direction, the amplitude is encoded in color. (C) Microscopic photo of the split-ring sub-wavelength structure. (D) Time-dependent fields (left) and polarizations (right) at the locations ① and ② in (B) (solid and dashed lines refer to the x- and y-components, respectively). (E) Space-time map of the surface carrier density at the inner edge [(B), the white dashed line].

temporal noise was diminished with a low-pass Gaussian filter at 1 THz. The vector field at 3 ps shows three local maxima (top, right and left). We see an asymmetry in the x-direction, a predominantly radial polarization everywhere, and at each angle a radially decreasing field strength. The peak field is 7 V/µm, which is ∼3.5 times higher than the driving field. Fig. 7.1D shows the time-dependent electric fields and polarizations (right block) at two selected positions (white circles in the first delay image of Fig. 7.1B). Fitting each such time trace with a damped-harmonic oscillator model reveals a map of central frequencies (0.27 – 0.30 THz) and dampings (0.17 – 0.33 THz). These ranges indicate that one delocalized mode is predominant after the excitation. The singular value decomposition results confirm the predominant mode, and Fig. 7.2B and C depict the spatial and temporal configuration of the mode, respectively.

Fig. 7.1E shows an analysis of the collective carrier motion causing the observed near-field dynamics. The surface charge density $\sigma = \epsilon_0 E_\perp$ is plotted along a path around the inner edge of the resonator (see the first plot in Fig. 7.2B), where ϵ_0 is a vacuum permittivity and $E_\perp$ is a field component perpendicular to the inner surface. The peak charge density is $\sim$400 e/µm^2, and $\sim$20 e/µm^2 are detectable above the noise. Three spatial regions are evident, one at the top ($\pm180°$) and two others left and right of the gap ($\sim\pm45°$). The dynamics around the gap extends by more than $\pm90°$ and is phase-shifted with respect to the top region. Some features in Fig. 7.1E have a tilt, indicating in part an azimuthally traveling excitation, which is also observable in the raw data. Circular motion ceases after $\sim$4 ps and the remaining dynamics is mostly symmetric with respect to the x-axis. It appears that the excitation first localizes at the gap and the top half, while subsequently creating a spread-out, rather symmetric and longer-lived mode with mostly radial polarization.

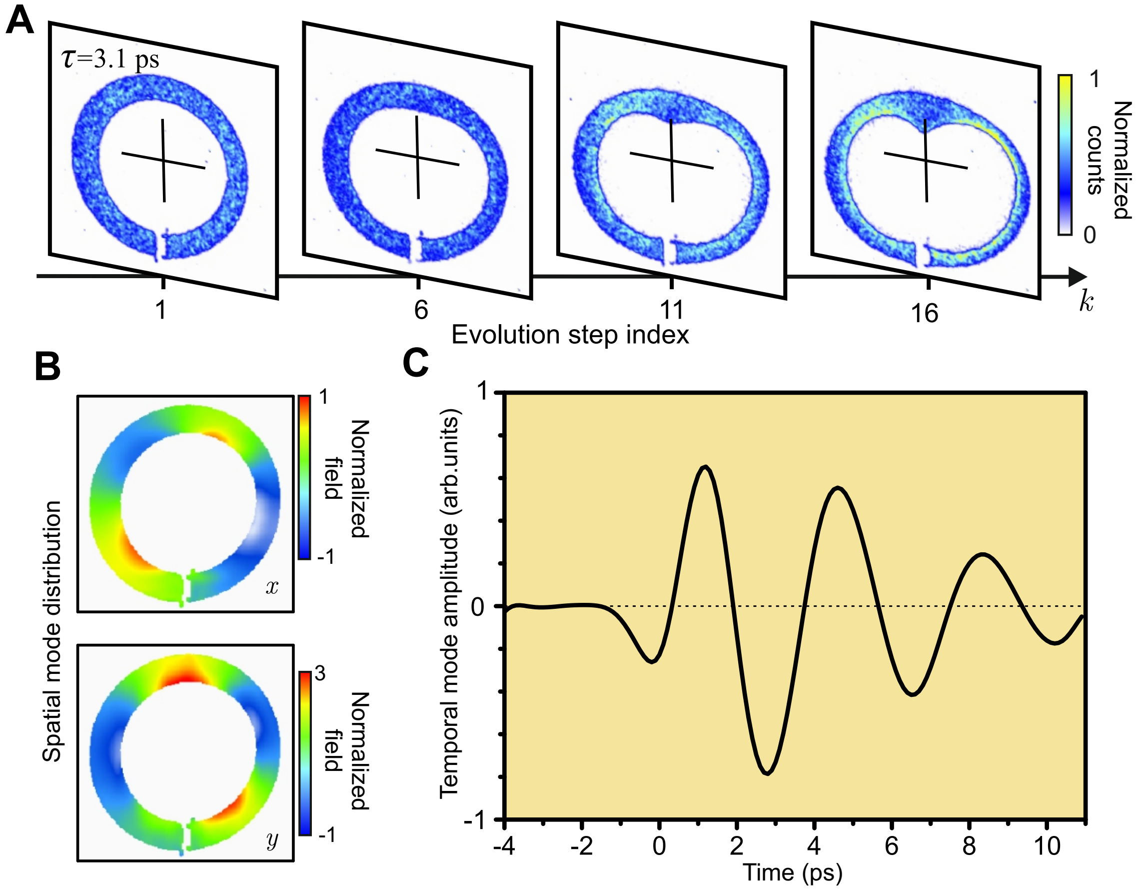

Figure 7.2: *Split-ring resonator under linear polarization: electron density evolution and eigenmode.* (A) Discrete evolution of the electron density at time delay $\tau = 3.1$ ps. (B) Spatial distribution of the predominant eigenmode in the split-ring resonator under the linear THz excitation (E_x^{eff} at the top and E_y^{eff} at the bottom). (C) Temporal profile of the predominant eigenmode in the split-ring resonator under the linear THz excitation.

7.2 Split-ring resonator: circular THz polarization

Circular polarization is created by inserting a wave plate in the THz excitation beam, consisting of three quartz plates cut at different crystal axis orientations and stacked together [90], designed and produced by Bernhard Halle Nachfl. GmbH.

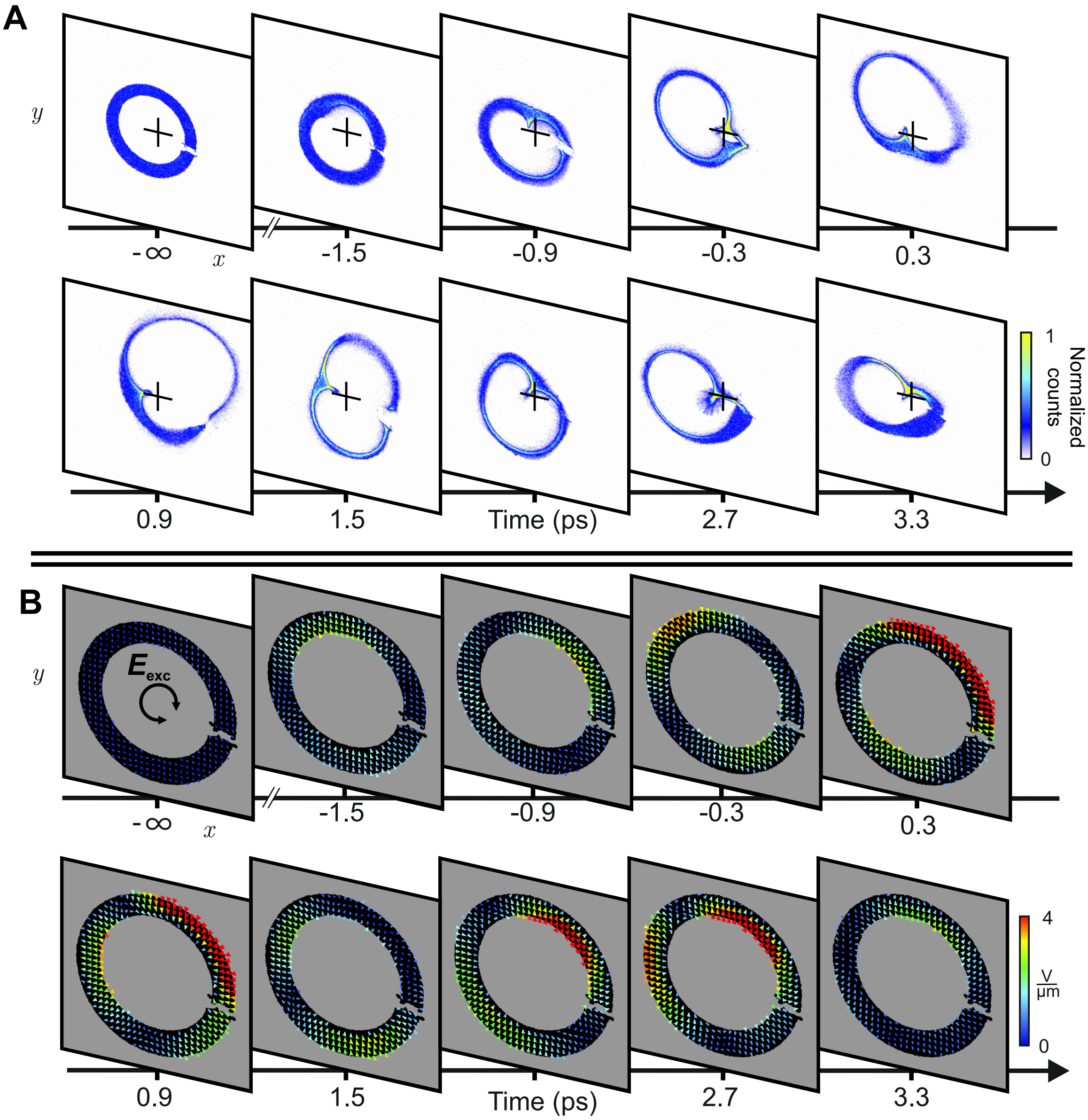

Figure 7.3: *Split-ring resonator under circular polarization: raw data and results.* (A) Image sequence of the raw electron density. (B) Field-guess evaluation ("step 3", see Section 6.4) of time-dependent vectorial fields.

The imaging lens magnification (see Fig. 5.1) was set to 7×, slightly higher than considered in Section 7.1, in order to increase the angular resolution due to losses at the wave plate. Due to hardware memory limitation of the computational resource, “step 4” of the reconstruction (see Section 6.4) was not performed, and the results of “step 3” are plotted[1] instead in Fig. 7.3B. In contrast to the linear polarization case, where only one predominant mode was excited and the electron density changes occurred more or less symmetrically to the axis (passing through the ring’s center from left to right), here we can observe a pronounced circular dynamics. A knot feature in the electron density (see cross position at $\tau = -0.3\,\text{ps}$ in Fig. 7.3A), created by a diverging field in the split-ring, exhibits a circular, clockwise movement.

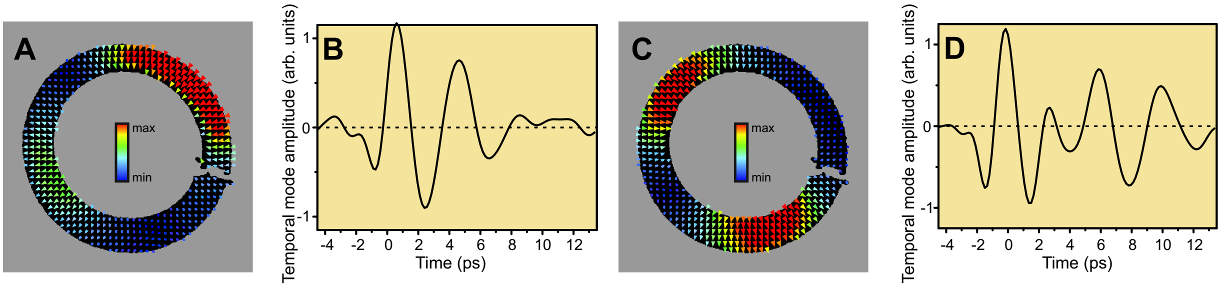

Figure 7.4: *Split-ring resonator under circular polarization: SVD results.* (A) Spatial amplitude profile of the first predominant mode. (B) Time-dependent profile of the mode (A). (C) Spatial amplitude profile of the second predominant mode. (D) Time-dependent profile of the mode (C).

Fig. 7.4A and C show the spatial amplitude profiles of two predominant modes and Fig. 7.4B and D depict their temporal dynamics, obtained by singular value decomposition.

---

[1] The result of the “step 3” is close to the final solution but not entirely equivalent.

7.3 Split-ring resonator: numerical validation

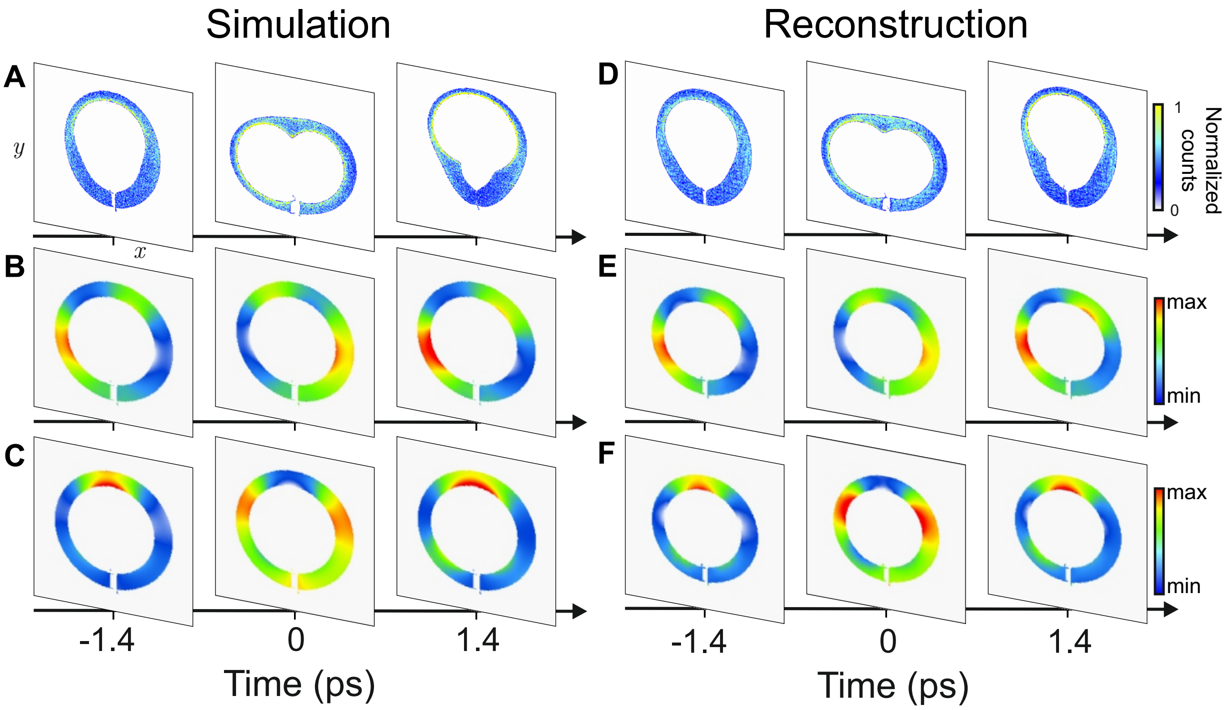

Figure 7.5: *Split-ring resonator under linear polarization: numerical validation.* (A) Image sequence of the electron density, obtained by the numerical simulation. (B) Longitudinally averaged ($z = -48 \ldots 48$ µm) x-component of the time-frozen Lorentz force. (C) Longitudinally averaged ($z = -48 \ldots 48$ µm) y-component of the time-frozen Lorentz force. (D) Reconstructed electron density image sequence. (E) Reconstructed time-dependent x-component of the field. (F) Reconstructed time-dependent y-component of the field. The color scale of respective simulated and evaluated plots is proportional.

The numerical experiment is realized with CST software (CST Particle-In-Cell Solver, CST GmbH) and reproduces the experiment well for the split-ring sub-wavelength resonator (see Section 7.1). A two-dimensional electron distribution is numerically propagated without particle-particle interactions and transversal velocities through the split-ring resonator with a longitudinal velocity of $v_e = 0.485c$. The number of simulated electrons is 5×10^5, in order to produce sufficient image signal. The resonator's model is based on the microscopic photo (see Fig. 7.1C) and includes similar imperfections. The material of the resonator is a perfect electric conductor, which is a good approximation at the THz frequencies in the experiment. The excitation is done by a plane wave with a Gaussian temporal envelope in the frequency range of 0.1 – 0.8 THz (see Fig. 3.2 for comparison). The initial position of the electron pulse is constant for different simulation iterations and the plane wave's initial position is shifted in the z-direction by 200-fs steps in order to scan the delay time. The electrons' positions and velocities are probed at $z = 392.5\,\mu\text{m}$ after the sample. Here, the interactions with the fields have subsided and the electrons are propagated using the ray matrix approach through a thin lens towards the screen. The distances d, L and the focal length F (see Section 6.2) were set as in the experiment. Obtained images were analyzed for the field reconstruction with exactly the same algorithm as in the experiment. The three-dimensional Lorentz force[2] was extracted at time delay τ_0, when electrons pass the center of the sample, and then longitudinally integrated within the range $z = -48 \ldots 48$ µm.

Fig. 7.5A and D show the simulated and reconstructed electron density images, respectively. Fig. 7.5B and C depict the transversal x- and y-components, respectively, of the longitudinally integrated time-frozen Lorentz force between $z = -48 \ldots 48$ µm. Fig. 7.5E and 7.5F present the reconstructed x- and y-components of the effective field $\mathbf{E}^{\mathrm{eff}}$, respectively.

---

[2] The Lorentz force $\mathbf{F}^{\mathrm{Lorentz}}(x, y, z; \tau_0)$ was calculated from three-dimensional electric and magnetic field distributions via $\mathbf{F}^{\mathrm{Lorentz}}(x, y, z; \tau_0) = e(\mathbf{E}(x, y, z; \tau_0) + v_{\mathrm{e}}\, \mathbf{B}(x, y, z; \tau_0))$.

7.4 Bowtie resonator

In the next experiment, we apply the waveform microscopy technique to a bowtie structure, already discussed in Subsection 4.2.3. Fig. 7.6A depicts a time delay sequence of the experimental raw images at the highest deflection field amplitude, and Fig. 7.6B shows the reconstructed vectorial fields. In the bowtie structure, there is only one mode excited (frequency 0.3 THz, damping ∼0.2 THz) and the evaluated time-dependent field in the center is presented in Fig. 7.6C along the enhancement direction, which reproduces the evaluated field from Subsection 4.2.3 (see Fig. 4.8). The field enhancement at $\tau = 2.8\,\text{ps}$ is ∼9 close to the metal and ∼6 at the center, which is lower than desirable, because the rounded crests of our structure apparently disperse the field lines at the center. Fig. 7.6D depicts the amplitude of the predominant mode from the SVD.

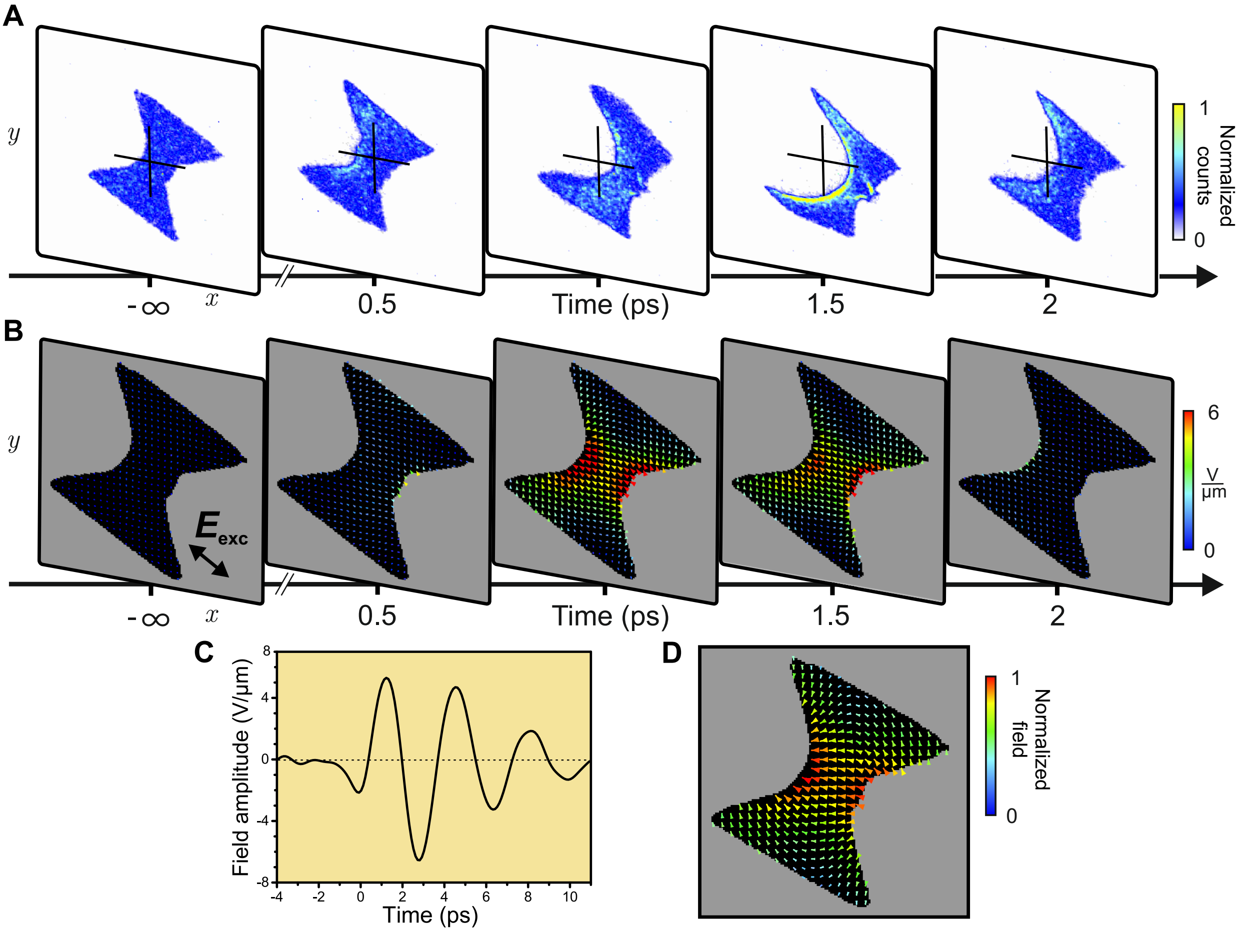

Figure 7.6: *Bowtie resonator: data and results.* (A) Image sequence of the raw electron density. (B) Reconstructed time-dependent vectorial field. (C) Evaluated time-dependent field at the center of the bowtie structure. (D) Spatial profile of the predominant mode, revealed through singular value decomposition of the evaluated data.

7.5 Slit resonator

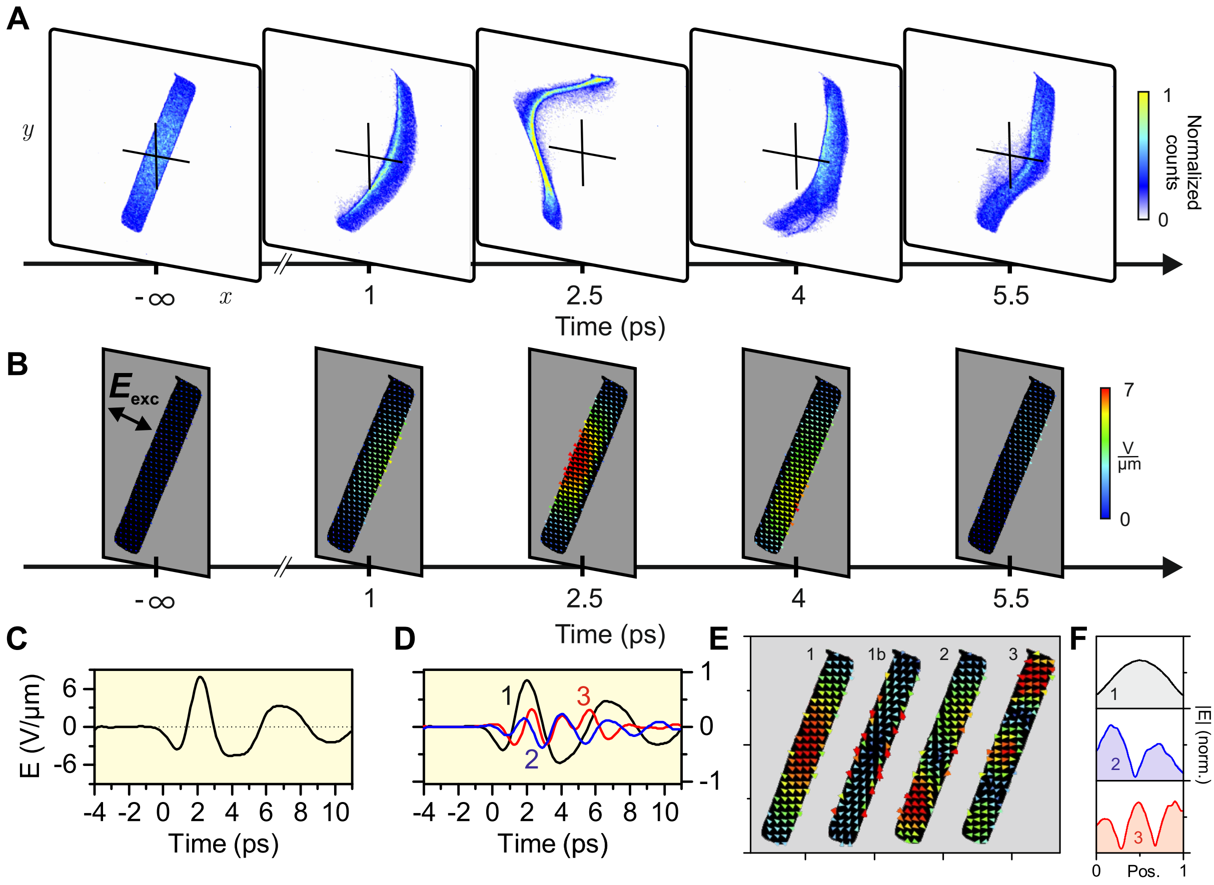

Figure 7.7: *Multi-mode slit resonator: data and results.* (A) Image sequence of the raw electron density. (B) Reconstructed time-dependent vectorial fields. (C) Evaluated time-dependent field at the center of the slit structure. (D) Time traces (amplitudes, scaled) of modes 1, 2, and 3 in (E). (E) First four predominant modes revealed through singular value decomposition. (F) Electric field strengths along a line through the center for modes 1, 2 and 3 in (E).

Next, we use the waveform electron microscopy to characterize a rectangular aperture resonator, discussed in Subsection 4.2.2. Fig. 7.7A shows raw images at the highest deflection field and Fig. 7.7B presents the reconstructed time-dependent vectorial fields. Fig. 7.7C shows the reconstructed field at the center, which reproduces the deflection field, evaluated in Subsection 4.2.2 (see Fig. 4.7A). The frequency at early times is higher than later, where the oscillations show a non-harmonic shape with damped peak regions. This indicates the presence of multiple modes at different frequencies, but phase-locked. In order to find those, we again invoked a principle component analysis via singular value decomposition. Fig. 7.7E depicts the first four predominant modes; further ones have no clear shape or time structure anymore. Three of the modes have a series of maxima that are almost equidistantly distributed over the slit length. Mode 1b is different and has a shape with vortex polarization; we attribute this to residual magnetic field effects and a slight tilt of the structure with respect to the electron beam. Also, the electron pulse duration was slightly longer than expected, which created additional noise. Fig. 7.7D shows the time traces from the decomposition matrix. Mode 1 is centered at 0.20 THz, mode 2 at 0.39 THz and mode 3 at 0.54 THz. Fig. 7.7F shows cuts through the modes along the slit's long axis at the center. One, two and three spatial maxima are evident, respectively, but with some asymmetries and slightly elliptical polarization in modes 2 and 3.

7.6 Focus-variation scan

In Section 6.3, we had discussed that for certain experimental situations involving nonlinearity, the linear-field approach of recording the discrete evolution of electron density has to be replaced by the focus-variation approach. Although the evaluation has not been preformed due to computational limitations, we present here the time delay sequence of raw images at the highest lens strength (magnification 9×) in the focus-variation scan. The angular resolution is increased as compared to before and it is clearly shown that low-amplitude fields can be better resolved than it was possible in Section 7.4.

This ability of waveform electron microscopy is important, because it shows that almost any kind of sample with almost any order of response to the excitation field can be appropriately studied.

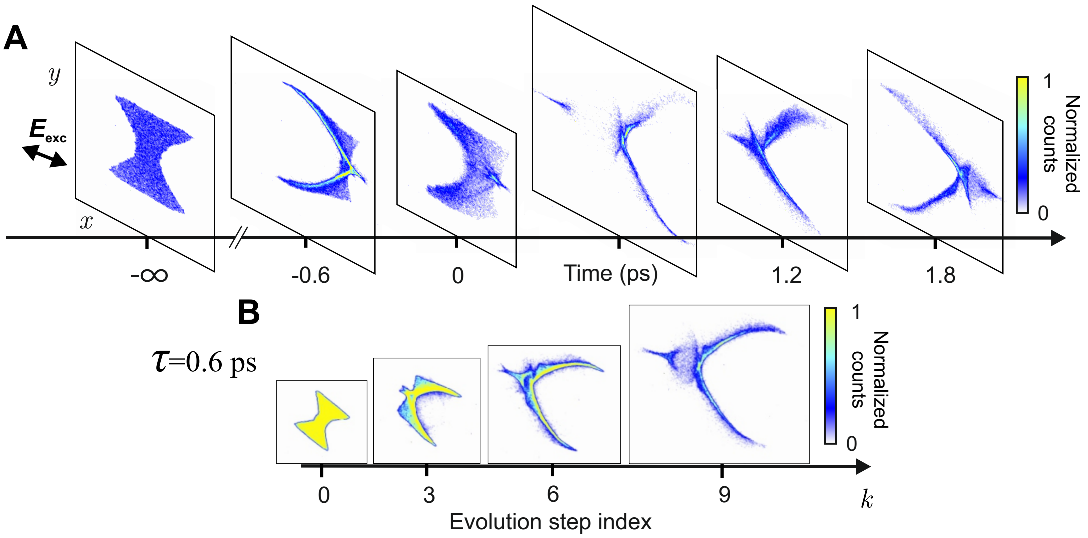

Figure 7.8: *Bowtie resonator: focus-variation approach scan.* (A) Image sequence of the raw electron density at the highest lens strength of the imaging lens (magnification 9×). (B) Discrete electron density evolution images at time delay $\tau = 0.6\,\text{ps}$ in the focus-variation approach.

Chapter 8

Discussion and outlook

As the result of this work, we have shown how to measure and reconstruct the vectorial electromagnetic dynamics in various samples with sub-cycle and sub-wavelength resolutions. There are a few advanced possibilities and further improvements that will be briefly discussed.

8.1 State-of-the-art instrumentation and plenoptic recording

A single-lens transmission electron microscope[1], as constructed and applied in this work, does not provide enough spatial and angular resolution. A real, commercial transmission electron microscope consists of at least three lenses and better apparatuses have even more, including spherical and chromatic aberration correctors. We have suggested two approaches to acquire the data necessary for waveform field reconstruction, and both can be applied to a real transmission electron microscope with their pros and cons (see Sections 6.2 and 6.3). For a double-lens or multi-lens case, theoretically, it is possible to combine the advantages of two approaches: by scanning the lenses' strengths, we can keep the magnification constant and apply a focus-variation approach (see Section 6.3) with high spatial resolution over the entire scan. Thus, nonlinear fields can be resolved without substantial resolution restrictions. By improving the fitting procedure algorithm for better computational resources, we would be able to reconstruct a sample's dynamics in space, time and vectorial direction with ultimate resolutions that are in the end only limited by the electron pulse duration and the beam emittance and aberrations.

Another prospective improvement takes its idea from light field optics [91]. Instead of recording an electron density evolution at every time delay as it is done in this work, it may be sufficient to record only one image per time delay, if a two-dimensional array of micro- or nanolenses is placed between the objective lens and the screen. This implementation,

---

[1] Here, the lens behind the sample is considered.

similar to the plenoptic camera in optics, requires not only finding a way to fabricate such lens array (or employing a sub-wavelength or metamaterial structure), but demands better quality of the electron beam. However, if all major problems are solved, the technique can become an essential built-in feature of a pulsed transmission electron microscope avoiding the need for any electron evolution scanning procedures.

8.2 B-field reconstruction

In waveform electron microscopy, the reconstructed effective field components[2] $E^{\mathrm{eff}}_{x,y} = E_{x,y} \mp v_{\mathrm{e}}\, B_{y,x}$ (see Chapter 7) incorporate magnetic fields, which might have a non-trivial response in some samples. In order to experimentally separate electric and magnetic properties of a device or metamaterial structure, we need additional data. Reconstruction of the transversal magnetic field, as already mentioned in Section 2.3, can be realized in the experiment by performing measurements at several electron acceleration voltages, i.e., electron longitudinal velocities. This is possible because the deflection by electric fields scales with v_{e}^{-2}, while the deflection by magnetic fields scales with v_{e}^{-1} (see Section 2.3).

The main challenge lies in the technical part: the electron beam should not shift at different voltages and all other conditions must remain the same in the experiment as well. A longitudinal magnetic (and electric) component can be resolved in a tomographic configuration (see Section 8.3 below) or by electron holography, which can also reveal a potential nanoscale Aharanov-Bohm effect in the sample [92].

8.3 Towards space-time tomography of electromagnetic waveforms

In Chapter 2, we had introduced some assumptions related to the electron's transition time through the sample and to the pulse duration of the single-electron pulse. Generally, the size of devices with an electromagnetic response decreases with respect to the excitation wavelength[3], thus, the transition time can approach the range of the electromagnetic oscillation period in realistic nanostructures. With pulse durations shorter than a field oscillation period, we can abandon assumption (III) in Section 2.3 and accept spatially distributed fields, meaning that equations (2.10) would contain integrals of fields over the depth in the sample. By rotating the sample and the excitation in an appropriate way, we can acquire angular dependent deflection distributions. When knowing the sample's dimensions and topography from prior calibration, we may apply tomographic reconstruction methods to obtain all six components of the electromagnetic field in space and time. The

---

[2] The components are introduced as longitudinally integrated components of the normalized Lorentz force (see Chapter 2.3).

[3] The structure size, which is resonant to the electromagnetic radiation, decreases faster than linearly with the wavelength due to the dispersion relation of the material.

problem seems to be intricate, but by implementing new ideas and methods, tomographic data acquisition and analysis can in principle be realized.

8.4 Final remarks

We have realized electron microscopy of electromagnetic waveforms and successfully revealed several sample dynamics with sub-wavelength and sub-cycle resolutions in space and time, respectively. Such exceptional temporal resolution was accomplished by compressing single-electron pulses down to 75-fs duration via an all-optical terahertz compression approach. By recording electron density evolutions in a pump-probe experiment, we reconstructed field vector dynamics through a least-square analysis of the data.

Given the advanced possibilities discussed above, this technique should be capable of a simple and straightforward integration into a commercial electron microscope, creating a powerful instrument for visualizing electrodynamics in nanoworld investigations.

Appendix A

The appendix shows math, which lies behind equations in Section 4.1.

The momentum changes $p_{x'}$ and $p_{y'}$ can be derived from the $\mathbf{E}$ and $\mathbf{B}$-field vector projections:

$$p_{x'}(\tau) = e\int_{-\infty}^{\infty} \left(E_x(t, x(t-\tau), y(t-\tau)) \cos\,\alpha_{\mathrm{e}} + E_y(t, x(t-\tau), y(t-\tau)) \sin\,\alpha_{\mathrm{e}}\right) \mathrm{d}t, \tag{1}$$

$$\begin{split} p_{y'}(\tau) = e\int_{-\infty}^{\infty} \big(E_y(t, x(t-\tau), y(t-\tau)) \cos\,\alpha_{\mathrm{e}} - E_x(t, x(t-\tau), y(t-\tau)) \sin\,\alpha_{\mathrm{e}} - \\ - v_{\mathrm{e}} B(t, x(t-\tau), y(t-\tau))\big)\, \mathrm{d}t, \end{split} \tag{2}$$

where $B = \dfrac{E_0}{c}$. The integral limits can are determined by general case and equations (4.1)-(4.3). The momentum change expressions (4.4), (4.5) can be written as sum of to integrals:

$$\begin{split} p_{x'}(\tau) = eE_0 \Bigg[\int_{-\infty}^{\tau} &(\sin(\omega t - \omega\beta\cos(\alpha-\alpha_{\mathrm{e}})(t-\tau) + \phi)\sin(\alpha_{\mathrm{e}} - \alpha) - \\ &- \sin(\omega t + \omega\beta\cos(\alpha+\alpha_{\mathrm{e}})(t-\tau) + \phi)\sin(\alpha_{\mathrm{e}} + \alpha))\mathrm{d}t + \\ \int_{\tau}^{\infty} &(\sin(\omega t - \omega\beta\cos(\alpha-\alpha_{\mathrm{e}})(t-\tau) + \phi)\sin(\alpha_{\mathrm{e}} - \alpha) - \\ &- \sin(\omega t + \omega\beta\cos(\alpha+\alpha_{\mathrm{e}})(t-\tau) + \phi)\sin(\alpha_{\mathrm{e}} + \alpha))\mathrm{d}t\Bigg], \end{split} \tag{3}$$

$$\begin{split} p_{y'}(\tau) = eE_0 \Bigg[\int_{-\infty}^{\tau} &(\sin(\omega t - \omega\beta\cos(\alpha-\alpha_{\mathrm{e}})(t-\tau) + \phi)(\cos(\alpha-\alpha_{\mathrm{e}}) - \beta) - \\ &- \sin(\omega t + \omega\beta\cos(\alpha+\alpha_{\mathrm{e}})(t-\tau) + \phi)(\cos(\alpha+\alpha_{\mathrm{e}}) + \beta))\mathrm{d}t + \\ \int_{\tau}^{\infty} &(\sin(\omega t - \omega\beta\cos(\alpha-\alpha_{\mathrm{e}})(t-\tau) + \phi)(\cos(\alpha-\alpha_{\mathrm{e}}) - \beta) - \\ &- \sin(\omega t + \omega\beta\cos(\alpha+\alpha_{\mathrm{e}})(t-\tau) + \phi)(\cos(\alpha+\alpha_{\mathrm{e}}) + \beta))\mathrm{d}t\Bigg], \end{split} \tag{4}$$

where τ is a moment, when particles enters the foil. The first term in both equations (3) and (4) are responsible for particle angles $\alpha_{\mathrm{e}} \in \left[-\dfrac{\pi}{2} + 2n\pi, \dfrac{\pi}{2} + 2n\pi\right]$, $n \in \mathbb{N}$, the second term - for $\alpha_\mathrm{e} \in \left(\frac{\pi}{2} + 2n\pi, \frac{3\pi}{2} + 2n\pi\right), n \in \mathbb{N}$. Let us work only with $\int_{-\infty}^{\tau}$ parts of equations (3) and (4):

$$\begin{aligned}
&\int_{-\infty}^{\tau} (\sin(\omega t - \omega\beta\cos(\alpha - \alpha_\mathrm{e})(t-\tau) + \phi)\sin(\alpha_\mathrm{e} - \alpha) - \\
&\qquad - \sin(\omega t + \omega\beta\cos(\alpha + \alpha_\mathrm{e})(t-\tau) + \phi)\sin(\alpha_\mathrm{e} + \alpha))\mathrm{d}t = \\
&= \frac{\sin(\alpha - \alpha_\mathrm{e})}{\omega(1 - \beta\cos(\alpha - \alpha_\mathrm{e}))}\cos(\omega t - \omega\beta\cos(\alpha - \alpha_\mathrm{e})(t-\tau) + \phi)|_{-\infty}^{\tau} + \\
&+ \frac{\sin(\alpha + \alpha_\mathrm{e})}{\omega(1 + \beta\cos(\alpha + \alpha_\mathrm{e}))}\cos(\omega t + \omega\beta\cos(\alpha + \alpha_\mathrm{e})(t-\tau) + \phi)|_{-\infty}^{\tau} = \\
&= \cos(\omega t + \phi)\left(\frac{\sin(\alpha - \alpha_\mathrm{e})}{\omega(1 - \beta\cos(\alpha - \alpha_\mathrm{e}))} + \frac{\sin(\alpha + \alpha_\mathrm{e})}{\omega(1 + \beta\cos(\alpha + \alpha_\mathrm{e}))}\right); \qquad (5)
\end{aligned}$$

$$\begin{aligned}
&\int_{-\infty}^{\tau} (\sin(\omega t - \omega\beta\cos(\alpha - \alpha_\mathrm{e})(t-\tau) + \phi)(\cos(\alpha - \alpha_\mathrm{e}) - \beta) - \\
&\qquad - \sin(\omega t + \omega\beta\cos(\alpha + \alpha_\mathrm{e})(t-\tau) + \phi)(\cos(\alpha + \alpha_\mathrm{e}) + \beta))\mathrm{d}t = \\
&= -\frac{\cos(\alpha - \alpha_\mathrm{e}) - \beta}{\omega(1 - \beta\cos(\alpha - \alpha_\mathrm{e}))}\cos(\omega t - \omega\beta\cos(\alpha - \alpha_\mathrm{e})(t-\tau) + \phi)|_{-\infty}^{\tau} + \\
&+ \frac{\cos(\alpha + \alpha_\mathrm{e}) + \beta}{\omega(1 + \beta\cos(\alpha + \alpha_\mathrm{e}))}\cos(\omega t + \omega\beta\cos(\alpha + \alpha_\mathrm{e})(t-\tau) + \phi)|_{-\infty}^{\tau} = \\
&= \cos(\omega t + \phi)\left(\frac{\cos(\alpha + \alpha_\mathrm{e}) + \beta}{\omega(1 + \beta\cos(\alpha + \alpha_\mathrm{e}))} - \frac{\cos(\alpha - \alpha_\mathrm{e}) - \beta}{\omega(1 - \beta\cos(\alpha - \alpha_\mathrm{e}))}\right). \qquad (6)
\end{aligned}$$

Here we used an approximation that at the infinity there is no interaction (plane wave envelope with close to infinite duration). For $\int_{\tau}^{\infty}$, expressions (5) and (6) hold the same absolute value but the overall sign is changed. See equation (4.6) and (4.7) for final expressions.

The zero-condition for deflection can be found from equation (4.7) by equating expression in brackets to zero:

$$\begin{aligned}
&(\cos(\alpha + \alpha_\mathrm{e}) + \beta)(1 - \beta\cos(\alpha - \alpha_\mathrm{e})) - (\cos(\alpha - \alpha_\mathrm{e}) - \beta)(1 + \beta\cos(\alpha + \alpha_\mathrm{e})) = \\
&= \left|\begin{matrix}\cos(+) = \cos(\alpha + \alpha_\mathrm{e}) \\ \cos(-) = \cos(\alpha - \alpha_\mathrm{e})\end{matrix}\right| = (1 + \beta^2)(\cos(+) - \cos(-)) - 2\beta(\cos(+)\cos(-) - 1) = \\
&= -2(1 + \beta^2)\sin\alpha\sin\alpha_\mathrm{e} - 2\beta(\cos^2\alpha\cos^2\alpha_\mathrm{e} - \sin^2\alpha\sin^2\alpha_\mathrm{e} - 1) = \\
&= -2(1 + \beta^2)\sin\alpha\sin\alpha_\mathrm{e} - 2\beta(-\sin^2\alpha - \sin^2\alpha_\mathrm{e}) = \\
&= 2\beta\sin^2\alpha_\mathrm{e} - 2(1 + \beta^2)\sin\alpha\sin\alpha_\mathrm{e} + 2\beta\sin^2\alpha = 0; \qquad (7)
\end{aligned}$$

The solution of this quadratic equation is:

$$\sin\,\alpha_{\mathrm{e}} = \begin{cases} \beta \sin\,\alpha, \\ \dfrac{\sin\,\alpha}{\beta}. \end{cases} \tag{8}$$

It's important to admit that the first solution in equation (8) is a velocity-matching condition (see equation (4.8)), the second solution in equation (8) is held for superluminal particles.

Appendix B

In the appendix, we estimate some quantities, e.g., ω_0, coordinate shift and drift in a sample x, introduced in Section 2.3. There, we had applied certain approximations and derived equations relating to the measured deflections of the effective field components. We assumed $\omega t_0 < 1$, now we estimate the limit of B_z for our particular setup. The electron-field interaction ends at $t = \tau_{\mathrm{transition}} = l_{\mathrm{sample}}\, v_{\mathrm{e}}^{-1}$, hence, $(e\, B_z\, l_{\mathrm{sample}}\, m_{\mathrm{e}}^{-1}\, v_{\mathrm{e}}^{-1}) < 1$. At given $l_{\mathrm{sample}} = 30\,\mu\mathrm{m}$, the typical dimensions of sample under the investigation in this work, and $v_{\mathrm{e}} = 0.48c$, we estimate $B_z < 27.3\,\mathrm{T}$, which corresponds to electric field of $E \approx 8.2 \times 10^9 \frac{\mathrm{V}}{\mathrm{m}}$ in rough estimation. It means that approximation $\omega_0 t < 1$ is totally valid for the field amplitudes used in our experiments and can be applied for higher field amplitudes with respective values of l_{sample} and v_{e}.

In this work, the peak electrical field inside the sample is $E^* \approx 10^7 \frac{\mathrm{V}}{\mathrm{m}}$ and $f^0_{x,y} \approx \frac{e\,E^*}{m_{\mathrm{e}}}$, thus we can assume upper limit for $B_z^* = \frac{E^*}{c} \approx 33\,\mathrm{mT}$[4]. The estimation of upper limit for the electron drift and velocity at $t = \tau_{\mathrm{transition}}$ from the expressions (2.14) and (2.15) for particular values given above, which are characteristic for the current work:

$$x(t_{\mathrm{sample}}) \approx \frac{v_x^0}{c} 62.5\mu\mathrm{m} + 38\mathrm{nm} + \frac{v_y^0}{c} 38\mathrm{nm}; \tag{9}$$

$$\dot{x}(t_{\mathrm{sample}}) = v_x \approx v_x^0 + 1.2\times 10^{-3}\, c + 1.2\times 10^{-3}\, v_y^0. \tag{10}$$

From equations (9) and (10), it is obvious that we should align the sample, the electron beam and the detector in a way to exclude v_x^0 and v_y^0. If we do so, then the deflection inside the sample is $\sim$40 nm, which is negligible. In Section 6.2 (equation (6.12)), we estimate the minimal angular resolution as $\alpha_{div} \approx 60$ µrad, which corresponds to $v_{\mathrm{min}} = v^0_{x,y} \approx 2.9\times 10^{-5}$c or $E^{\mathrm{eff}}_{\mathrm{min}} \approx 2.4\times 10^5$ V/m, meaning that the gained transversal velocity by the E^* is $1.2\times 10^{-3}\, c$, which 2 orders above the resolution limit. If the sample and the electron beam are aligned in such a way, that there exists a small tilt angle θ and $v^0_{x,y} = \theta_{x,y}\, v_{\mathrm{e}}$, then

---

[4] For the plane wave with $\mathbf{E} = \{0, E_0, 0\}$ $B_z = 0$ but near the structure (or within it) B_z-component exists because of the material bounds. If enhancement of the electric field occurs, it also occurs in B_z-component due to $\frac{\partial B}{\partial t} \propto \left(\frac{\partial E_y}{\partial x} - \frac{\partial E_x}{\partial y}\right)$.

the correction can be in a detectable regime: for $\theta = 7°$ the x-shift in the sample is $\sim 1.2\,\mu\mathrm{m}$ and the velocity correction caused by B_z-component is $\left(\frac{v_y^0}{c}\,1.2 \times 10^{-3}\,c\right) \approx 2.2 \times 10^{-5}\,c$.

We consider that the initial velocity components $v_{x,y}^0$ were diminished to values $\alpha_{\mathrm{div}} v_{\mathrm{e}}$ in the experiment, thus, the impact of the B_z-component is insignificant and we resolve an effective fields $E_{x,y}^{\mathrm{eff}} = E_{x,y} \mp v_{\mathrm{e}}\, B_{y,x}$, introduced in (2.11) with amplitudes higher than $E_{\mathrm{min}}^{\mathrm{eff}} \approx 2.4 \times 10^5 \mathrm{V/m}$.

Data Archiving

The experimental raw data, evaluation files, and original figures can be found on the Data Archive Server of the Laboratory for Attosecond Physics at the Max Planck Institute of Quantum Optics: `/afs/rzg/mpq/lap/publication_archive`

The source data of all figures is organized relative to the root folder of the data archive for the thesis within subfolders inside the `/figures` directory, using the same figure numbers as in the thesis. A text file within each figure's folder named `fig X.X.txt` (`X.X` being the figure's number) gives detailed information about the organization and format of the raw data, as well as the processing performed in order to obtain the final figure. Further experimental and simulation details are given where applicable, in addition to the main text.

Bibliography

[1] R. Erni, M. D. Rossell, C. Kisielowski, and U. Dahmen, "Atomic-resolution imaging with a sub-50-pm electron probe," *Phys. Rev. Lett.*, vol. 102, p. 096101, Mar. 2009.

[2] P. E. Batson, N. Dellby, and O. L. Krivanek, "Sub-angstrom resolution using aberration corrected electron optics," *Nature*, vol. 418, pp. 617–620, Aug. 2002.

[3] K. Mueller, F. F. Krause, A. Beche, M. Schowalter, V. Galioit, S. Loeffler, J. Verbeeck, J. Zweck, P. Schattschneider, and A. Rosenauer, "Atomic electric fields revealed by a quantum mechanical approach to electron picodiffraction," *Nature Communications*, vol. 5, p. 5653, Dec. 2014.

[4] S. Neppl, R. Ernstorfer, E. M. Bothschafter, A. L. Cavalieri, D. Menzel, J. V. Barth, F. Krausz, R. Kienberger, and P. Feulner, "Attosecond time-resolved photoemission from core and valence states of magnesium," *Physical Review Letters*, vol. 109, p. 087401, Aug. 2012.

[5] K. C. Prince, E. Allaria, C. Callegari, R. Cucini, G. D. Ninno, S. D. Mitri, B. Diviacco, E. Ferrari, P. Finetti, D. Gauthier, L. Giannessi, N. Mahne, G. Penco, O. Plekan, L. Raimondi, P. Rebernik, E. Roussel, C. Svetina, M. Trovó, M. Zangrando, M. Negro, P. Carpeggiani, M. Reduzzi, G. Sansone, A. N. Grum-Grzhimailo, E. V. Gryzlova, S. I. Strakhova, K. Bartschat, N. Douguet, J. Venzke, D. Iablonskyi, Y. Kumagai, T. Takanashi, K. Ueda, A. Fischer, M. Coreno, F. Stienkemeier, Y. Ovcharenko, T. Mazza, and M. Meyer, "Coherent control with a short-wavelength free-electron laser," *Nat Photon*, vol. 10, pp. 176–179, Mar. 2016.

[6] M. Huppert, I. Jordan, D. Baykusheva, A. von Conta, and H. J. Wörner, "Attosecond delays in molecular photoionization," *Phys. Rev. Lett.*, vol. 117, p. 093001, Aug. 2016.

[7] M. A. Seo, A. J. L. Adam, J. H. Kang, J. W. Lee, S. C. Jeoung, Q. H. Park, P. C. M. Planken, and D. S. Kim, "Fourier-transform terahertz near-field imaging of one-dimensional slit arrays: mapping of electric-field-, magnetic-field-, and poynting vectors," *Opt. Express*, vol. 15, pp. 11781–11789, Sept. 2007.

[8] A. Bitzer, H. Merbold, A. Thoman, T. Feurer, H. Helm, and M. Walther, "Terahertz near-field imaging of electric and magnetic resonances of a planar metamaterial," *Opt. Express*, vol. 17, pp. 3826–3834, Mar. 2009.

[9] H. Murakami, K. Serita, Y. Maekawa, S. Fujiwara, E. Matsuda, S. Kim, I. Kawayama, and M. Tonouchi, "Scanning laser terahertz imaging system," *Journal of Physics D: Applied Physics*, vol. 47, p. 374007, Aug. 2014.

[10] F. Blanchard, A. Doi, T. Tanaka, and K. Tanaka, "Real-time, subwavelength terahertz imaging," *Annual Review of Materials Research*, vol. 43, pp. 237–259, July 2013.

[11] M. Eisele, T. L. Cocker, M. A. Huber, M. Plankl, L. Viti, D. Ercolani, L. Sorba, M. S. Vitiello, and R. Huber, "Ultrafast multi-terahertz nano-spectroscopy with sub-cycle temporal resolution," *Nature Photonics*, vol. 8, p. 841845, Oct. 2014.

[12] K. Lee, H. Kih, J. Kihm, W. Choi, H. Kim, C. Ropers, D. Park, Y. Yoon, S. Choi, D. Woo, K. J., B. Lee, Q. Park, C. Lienau, and D. Kim, "Vector field microscopic imaging of light," *Nature Photon*, vol. 1, pp. 53–56, Jan. 2007.

[13] M. Namboodiri, T. Khan, K. Karki, M. Kazemi, S. Bom, G. Flachenecker, V. Namboodiri, and A. Materny, "Nonlinear spectroscopy in the near-field: time resolved spectroscopy and subwavelength resolution non-invasive imaging," *Nanophotonics*, vol. 3, p. 6173, Mar. 2014.

[14] S. Viarbitskaya, A. Teulle, R. Marty, J. Sharma, C. Girard, A. Arbouet, and E. Dujardin, "Tailoring and imaging the plasmonic local density of states in crystalline nanoprisms," *Nature Materials*, vol. 12, pp. 426–432, May 2013.

[15] T. L. Cocker, V. Jelic, M. Gupta, S. J. Molesky, J. BurgessJacob A., G. D. L. Reyes, L. V. Titova, Y. Y. Tsui, M. R. Freeman, and F. A. Hegmann, "An ultrafast terahertz scanning tunnelling microscope," *Nat Photon*, vol. 7, pp. 620–625, Aug. 2013.

[16] G. C. Cho, H.-T. Chen, S. Kraatz, N. Karpowicz, and R. Kersting, "Apertureless terahertz near-field microscopy," *Semiconductor Science and Technology*, vol. 20, p. S286, June 2005.

[17] A. Lubk and J. Zweck, "Differential phase contrast: An integral perspective," *Physical Review A*, vol. 91, p. 023805, Feb. 2015.

[18] J. Itatani, J. Levesque, D. Zeidler, H. Niikura, H. Pepin, J. C. Kieffer, P. B. Corkum, and D. M. Villeneuve, "Tomographic imaging of molecular orbitals," *Nature*, vol. 432, pp. 867–871, Dec. 2004.

[19] M. J. J. Vrakking, "Attosecond imaging," *Phys. Chem. Chem. Phys.*, vol. 16, pp. 2775–2789, Nov. 2014.

[20] P. B. Corkum and F. Krausz, “Attosecond science,” *Nature Physics*, vol. 3, pp. 381–387, June 2007.

[21] T. Suzuki, “Femtosecond time-resolved photoelectron imaging,” *Annual Review of Physical Chemistry*, vol. 57, pp. 555–592, May 2006.

[22] L. Chen, R. Li, J. Chen, P. Zhu, F. Liu, J. Cao, Z. Sheng, and J. Zhang, “Mapping transient electric fields with picosecond electron bunches,” *PNAS*, vol. 112, pp. 14479–14483, Nov. 2015.

[23] A. R. Bainbridge, C. W. Barlow Myers, and W. A. Bryan, “Femtosecond few- to single-electron point-projection microscopy for nanoscale dynamic imaging,” *Structural Dynamics*, vol. 3, Mar. 2016.

[24] M. Müller, A. Paarmann, and R. Ernstorfer, “Femtosecond electrons probing currents and atomic structure in nanomaterials,” *Nature Communications*, vol. 5, p. 5292, Oct. 2014.

[25] J. Yang, J. Beck, C. J. Uiterwaal, and M. Centurion, “Imaging of alignment and structural changes of carbon disulfide molecules using ultrafast electron diffraction,” *Nature Communications*, vol. 6, p. 8172, Sept. 2015.

[26] A. Yurtsever, R. M. van der Veen, and A. H. Zewail, “Subparticle ultrafast spectrum imaging in 4D electron microscopy,” *Science*, vol. 335, pp. 59–64, Jan. 2012.

[27] A. Yurtsever and A. H. Zewail, “Direct visualization of near-fields in nanoplasmonics and nanophotonics,” *Nano Letters*, vol. 12, pp. 3334–3338, May 2012.

[28] S. T. Park, M. M. Lin, and A. H. Zewail, “Photon-induced near-field electron microscopy (PINEM): theoretical and experimental,” *New Journal of Physics*, vol. 12, p. 123028, Dec. 2010.

[29] B. Schaffer, K. Riegler, G. Kothleitner, W. Grogger, and F. Hofer, “Monochromated, spatially resolved electron energy-loss spectroscopic measurements of gold nanoparticles in the plasmon range,” *Micron*, vol. 40, pp. 269 – 273, Feb. 2009.

[30] O. Nicoletti, F. de la Pena, R. K. Leary, D. J. Holland, C. Ducati, and P. A. Midgley, “Three-dimensional imaging of localized surface plasmon resonances of metal nanoparticles,” *Nature*, vol. 502, pp. 80–84, Oct. 2013.

[31] A. Ryabov and P. Baum, “Electron microscopy of electromagnetic waveforms,” *Science*, vol. 353, pp. 374–377, July 2016.

[32] M. Aidelsburger, F. O. Kirchner, F. Krausz, and P. Baum, “Single-electron pulses for ultrafast diffraction,” *Proceedings of the National Academy of Sciences of the United States of America*, vol. 107, pp. 19714–19719, Nov. 2010.

[33] C. Carter and D. Williams, *Transmission Electron Microscopy: Diffraction, Imaging, and Spectrometry.* Springer International Publishing, 2016.

[34] L. Landau and E. Lifshitz, *Quantum Mechanics. Course of Theoretical Physics*, vol. Volume 3. Pergamon Press, 1965.

[35] P. Baum, "Towards ultimate temporal and spatial resolutions with ultrafast single-electron diffraction," *Journal of Physics B-atomic Molecular and Optical Physics*, vol. 47, p. 124005, June 2014.

[36] C. Kealhofer, W. Schneider, D. Ehberger, A. Ryabov, F. Krausz, and P. Baum, "All-optical control and metrology of electron pulses," *Science*, vol. 352, pp. 429–433, Apr. 2016.

[37] L. Kasmi, D. Kreier, M. Bradler, E. Riedle, and P. Baum, "Femtosecond single-electron pulses generated by two-photon photoemission close to the work function," *New Journal of Physics*, vol. 17, p. 033008, May 2015.

[38] A. Gliserin, A. Apolonski, F. Krausz, and P. Baum, "Compression of single-electron pulses with a microwave cavity," *New Journal of Physics*, vol. 14, p. 073055, July 2012.

[39] P. Baum, "On the physics of ultrashort single-electron pulses for time-resolved microscopy and diffraction," *Chemical Physics*, vol. 423, pp. 55–61, Sept. 2013.

[40] A. Gliserin, M. Walbran, F. Krausz, and P. Baum, "Sub-phonon-period compression of electron pulses for atomic diffraction," *Nature Communications*, vol. 6, p. 8723, Oct. 2015.

[41] C. Weninger and P. Baum, "Temporal distortions in magnetic lenses," *Ultramicroscopy*, vol. 113, pp. 145–151, Feb. 2012.

[42] W. Schneider, "Deflection of electron pulses by thz fields," *PhD thesis, Ludwig-Maximilians Universitt Mnchen,*, June 2015.

[43] W. Schneider, A. Ryabov, C. Lombosi, T. Metzger, Z. Major, J. A. Fülöp, and P. Baum, "800-fs, 330-J pulses from a 100-W regenerative Yb:YAG thin-disk amplifier at 300 kHz and THz generation in LiNbO3," *Optics Letters*, vol. 39, pp. 6604–6607, Dec. 2014.

[44] J. A. Fülöp, Z. Ollmann, C. Lombosi, C. Skrobol, S. Klingebiel, L. Pálfalvi, F. Krausz, S. Karsch, and J. Hebling, "Efficient generation of thz pulses with 0.4 mj energy," *Opt. Express*, vol. 22, pp. 20155–20163, Aug 2014.

[45] M. V. Tsarev, D. Ehberger, and P. Baum, "High-average-power, intense THz pulses from a LiNbO3 slab with silicon output coupler," *Applied Physics B*, vol. 122, p. 30, Jan. 2016.

[46] D. Kreier, “Ultrafast single-electron diffraction at 100 kev and investigation of carbon-nanotube dynamics,” *PhD thesis, Ludwig-Maximilians Universitt Mnchen*, Jan. 2015.

[47] F. A. Siegrist, “Messung der emittanz einer femtosekunden-elektronenquelle,” *Bachelorarbeit, Ludwig-Maximilians-Universität München*, July 2013.

[48] A. Klug, “Image analysis and reconstruction in the electron microscopy of biological macromolecules,” *Chemica Scripta*, vol. 14, pp. 245–256, 1979.

[49] D. Shi, B. L. Nannenga, M. G. Iadanza, and T. Gonen, “Three-dimensional electron crystallography of protein microcrystals,” *eLife*, vol. 2, p. e01345, Oct. 2013.

[50] P. Baum and A. H. Zewail, “Breaking resolution limits in ultrafast electron diffraction and microscopy,” *Proceedings of the National Academy of Sciences of the United States of America*, vol. 103, pp. 16105–16110, Oct. 2006.

[51] D. J. Flannigan and A. H. Zewail, “4D electron microscopy: Principles and applications,” *Accounts of Chemical Research*, vol. 45, pp. 1828–1839, Nov. 2012.

[52] S. Lahme, C. Kealhofer, F. Krausz, and P. Baum, “Femtosecond single-electron diffraction,” *Structural Dynamics*, vol. 1, p. 034303, June 2014.

[53] M. Eichberger, N. Erasmus, K. Haupt, G. Kassier, A. von Flotow, J. Demsar, and H. Schwoerer, “Femtosecond streaking of electron diffraction patterns to study structural dynamics in crystalline matter,” *Applied Physics Letters*, vol. 102, p. 121106, Mar. 2013.

[54] M. Gao, Y. Jiang, G. H. Kassier, and R. J. D. Miller, “Single shot time stamping of ultrabright radio frequency compressed electron pulses,” *Applied Physics Letters*, vol. 103, p. 033503, July 2013.

[55] P. Baum and A. Zewail, “Femtosecond diffraction with chirped electron pulses,” *Chemical Physics Letters*, vol. 462, pp. 14–17, Sept. 2008.

[56] M. T. Hassan, H. Liu, J. S. Baskin, and A. H. Zewail, “Photon gating in four-dimensional ultrafast electron microscopy,” *Proceedings of the National Academy of Sciences of the United States of America*, vol. 112, pp. 12944–12949, Oct. 2015.

[57] M. Kozak, J. McNeur, K. J. Leedle, N. Schoenenberger, A. Ruehl, I. Hartl, J. S. Harris, R. L. Byer, and P. Hommelhoff, “Optical gating and streaking of free-electrons with attosecond precision,” *arXiv:1512.04394*, Dec. 2015.

[58] T. van Oudheusden, P. L. E. M. Pasmans, S. B. van der Geer, M. J. de Loos, M. J. van der Wiel, and O. J. Luiten, “Compression of subrelativistic space-charge-dominated electron bunches for single-shot femtosecond electron diffraction,” *Physical Review Letters*, vol. 105, p. 264801, Dec. 2010.

[59] M. Walbran, A. Gliserin, K. Jung, J. Kim, and P. Baum, "5-femtosecond laser-electron synchronization for pump-probe crystallography and diffraction," *Phys. Rev. Applied*, vol. 4, p. 044013, Oct 2015.

[60] N. Laman and D. Grischkowsky, "Terahertz conductivity of thin metal films," *Applied Physics Letters*, vol. 93, Aug. 2008.

[61] F. O. Kirchner, A. Gliserin, F. Krausz, and P. Baum, "Laser streaking of free electrons at 25 keV," *Nature Photonics*, vol. 8, pp. 52–57, Jan. 2014.

[62] A. Feist, K. E. Echternkamp, J. Schauss, S. V. Yalunin, S. Schaefer, and C. Ropers, "Quantum coherent optical phase modulation in an ultrafast transmission electron microscope," *Nature*, vol. 521, p. 200, May 2015.

[63] A. Gliserin, M. Walbran, and P. Baum, "Passive optical enhancement of laser-microwave synchronization," *Applied Physics Letters*, vol. 103, p. 031113, July 2013.

[64] T. W. Ebbesen, H. J. Lezec, H. F. Ghaemi, T. Thio, and P. A. Wolff, "Extraordinary optical transmission through sub-wavelength hole arrays," *Nature*, vol. 391, pp. 667–669, Feb. 1998.

[65] E.-S. Kwak, J. Henzie, S.-H. Chang, S. K. Gray, G. C. Schatz, , and T. W. Odom, "Surface plasmon standing waves in large-area subwavelength hole arrays," *Nano Letters*, vol. 5, pp. 1963–1967, Oct. 2005.

[66] X. Lu and W. Zhang, "Terahertz localized plasmonic properties of subwavelength ring and coaxial geometries," *Applied Physics Letters*, vol. 94, May 2009.

[67] S. Yin, X. Lu, N. Xu, S. Wang, E. Yiwen, X. Pan, X. Xu, H. Liu, L. Chen, W. Zhang, and L. Wang, "Spoof surface plasmon polaritons in terahertz transmission through subwavelength hole arrays analyzed by coupled oscillator model," *Scientific Reports*, vol. 5, p. 16440, Nov. 2015.

[68] N. I. Zheludev, "The road ahead for metamaterials," *Science*, vol. 328, pp. 582–583, Apr. 2010.

[69] N. I. Zheludev and Y. S. Kivshar, "From metamaterials to metadevices," *Nature Materials*, vol. 11, pp. 917–924, Nov. 2012.

[70] K. Yao and Y. Liu, "Plasmonic metamaterials," *arXiv:1312.4614*, Dec. 2013.

[71] J. Fabianska, G. Kassier, and T. Feurer, "Split ring resonator based thz-driven electron streak camera featuring femtosecond resolution.," *Scientific reports*, vol. 4, pp. 5645–5645, July 2014.

[72] S. Shapiro, "Ultrashort light pulses," *Springer-Verlag Berlin Heidelberg*, 1984.

[73] A. Berrier, P. Albella, M. A. Poyli, R. Ulbricht, M. Bonn, J. Aizpurua, and J. G. Rivas, “Detection of deep-subwavelength dielectric layers at terahertz frequencies using semiconductor plasmonic resonators,” *Opt. Express*, vol. 20, pp. 5052–5060, Feb 2012.

[74] M. I. Stockman, M. F. Kling, U. Kleineberg, and F. Krausz, “Attosecond nanoplasmonic-field microscope,” *Nat Photon*, vol. 1, pp. 539–544, Sept. 2007.

[75] R. Kienberger, E. Goulielmakis, M. Uiberacker, A. Baltuska, V. Yakovlev, F. Bammer, A. Scrinzi, T. Westerwalbesloh, U. Kleineberg, U. Heinzmann, M. Drescher, and F. Krausz, “Atomic transient recorder,” *Nature*, vol. 427, pp. 817–821, Feb. 2004.

[76] M. M. Shakya and Z. H. Chang, “Achieving 280 fs resolution with a streak camera by reducing the deflection dispersion,” *Applied Physics Letters*, vol. 87, p. 041103, July 2005.

[77] C. E. Willert and M. Gharib, “Digital particle image velocimetry,” *Experiments in Fluids*, vol. 10, pp. 181–193, Jan. 1991.

[78] Y. Zeldovich and A. Mishkis, “Elements of mathematical physics,” *Nauka*, 1973.

[79] V. Kumar, “Understanding the focusing of charged particle beams in a solenoid magnetic field,” *American Journal of Physics*, vol. 77, pp. 737–741, July 2009.

[80] M. J. Pritchard, “Manipulation of ultracold atoms using magnetic and optical fields,” *PhD thesis, University of Durham*, Sept. 2006.

[81] R. Erni, “Aberration-corrected imaging in transmission electron microscopy. an introduction,” *Imperial College Press*, 2010.

[82] T. Urban, “Charakterisierung und optimierung der detektion von einzelelektronen für die ultraschnelle elektronenbeugung,” *Bachelorarbeit am Physik-Department der Technischen Universität München*, Aug. 2014.

[83] J. Nocedal and S. Wright, *Numerical Optimization.* Springer Series in Operations Research and Financial Engineering, Springer New York, 2006.

[84] G. Strang, *Linear Algebra and Its Applications.* Thomson, Brooks/Cole, 2006.

[85] A. Chatterjee, “An introduction to the proper orthogonal decomposition,” *Current Science*, vol. 78, pp. 763–927, Apr. 2000.

[86] B. Feeny, “A complex orthogonal decomposition for wave motion analysis,” *Journal of Sound and Vibration*, vol. 310, pp. 77 – 90, Apr. 2008.

[87] Q. Zhang, Y. Liu, and S. Wang, “The identification of coherent structures using proper orthogonal decomposition and dynamic mode decomposition,” *Journal of Fluids and Structures*, vol. 49, pp. 53 – 72, Aug. 2014.

[88] F. Guéniat, L. Pastur, and F. Lusseyran, “Investigating mode competition and three-dimensional features from two-dimensional velocity fields in an open cavity flow by modal decompositions,” *Physics of Fluids*, vol. 26, Aug. 2014.

[89] G. Golub and C. Van Loan, *Matrix Computations*. Johns Hopkins Studies in the Mathematical Sciences, Johns Hopkins University Press, 1996.

[90] J. B. Masson and G. Gallot, “Terahertz achromatic quarter-wave plate,” *Optics Letters*, vol. 31, pp. 265–267, Jan. 2006.

[91] R. Ng, M. Levoy, M. Brdif, G. Duval, M. Horowitz, and P. Hanrahan, “Light field photography with a hand-held plenoptic camera,” *Stanford University Computer Science Tech Report*, Apr. 2005.

[92] A. Tonomura, T. Matsuda, R. Suzuki, A. Fukuhara, N. Osakabe, H. Umezaki, J. Endo, K. Shinagawa, Y. Sugita, and H. Fujiwara, “Observation of aharonov-bohm effect by electron holography,” *Phys. Rev. Lett.*, vol. 48, pp. 1443–1446, May 1982.

List of publications

[1] **A. Ryabov** and P. Baum, "Electron microscopy of electromagnetic waveforms," *Science*, vol. 353, no. 6297, pp. 374-377 (2016)

[2] C. Kealhofer, W. Schneider, D. Ehberger, **A. Ryabov**, F. Krausz, and P. Baum, "All-optical control and metrology of electron pulses," *Science*, vol. 352, no. 6284, pp. 429-433 (2016)

[3] W. Schneider, **A. Ryabov**, C. Lombosi, T. Metzger, Z. Major, J. A. Fülöp, and P. Baum, "800-fs, 330-J pulses from a 100-W regenerative Yb:YAG thin-disk amplifier at 300 kHz and THz generation in LiNbO3," Optics Letters, vol. 39, pp. 6604-6607 (2014)

[4] M. M. Nazarov, V. K. Balya, I. Yu. Denisyuk, **A. Yu. Ryabov**, and A. P. Shkurinov, "Obtaining terahertz-range metamaterials by laser engraving," *J. Opt. Technol.* 79, 251-256 (2012)

Acknowledgements

As the last memo of the work, I would like to thank numerous people who influenced on and contributed to this work. First of all, I want to thank Professor Ferenc Krausz for giving me a great opportunity to join the group of such outstanding scientists and to have a glance into the attoworld. Experience I have gained over past 4.5 years is a big treasure I own now. I would like also to thank Professor Roland Kersting for agreeing to review my thesis Professor Eberhard Riedle and Professor Armin Scrinzi for taking part in my PhD defense committee.

I have to admit that I had great luck to be a member of Peter Baum's group. His support, guidance and exceptional way of thinking made my PhD time indeed full of enthusiasm, his ideas truly could excite and motivate for new findings. The amount of his patience can hardly be overestimated, especially, during his help with paper and thesis writing. I started the lab work in the group under guidance of Waldemar Schneider, whom I want to thank for knowledge and experience he shared with me. I am grateful to Alexander Gliserin, our LabVIEW guru, for sharing his knowledge about hardware, software and, in general, "scienceware". Many thanks to Matthew Walbran, my NZ friend, for his limitless responsiveness and for the great time spent inside and outside our office. Alex and Matt should definitely be honored as persons, who could proofread in extreme rush: you, guys, contributed a lot to make my thesis readable. Also, I own a big "Danke" to Alex for abstract translation. Many thanks to Dominik Ehberger and Catherine Kealhofer for the great collaboration and results, which really made my experiment to be performed smoothly. I thank all group alumni with whom I had a chance to work. The amount of knowledge I got in the group during PhD time is really huge.

I am very thankful to my family for support and love: my mom Svetlana and dad Yuriy, my brother Alexey and my sister-in-law Mariya, my beloved nieces, Alexandra and Kseniya. The thought that I am always welcome gave me a nice advantage while living abroad.

I want to thank Elena Fedulova for her help in my initial German life and with my PhD defense planning. No one can say if I could ever reach my current status of "PhD-student-who-wrote-the-thesis" without the support of my Munich friends, but I would say "no, I could not". Olga Vasilyeva, Alexander Peregudov, Tatjana Keller and Lilja Root – you all gave me the feeling that I am at home. I have to thank Alexandra Verezemskaya, who inspired me to search a PhD position abroad and gave me a nice survival lesson. I am very thankful to Anastasiya Naumets, who was cheering me up and motivating during almost

two last years. I can not forget my “Siegen” friends, Evgeniy Tikhomirov and Anastasiya Lunegova, who also gave me support and motivation (however, maybe they do not realize that). I am grateful to Igor Obraztsov for a friendly-scientific help and support with my talk. Now, I do hope that more interesting things are waiting for me in this life!